Conference Proceedings of the Society for Experimental Mechanics Series

Christopher Niezrecki *Editor*

Structural Health Monitoring & Damage Detection, Volume 7

Proceedings of the 35th IMAC, A Conference and Exposition on Structural Dynamics 2017

Springer

Conference Proceedings of the Society for Experimental Mechanics Series

Series Editor

Kristin B. Zimmerman, Ph.D.
Society for Experimental Mechanics, Inc.,
Bethel, CT, USA

More information about this series at http://www.springer.com/series/8922

Christopher Niezrecki
Editor

Structural Health Monitoring & Damage Detection, Volume 7

Proceedings of the 35th IMAC, A Conference and Exposition on Structural Dynamics 2017

Springer

Editor
Christopher Niezrecki
Department of Mechanical Engineering
University of Massachusetts
Lowell, MA, USA

ISSN 2191-5644 ISSN 2191-5652 (electronic)
Conference Proceedings of the Society for Experimental Mechanics Series
ISBN 978-3-319-54108-2 ISBN 978-3-319-54109-9 (eBook)
DOI 10.1007/978-3-319-54109-9

Library of Congress Control Number: 2017934884

Printed on acid-free paper

This Springer imprint is published by Springer Nature
The registered company is Springer International Publishing AG
The registered company address is: Gewerbestrasse 11, 6330 Cham, Switzerland

Preface

Structural Health Monitoring & Damage Detection represents one of ten volumes of technical papers presented at the 35th IMAC, A Conference and Exposition on Structural Dynamics, organized by the Society for Experimental Mechanics, and held in Garden Grove, California, January 30 to February 2, 2017. The full proceedings also include volumes on *Nonlinear Dynamics*, *Dynamics of Civil Structures*, *Model Validation and Uncertainty Quantification*, *Dynamics of Coupled Structures*, *Sensors and Instrumentation*, *Special Topics in Structural Dynamics*, *Rotating Machinery*, *Hybrid Test Methods*, *Vibro-Acoustics and Laser Vibrometry*, *Shock & Vibration*, *Aircraft/Aerospace and Energy Harvesting*, and *Topics in Modal Analysis & Testing*.

Each collection presents early findings from experimental and computational investigations on an important area within structural dynamics. Structural health monitoring and damage are a couple of these areas.

The organizers would like to thank the authors, presenters, session organizers, and session chairs for their participation in this track.

Lowell, MA, USA — Christopher Niezrecki

Contents

Chapter 1
Exploiting Spatial Sparsity in Vibration-Based Damage Detection

Chandler Smith and Eric M. Hernandez

Abstract One of the main limitations traditionally encountered in vibration-based structural health monitoring (SHM) is detecting, localizing and quantifying localized damage using global response measurements. This paper presents an impulse response sensitivity approach enhanced with a LASSO regularization in order to detect spatially sparse (localized) damage. The analytical expression for impulse response sensitivity was derived using Vetter calculus. The proposed algorithm exploits the fact that when damage is sparse, an l_1-norm regularization is more suitable than the more common least squares (l_2-norm) minimization. The proposed methodology is successfully applied in the context of a simulated non-uniform shear cantilever beam with noise-contaminated input–output measurements.

Keywords Sparsity • Impulse response • Lasso • Damage • Sensitivity

1.1 Introduction

Detecting damage in the form of stiffness reduction is an important problem in structural health monitoring (SHM). A variety of methods have been proposed in the last three decades [1, 2]. The concept of spatial sparsity and how to best exploit in the context of vibration-based damage detection has been recently proposed. Kaouk and Zimmerman [3] derived algorithms to detect damage using a minimum rank perturbation criteria. Although low rank perturbation of the stiffness matrix does not necessarily imply spatial sparsity, their work represents one of the first contributions in the use sparsity as a constraint.

More recently, Link and Zimmerman [4] used greedy pursuit methods to detect spatially sparse damage using frequency response functions. However, more effective and efficient sparse recovery algorithms such as the Basis Pursuit are more commonly used. One example of exploiting spatial sparsity in SHM with basis pursuit algorithms can be found in work by Hernandez [5, 6] which utilizes eigenvalue sensitivity and l_1 minimization to locate sparse damages. The algorithm has been validated experimentally.

This paper extends the idea presented in [5, 6] into the time domain and uses impulse response sensitivity to locate and quantify spatially sparse damage. The main hypothesis is that by using impulse response sensitivity we can effectively and compactly combine the effect of damage in mode shapes, frequency and damping in a single metric. Using changes in the impulse response as a damage sensitive feature has been used by other researchers [7, 8], however without imposing the spatial sparsity constraint explicitly. Using Vetter calculus, an analytical expression for the sensitivity of the impulse response is obtained and used to setup the inverse problem of detecting reductions in model parameters based on identified changes in impulse response. The inverse problem is effectively solved using LASSO regularization, an efficient l_1-based optimization scheme.

The paper begins by presenting the systems of interest and the method of approach. This is followed by a brief section on LASSO regularization and then a section on implementation and verification. The numerical implementation is carried out using a shear-beam structure with 21 degrees of freedom. In all cases, limited spectral data and noise-contaminated single input-single output (SISO) are considered. The paper ends with a section investigating the effects of model error and conclusions.

C. Smith • E.M. Hernandez (✉)
College of Engineering and Mathematical Sciences, University of Vermont, Burlington, VT 05405, USA
e-mail: csmith24@uvm.edu; eric.hernandez@uvm.edu

C. Niezrecki (ed.), *Structural Health Monitoring & Damage Detection, Volume 7*, Conference Proceedings of the Society for Experimental Mechanics Series, DOI 10.1007/978-3-319-54109-9_1

1.2 Method of Approach

The sensitivity approach is a popular and practical framework for finite model updating in structural dynamics [9]. The sensitivity matrix maps mass, stiffness and(or) damping parameters to associated changes in system response characteristics, typically variations in eigenvectors and eigenvalues [9]. In this paper, we seek a relationship between small changes in the impulse response to small changes in the parameters that define the stiffness matrix.

The impulse response of a linear system described by

$$h(t,\theta) = \int_0^t \mathbf{C}(\theta)\, e^{A(\theta)(t-\tau)}\mathbf{B}(\theta)\,\delta(\tau)\,d\tau = \mathbf{C}(\theta)\, e^{A(\theta)t}\mathbf{B}(\theta) + \mathbf{D}\delta(t) \tag{1.1}$$

where **A**, **B**, **C**, and **D** are the matrices that define the state-space model of the system. We seek to find

$$\Delta h(t) = \mathbf{S}(t)\Delta\theta \tag{1.2}$$

where $\Delta\theta \in R^{p\times 1}$ is a vector of changes in the p parameters that define the stiffness of the structure, $\mathbf{S} \in R^{mxp}$ is the impulse response sensitivity matrix, $\Delta h(t) \in R^{m\times 1}$ is the corresponding change in the impulse response between damaged and undamaged states, and m is the number of output multiplied times the number of time steps.

We restrict our attention to the case where the stiffness can be expressed as

$$\mathbf{K} = \sum_{i=1}^{p} \mathbf{E}_{i,K} f_i(\theta) \tag{1.3}$$

where **E** is an elementary influence matrix and $f_i(\cdot)$ is a differentiable function. By taking the first term of the Taylor series expansion around the parameter of interest, the stiffness and damping matrices may be written as

$$\mathbf{K} = \sum_{i=1}^{p} \mathbf{E}_{i,K}\theta \tag{1.4}$$

where the sensitivity matrix is defined as the derivative of the impulse response with respect to a change in parameter θ, written as

$$\mathbf{S}(t,\theta) = \frac{\partial h(t,\theta)}{\partial\theta} = \frac{\partial}{\partial\theta}\left(\mathbf{C}(\theta)\, e^{\mathbf{A}(\theta)t}\mathbf{B}(\theta) + \mathbf{D}\delta(t)\right) \tag{1.5}$$

The matrices **A**, **B**, **C**, and **D** are written as (for acceleration measurements)

$$\mathbf{A} = \begin{bmatrix} 0 & \mathbf{I} \\ -\mathbf{M}^{-1}\mathbf{K}(\theta) & -\mathbf{M}^{-1}\mathbf{C_d}(\theta) \end{bmatrix}, \quad \mathbf{B} = \begin{bmatrix} 0 \\ \mathbf{M}^{-1}b_2 \end{bmatrix}, \quad \mathbf{C} = c_2\left[-\mathbf{M}^{-1}\mathbf{K}(\theta) \;\; -\mathbf{M}^{-1}\mathbf{C_d}(\theta)\right], \quad \mathbf{D} = c_2\mathbf{M}^{-1}b_2 \tag{1.6}$$

b_2 and c_2 are respectively the input and output influence matrices, and $\mathbf{M} = \mathbf{M}^T \in R^{nxn}$, $\mathbf{C}_d = \mathbf{C}_d{}^T \in R^{nxn}$, and $\mathbf{K} = \mathbf{K}^T \in R^{nxn}$ are the mass, damping and stiffness matrices. The derivative of the exponential mapping in Eq. (1.1) can be found using results from Vetter [10] and Brewer [11]. Applying the chain rule from Vetter's calculus the sensitivity is written as

$$\frac{\partial h(t,\theta)}{\partial\theta} = \frac{\partial\mathbf{C}}{\partial\theta}e^{\mathbf{A}t}\mathbf{B} + \left(\mathbf{I}_p \otimes \mathbf{C}\right)\frac{\partial e^{\mathbf{A}t}}{\partial\theta}\mathbf{B} + \left(\mathbf{I}_p \otimes \left(\mathbf{C}e^{\mathbf{A}t}\right)\right)\frac{\partial\mathbf{B}}{\partial\theta} + \frac{\partial\mathbf{D}}{\partial\theta} \tag{1.7}$$

Such that

$$\frac{\partial\mathbf{A}}{\partial\theta_i} = \begin{bmatrix} 0 & \mathbf{I} \\ -\mathbf{M}^{-1}\mathbf{E}_{i,K} & -\mathbf{M}^{-1}\mathbf{E}_{i,C_d} \end{bmatrix}, \quad \frac{\partial\mathbf{C}}{\partial\theta_i} = c_2\left[-\mathbf{M}^{-1}\theta_i \;\; -\mathbf{M}^{-1}\theta_i\right], \quad \frac{\partial\mathbf{B}}{\partial\theta_i} = 0, \frac{\partial\mathbf{D}}{\partial\theta_i} = 0 \tag{1.8}$$

where $\otimes$ is the Kronecker product. In the case that $\mathbf{C}$ is a function of θ, then Eq. (1.7) is reduced to

$$\frac{\partial h(t,\theta)}{\partial \theta} = \frac{\partial \mathbf{C}}{\partial \theta} e^{\mathbf{A}t}\mathbf{B} + \left(\mathbf{I}_p \otimes \mathbf{C}\right) \frac{\partial e^{\mathbf{A}t}}{\partial \theta}\mathbf{B} \tag{1.9}$$

Applying Brewer's derivative of a matrix exponential we obtain

$$\frac{\partial e^{\mathbf{A}(\theta)t}}{\partial \theta} = \sum_{k}^{2n}\sum_{l}^{2n} \left(\mathbf{I}_1 \otimes \alpha_k \gamma_k^*\right) \frac{\partial \mathbf{A}}{\partial \theta} \left(\mathbf{I}_p \otimes \alpha_l \gamma_l^*\right) f_{kl}(t),\ f_{kl}(t) = \begin{cases} te^{\lambda_k t} & \text{if } \lambda_k = \lambda_l \\ \frac{e^{\lambda_l t} - e^{\lambda_k t}}{\lambda_l - \lambda_k} & \text{if } \lambda_k \neq \lambda_l \end{cases} \tag{1.10}$$

where α is the eigenvectors of $\mathbf{A}$ and γ is the eigenvectors of $\mathbf{A}^T$ which are normalized such that

$$\gamma_k^* \alpha_k = 1 \tag{1.11}$$

In order to be consistent with the spectral bandwidth of the identified impulse response used to compute Δh the sensitivity matrix is truncated at the maximum number of identified frequencies. Using the spectral representation of an exponential mapping, the truncation at the specified eigenvalueλ_r, where $r < n$, is defined as

$$e^{\mathbf{A}t} = \sum_{k=1}^{2r} \alpha_k \gamma_k^* e^{\lambda_k t} \tag{1.12}$$

where α and γ are normalized according to Eq. (1.11).

1.3 LASSO Regularization

In 1996, R. Tibshirani proposed a new method (LASSO regression) for estimating linear models which seeks to minimize the following residual function

$$\min_{x \in R^p} \frac{1}{2}\|y - Ax\|_2^2 + \lambda \|x\|_1 \tag{1.13}$$

with regularization parameter $\lambda \geq 0$ [12]. LASSO typically recovers sparse solution due to the l_1-norm constraint. For experimental demonstrations we use the Matlab package, Lasso and Elastic-Net Regularized Generalized Linear Models (glmnet), an efficient procedure for fitting the lasso regularization path for linear regression [13]. The algorithm uses cyclical coordinate descent computed along a regularization path to optimize the objective function over each parameter with others fixed, and cycles repeatedly until convergence [13].

The choice of the regularization parameter is subject to the user, where larger values of λ tend to sparse solutions. To exclude user bias to the known solution, we use the glmnet's built in cross validation algorithm to select a value of λ. The cross validation uses tenfold. We constrain the maximum number of nonzero elements in x to about 20% the number of degrees of the system of interest.

1.4 Simulations and Verification

The simulated experiment shall validate our methodology that seeking small localized damages with a sparsity prior will yield more accurate and illustrative results than without (i.e. l_2 regularization). The simulation is an ideal case because the model used to generate the data is also the one used to implement the algorithm.

The simulated model is a 21 degree of freedom, non-uniform shear beam with degrees of freedom enumerated from 1 the first mass closest to the support, to 21 the free end. The spring stiffness are as follows: $k_1 = \ldots = k_7 = 1000$, $k_8 = \ldots = k_{14} = 750$, and $k_{15} = \ldots = k_{21} = 500$, and the masses: $m_1 = \ldots = m_7 = 1$, $m_8 = \ldots = m_{14} = 0.75$, and $m_{15} = \ldots = m_{21} = 0.5$. The structure is classically damped with a damping coefficient of 0.01. The fundamental frequency is 0.436 Hz.

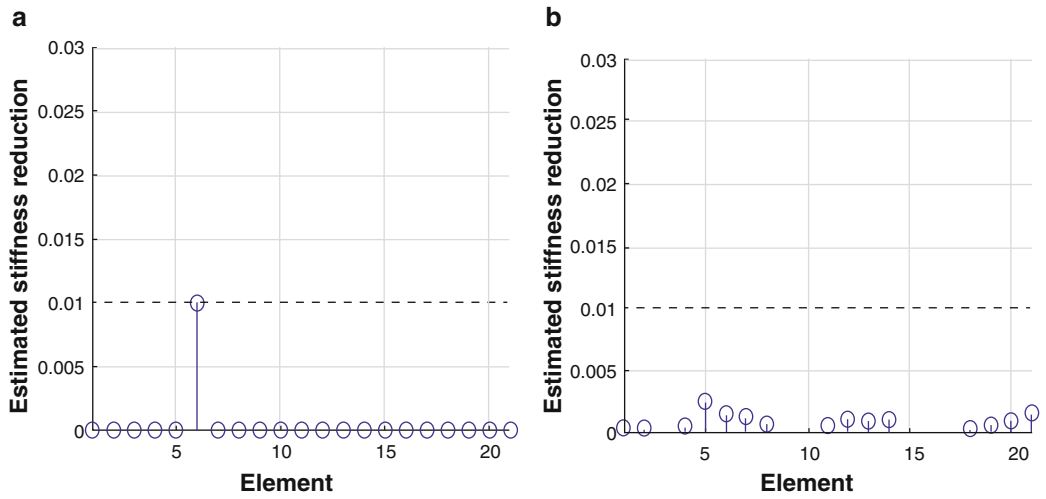

Fig. 1.1 Estimated stiffness reduction for every element. In this case, only the stiffness of El. 6 was reduced by 1%. (**a**) The l_1-based solution, and (**b**) the l_2-based solution

Stiffness is the only damage sensitive parameter and the sensitivity matrix is defined by Eq. (1.9). The change in impulse response between the damaged and undamaged system contain only the specified lower frequencies, which are typically the only ones that can be identified from structural vibrations. The input sensor is fixed at El. 21 and the output sensor fixed at El. 3 for all subsequent experiments. Our objective is: (1) to show how the LASSO regularization compares to the Tikhonov regularization in detecting changes in stiffness, (2) present the minimum number of frequencies required to detect a reduction in stiffness at a specified location, and (3) show the effects of identification errors (noise) on the probability of detection (POD).

In the first simulation, the stiffness of El. 6 is reduced by 1% and the lowest four frequencies are identified within the impulse responses of the original system and the damaged system. No prior information about the quantity or magnitude of damages are known except that the solution is sparse. As described above, the system is single input and single output, and the sensitivity matrix is truncated according to the number of identified frequencies (Eqs. (1.10) and (1.12)). The LASSO regularization (Eq. (1.13)) is used to estimate the reduction in stiffness and its location. The results are compared to the solution of the Tikhonov regularization (Fig. 1.1).

It is immediately clear that the l_1 constrained solution identifies the true damaged element, and estimates the magnitude of the reduction in stiffness precisely. In stark contrast, no information is gained about the damaged element when the regularization is subjected to the l_2 constrained parameter nor is the solution sparse. The solution to the LASSO has only one non-zero element and hence is sparse.

The performance of the l_1 constrained regularization method in detecting a 1% stiffness reduction in any single element taken separately is considered. Figure 1.2a presents the minimum number of frequencies required to identify this reduction at any single element. The impulse response sensitivity method and frequency sensitivity method are compared. Frequencies are selected sequentially from the lowest in increments of one until a proper detection is obtained. Figure 1.2b presents the estimated stiffness reduction by the l_1 regularization for the case where only four frequencies were identified. We compare the sparse sensitivity method with frequency shifts from [5], to the sparse sensitivity method with impulse responses. Clearly, the number of identifiable frequencies required to detect a single damage is far less in the impulse method.

We consider now the case with multiple damage locations and varying percent reduction in stiffness. In this case, the impulse response and sensitivity matrix were truncated at the sixth frequency. Figure 1.3 presents the following scenarios: (1) the stiffness of El. 6 reduced by 1% and El. 15 by 1%, (2) stiffness of El. 6 reduced by 1% and El. 15 by 3%, and (3) El. 6 reduced by 1% and El. 15 by 5%. In cases (1) and (2) damages were correctly located, and their reductions in stiffness accurately estimated. In case (3) a false positive is obtained at El. 19 and the estimated magnitudes of the stiffness reduction at the true damage locations shrink in value. This may be due to the greater reduction in stiffness which drives the error between the linear approximation and the true nonlinearity of the sensitivity. We require small changes in stiffness so that the changes in impulse response are contained within the linear span of the sensitivity matrix.

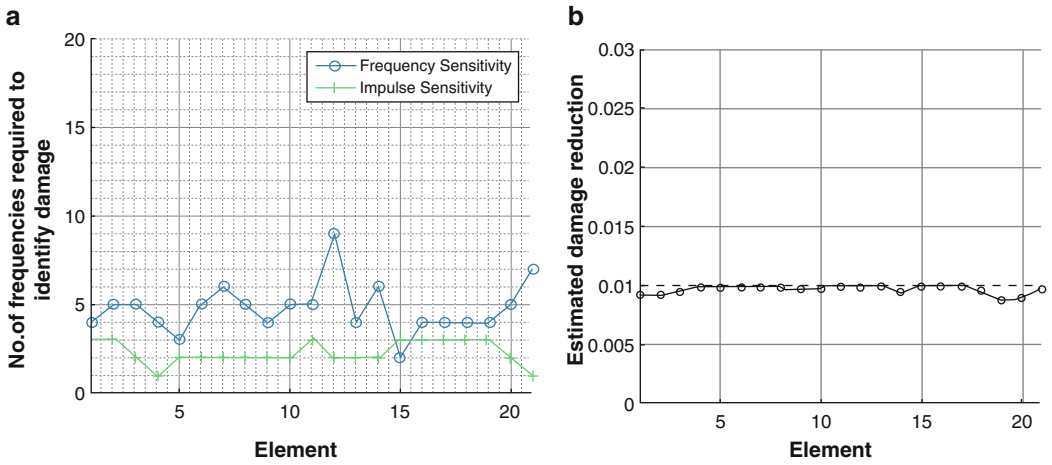

Fig. 1.2 (**a**) Number of frequencies required in order to identify a single element damage. Frequencies selected sequentially from the lowest in increments of one until a proper detection is obtained. (**b**) Estimated stiffness reduction for every element [5]

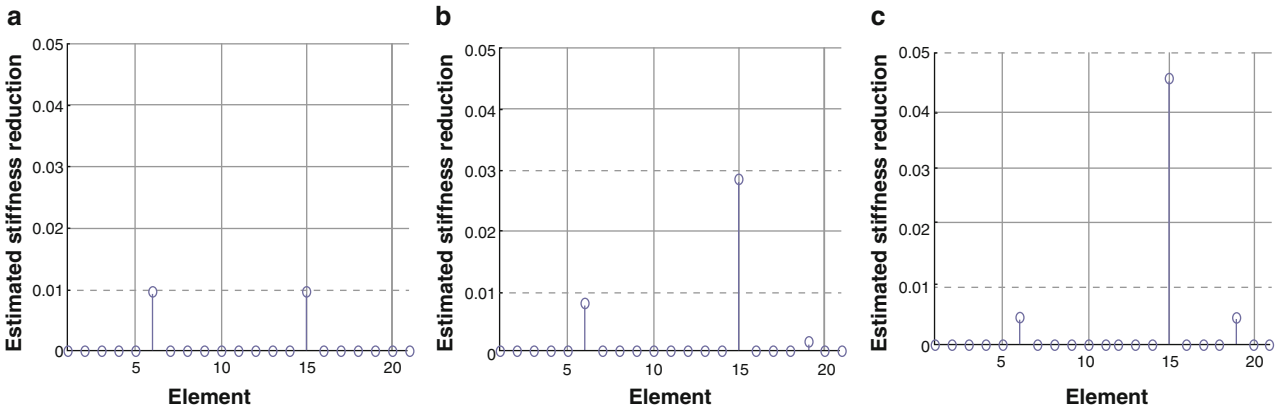

Fig. 1.3 Estimated stiffness reduction for the following multiple damage cases: (**a**) 1% damage at El. 6 and El. 15, (**b**) 1% damage at El. 6 and 3% at El. 15, (**c**) and 1% damage at El. 6 and 5% damage at El. 15

1.5 Effects of Measurement Noise

The effects of measurement noise ϵ on Eq. (1.2) are investigated. ϵ is defined as the realization of an n-dimensional Gaussian random vector with zero mean and standard deviation of each component ϵ_i proportional to the corresponding $h(t_i)$, where n is length of the vector of time. In this scenario, the vector of noise is added to the measured output for both damaged and undamaged states. The impulse responses are then identified from the simulated outputs given a white Gaussian input using the Observer/Kalman Filter Identification (OKID). The number of identified frequencies in the spectral bandwidth of the impulse response varied from 4 to 10. The location of the input was held at El. 21, and the output at El. 3. In each case, 1000 simulations were performed and a probability of detection (POD) was obtained. The criteria for detection were: (1) the method correctly identifies the damaged element, and (2) it does not assign a value greater than 20 percent than that of the element of greatest reduction to any other element. To reduce the effects of noise from the identified damping which is often more sensitive to noise than other dynamic features, we consider only the identified impulse response between $2.5''$ and $27.5''$.

The POD is compared to those obtained from [5] for a single 10% stiffness reduction at El. 2, El. 6, El. 14, and El. 20. Figure 1.4 presents the POD for each case as a function of the maximum coefficient of variation of the identified frequencies. It is clear that the impulse response method results in much better POD values than the frequency sensitivity method for El. 2, 6, and 14. The behavior of the POD at El. 20 is yet to be explained.

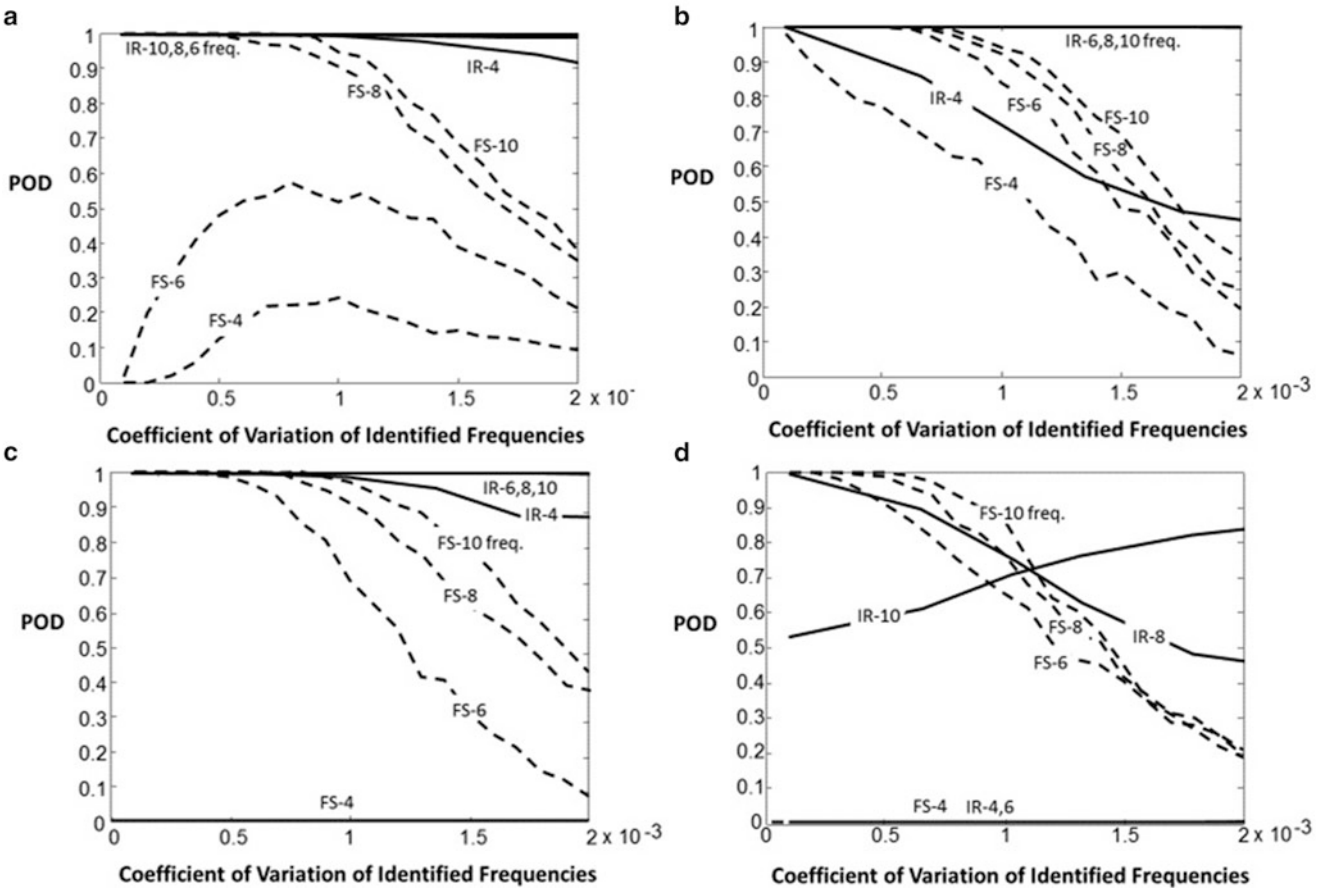

Fig. 1.4 Probability of detection (POD) as a function of the coefficient of variation of the selected frequencies for impulse response (IR) and frequency sensitivity (FS) method [5]. (**a**) Corresponds to spring 2, (**b**) to spring 6, (**c**) to spring 14, and (**d**) to spring 20

1.6 Conclusion

This paper explores the use of the impulse response sensitivity for detecting spatially sparse damage. The paper shows that it is possible to detect spatially sparse stiffness reductions in the presence of noise and limited spectral data by measuring changes in impulse response with single input single output systems. In setting up the problem, the sensitivity of the impulse response with respect to changes in damage sensitivity parameters was found using Vetter calculus. Finally, the proposed method is compared to frequency sensitivity methods from [5], and the results clearly show the advantage of the proposed method. Future work will explore the effects of optimized input/output locations, multi-input multi-output systems, varying magnitudes of damage, and the robustness of the proposed algorithm to modeling errors.

References

1. Doebling, S., Farrar, C., Prime, M. and Shevitz, D. Damage identification and health monitoring of structural and mechanical systems from changes in their vibration characteristics: A literature review. Los Alamos National Laboratories Report (LA-13070-MS) (1996)
2. Sohn, H., Farrar, C. Hemez, F., Shunk, D., Stinemates, D. and Nadler, B. A review of structural health monitoring literature: 1996–2001. Los Alamos National Laboratories Report (LA-13070-MS) (2003)
3. Kaouk, M., Zimmerman, D.C.: Structural damage assessment using a generalized minimum rank perturbation theory. AIAA J. **32**(4), 836–842 (1994)
4. Link, R.J., Zimmerman, D.C.: Structural damage diagnosis using frequency response functions and orthogonal matching pursuit: theoretical development. Struct. Control. Health Monit. **22**, 889–902 (2015)
5. Hernandez, E.M.: Identification of isolated structural damage from incomplete spectrum information using L1-norm minimization. Mech. Syst. Signal Process. **46**(1), 59–69 (2014)

6. Hernandez, E.M.: Identification of localized structural damage from highly incomplete modal information: theory and experiments. ASCE J. Eng. Mech. **142**(2), 04015075 (2016)
7. Hassiotis, S.: Identification of damage using natural frequencies and Markov parameters. Comput. Struct. **74**(3), 365–373 (2000)
8. Law, S.S., Li, X.Y.: Wavelet-based sensitivity analysis of the impulse response function for damage detection. J. Appl. Mech. **74**, 375–377 (2007)
9. Mottershead, J.E., Link, M., Friswell, M.: The sensitivity method in finite element model updating. A tutorial. Mech. Syst. Signal Process. **25**(7), 2275–2296 (2011)
10. Vetter, W.J.: Derivative operations on matrices. IEEE Trans. Autom. Control. **15**(4), 241–244 (1970)
11. Brewer, J.: The derivative of the exponential matrix with respect to a matrix. IEEE Trans. Inf. Theory. **22**(4), 656–657 (1977)
12. Tibshirani, R.: Regression shrinkage and selection via the lasso. J. R. Stat. Soc. B. **58**(1), 267–288 (1996)
13. Friedman, J., Hastie, T., Tibshirani, R.: Regularization paths for generalized linear models via coordinate descent. J. Stat. Softw. **33**(1), 1–22 (2010)

Chapter 2
Multi-Source Sensing and Analysis for Machine-Array Condition Monitoring

Shannon M. Danforth, Jaden T. Martz, Alison H. Root, Eric B. Flynn, and Dustin Y. Harvey

Abstract Early detection of damage in machines can eliminate the expenses and safety hazards associated with failure. Current methods use distributed systems to monitor individual machines, but the associated costs of instrumentation, data acquisition hardware, and facility retrofits are high. A centralized, remote, multi-source monitoring system would increase both the cost efficiency and ease of user operation. This study investigates how data from multiple sensing streams can best be utilized for decision making processes and to what extent a remote, centralized instrumentation package can effectively monitor multiple machines. An array of duct fans was used in this study to represent an arbitrary set of systems from which data can be collected and fused. Data was acquired using multiple measurement types (vibrations, acoustics, current, voltage, RF) using a centralized instrumentation system. The voltage and current were measured from the single supply used to power the fan array. The remaining sensors, including an accelerometer, microphone, and antenna, were placed in a single, central location among the array of fans. Data analysis focused on determining whether separate, nominally identical machines could be uniquely identified and characterized from measurements. Spectral analysis and signature development were used to characterize the state of each machine. These methods can be implemented in other applications involving the fusion of data from several sources to obtain information about the identification, location, and characterization of one or more dynamic systems.

Keywords Condition monitoring • Remote sensing • Data fusion • Machine learning • Machine array

2.1 Introduction

The development and implementation of condition monitoring has gained popularity in recent years due to society's increasing dependence on rotating machinery. As regularly replacing all aging mechanical systems would be costly, condition monitoring techniques aim to ensure that these machines can safely remain in operation [1]. Condition monitoring systems are designed to detect damage as early as possible by identifying altered characteristics in the machine's dynamic response [2].

Systems of rotating machinery are typically monitored using individual sensors (one or more per machine), but these distributed health monitoring systems result in an increased cost of acquiring data, installing the devices, and repairing the monitoring system. This study investigates the effectiveness of a centralized, remote, multi-source condition monitoring system for an array of machines. The utilization of data from multiple sources aims to increase the accuracy of identification and characterization.

S.M. Danforth
University of Portland, 5000 N Willamette Blvd, Portland, OR 97203, USA
e-mail: danforth16@up.edu

J.T. Martz
Pennsylvania State University, 201 Old Main, University Park, PA 16802, USA
e-mail: jtm2114@gmail.com

A.H. Root
Case Western Reserve University, 10900 Euclid Ave, Cleveland, OH 44106, USA
e-mail: alison.root@case.edu

E.B. Flynn • D.Y. Harvey (✉)
Los Alamos National Laboratory, P.O. Box 1663, Los Alamos, NM 87545, USA
e-mail: eflynn@lanl.gov; harveydy@lanl.gov

C. Niezrecki (ed.), *Structural Health Monitoring & Damage Detection, Volume 7*, Conference Proceedings of the Society for Experimental Mechanics Series, DOI 10.1007/978-3-319-54109-9_2

The study explores how well the remote, centralized system can identify and characterize a damaged machine among the array. The techniques for multi-source data fusion, as well as identification and characterization of one damaged machine among an array, could be generalized to other applications in order to increase the effectiveness of combining multi-source data to make decisions.

2.2 Background

In comparison to a time-based maintenance approach, where the health of machines is planned and investigated periodically, or a reaction-based approach, where machines remain in operation until failure occurs, condition-based monitoring provides a safe, economical method of machine maintenance [3]. Most generally, condition monitoring refers to the implementation of a damage detecting system for rotating machinery [1]. The process of condition monitoring involves several steps: collecting dynamic response data at periodic times, extracting features from the data, and using statistical methods to determine if the system is in a healthy or unhealthy state [2].

Approaches for monitoring the health of a dynamic system focus on either data-based or model-based techniques. Data-based approaches aim to "learn" characteristics of healthy and unhealthy system states using measured data. A statistical model of the system is developed to identify when damage has occurred. The model-based approach typically involves finite element modeling, but also requires initial data from the system in order to improve accuracy [1]. Because it does not necessitate a physical model and instead relies on pattern recognition algorithms, the data-based approach is favorable; however, its otherwise purely empirical model can be strengthened by a knowledge of physical relationships.

Condition monitoring is a relatively mature area within the field of structural health monitoring [4]. Various methods of monitoring have been developed that utilize the thermal, chemical, electrical, or mechanical properties of the system in order to detect specific types of damage [5–9]. Vibration measurements have been used extensively in condition monitoring; the acceleration data is used as input for techniques that track changes in the system dynamics using pattern recognition [9] or to identify damage through knowledge of the physical relationships between the output signals from the stator, rotor, and shaft bearings [10].

Currently, condition monitoring for multiple machines utilize distributed sensor networks, where one or more sensors are applied to each individual machine in order to characterize its health [11]. However, in applications with a large array of machines, dedicating a sensor to each entity is expensive. Associated costs include the sensors and the utilities necessary to power the sensors, the storage and processing of multiple channels of data, and the cost of maintenance or retrofit to the condition monitoring equipment [12].

When implementing a condition monitoring system, one must identify its objectives, develop a definition of damage, identify the conditions in the operating environment, and acknowledge the limitations for data collection in these surroundings. This operational evaluation stage helps determine the appropriate sensor network to use for the specific condition monitoring application [1]. Many types of sensors can be used to measure quantities such as acceleration, strain, force, or temperature.

Multi-source data fusion has become increasingly relevant in applications such as robotics, medicine, military threat recognition, and battlefield surveillance. Data from multiple sources can improve a system's accuracy in identifying and characterizing any dynamic entity [13]. The method of acquiring, processing, and combining data from multiple sources can provide a more accurate assessment of the system being monitored, and recent advances in sensing technology and data processing have placed an emphasis on this practice [14]. The multi-source sensing system can provide the most amount of information if the sensors measure different physical phenomena, but fusing the data from sources that are not commensurate adds complexity to the processing flow. Additionally, if the information from a certain sensor is biased or inaccurate, the resulting decision can be skewed [13].

The fusion of data can take place at a variety of levels. For any particular multi-source application, a central question is at what point in the procedure the data should be combined in order to extract the maximum amount of accurate information. If the sensors all measure the same physical quantities, the data may be fused at the raw level; however, non-commensurate data must be fused later in the processing flow [13].

Machine learning is a common and effective way to combine data from multiple sources at the feature level. In condition monitoring applications, features are extracted from each data stream, then concatenated and used in a pattern recognition algorithm to identify changes in the system's dynamic response [13]. A machine learning network can either be supervised or unsupervised, depending if information is known about the system being monitored in multiple states or only one [1].

Data fusion can also take place at the decision level, where a decision is made using the data from each individual sensor and then fused in order to make an overall inference about the state of the system. The decisions can be combined using

voting methods, where "majority rules" techniques are used to make an overall assessment [15]. Probabilistic fusion is a sophisticated method of decision-level fusion where the probability of an event occurrence is calculated from each sensor output; these values are merged to create an overall decision of the system state [16].

The system developed in this study aims to monitor an array of nominally identical machines from a centralized location. The added complexity of an array of fans in this monitoring system may render the independent processing of each sensor domain ineffective. The authors of this paper believe the relationships between each sensor domain should be utilized in order to provide more specific inferences for identifying and characterizing damage. The study investigates to what extent this monitoring system will be able to identify damage in one machine among the array.

2.3 Experimental Setup and Procedures

The array of machines consisted of four Apollo Horticulture 4-in. 190 CFM inline duct fans connected to a power strip, allowing the fans to run in parallel. Each had a variable speed controller. Several sensors were considered for measuring the fans. These included an accelerometer, microphone, current and voltage probe, antenna, and a magnetic field sensor.

The accelerometer was the first sensor considered because of its wide use in condition monitoring techniques. Based on the literature, accelerometer data should provide information for characterizing mechanical damage of a motor and indicating shaft speed [9]. To perform the experiments, a PCB 352C22 was used with an operating range of 1 Hz–10 kHz and a sensitivity of 10 mV/g. The sensor was sampled at 20 kS/s.

In an environment of rotating machinery, airborne acoustics are prevalent. As it was anticipated that damaged components would show symptoms through subtle auditory variations, a microphone was included in the sensor collection. A PCB 130A24 was used with a frequency range of 20 Hz–16 kHz and a sensitivity of 10 mV/Pa. A sampling rate of 20 kS/s was chosen based on the lack of substantial content beyond 10 kHz during initial data collection. This observation is supported by the understanding that an increase in sound wave frequency greatly increases the attenuation of sound in air as well as reduces the ability of the wave to diffract [17]. For the application of the study, the sound signal could likely be traveling around obstacles for distances greater than what could be reasonably detected after the resulting attenuation.

The current probe was chosen to establish a basis for the electric signature, allowing the system to highlight differences in the electrical response of the machine array and potential electrical damage. A current transformer was used at the wall source for measurements, with a sensitivity of 1.3 V/A and sample rate of 200 kHz.

The voltage probe was used to complete the electric signature. It was not expected that the voltage measurement alone would provide much information on the subtleties of the system, but could be useful when combined with data from other sensors. The voltage was measured at the wall using a voltage divider with a sensitivity of 1/33 V/V and a sample rate of 200 kHz.

The antenna provided a way to supplement the electrical signature of the system through a non-contact channel. Additionally, because electromagnetic radiation attenuates less with regards to distance or obstructions at low frequencies, this sensor was expected to be more useful in a wider range of environments [18]. An L-400B LF antenna was used with a frequency response of 10–500 kHz and a sensitivity of −3 dB at 250 kHz. The data was sampled at 200 kS/s due to the sampling rate limit on the data acquisition unit.

An Ametes MFS was used to measure the magnetic field generated by the motor. Measurements were taken in three axes at a sensitivity of 280 mV/mT over a field range of ±7.3 mT and a sample rate of 200 kHz. After preliminary testing, it was found that the sensor was not sensitive enough to measure magnetic field emanations from the fans beyond a few inches. As the sensing system aimed to be remote, this relatively small range was not effective for the application of the study. The sensor was discarded from the experimental procedure.

The sensors were fed into a National Instruments PXIe-1073 data acquisition unit capable of a 204.8 kHz maximum sample rate. Figure 2.1 shows the sensor and fan array locations in the final setup.

The total collection process spanned a 2-month period with collections taken at various times during the work day. Data was collected in 1-min intervals in order to provide adequate frequency resolution for spectral-based signatures. Five discrete fan speeds were defined for data collection: low, medium-low, medium, medium-high, and high. The fans were labeled A–D and clamped to the table at their base. No other devices were present on the table; however, other mechanical and electrical signal sources were present in the laboratory and neighboring laboratories, including significant RF signals from the light fixtures. The interference from the lights was removed by turning them off during collection.

Data was collected with each fan running separately at each speed to characterize the frequency content of the fans. These individual tests were performed several times in order to validate the trends observed during the analysis stage. Data collected from combinations of fans running at various speeds was used to test the condition monitoring model. Figure 2.2 shows an example of the raw time response and the PSD for microphone data.

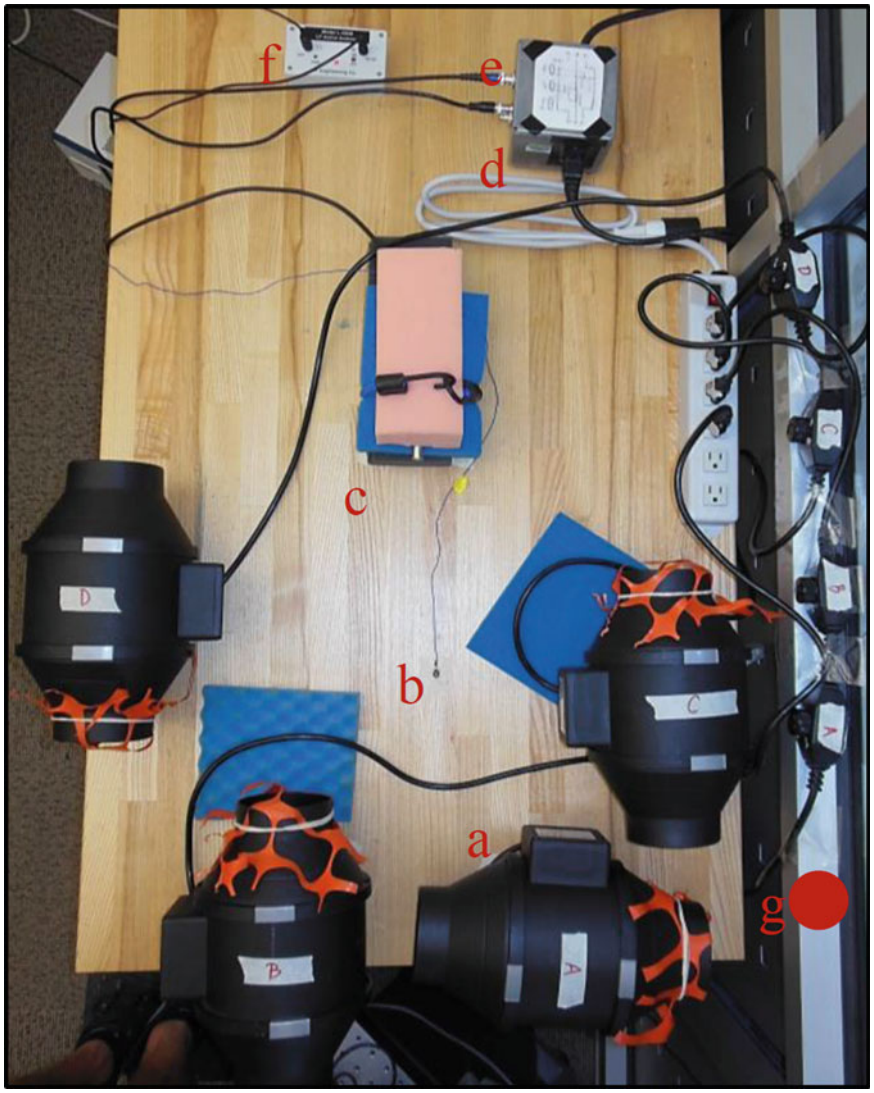

Fig. 2.1 Components of experimental setup, including (**a**) fan array, (**b**) accelerometer, (**c**) microphone, (**d**) current probe, (**e**) voltage probe (**f**) RF amplifier (**g**) RF antenna (positioned above setup)

Simulated damage was introduced into the system by either loosening screws on the motor frame or adding lumped mass to individual fan blades. The fans were disassembled and reassembled many times to induce these damage conditions.

2.4 Analysis Approaches

In order to identify damage in the fan array, several methods for utilizing the data from each sensor stream were explored and evaluated. Given a data set collected with any combination of fans in operation, the first goal of analysis focused on utilizing the multi-source data to indicate which fans were running in a healthy state. Blind source separation, the initial attempt at data analysis, used measured mixture signals to produce time signals from each source. Next, a linear least squares method was used to generate a state vector indicating the number of operating fans. The same fingerprints were applied in a brute force optimization method, aiming to identify the smallest error between a given data set and a collection of consistent fingerprints from each machine. Lastly, three different detector methods used the statistics generated from data collection to characterize the fan array. Of all the methods, the third detector method proved to be the most effective.

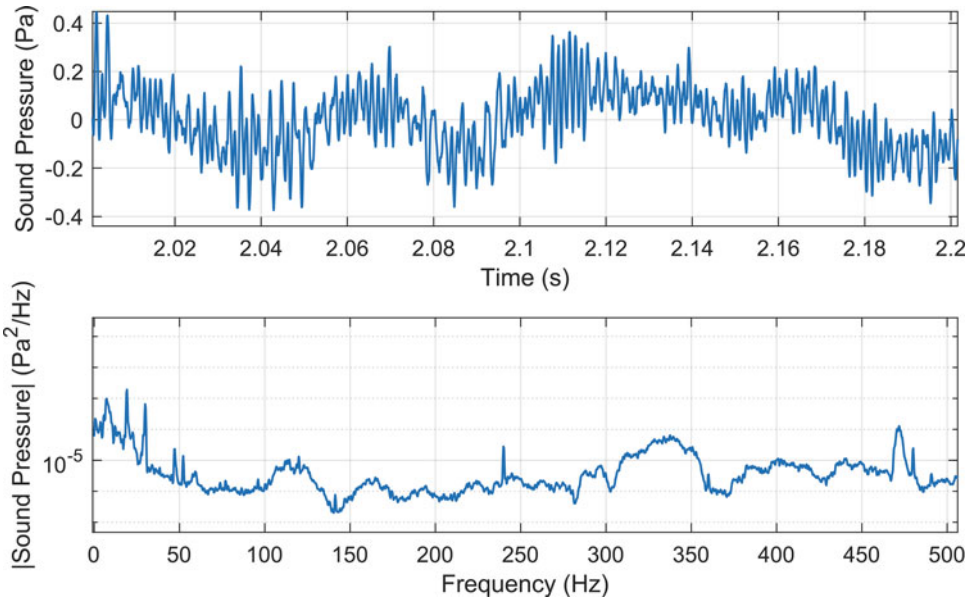

Fig. 2.2 Raw time response and power spectral density estimate for microphone data

2.5 Blind Source Separation

An attempt at recovering the source signals from each fan in the array was made using Blind Source Separation (BSS). One BSS technique applies Independent Component Analysis (ICA) to produce time signals from each independent source given measured mixture signals [19]. However, this method is effective only when the number of sensors is equal to the number of sources. In the case where the number of source signals outnumbers the number of sensors, alternative BSS methods such as clustering approaches and Sparse Component Analysis (SCA) have been developed [20–24]. Typically, commensurate sensor data are used; however, only one of each sensor type was present in this study. The sparse clustering approach was implemented with non-commensurate data, and it was determined that BSS methods were not able to provide the desired source signals.

2.6 Linear Least Squares

A linear least-squares approach investigated to what extent the root mean square (RMS) values of the time response from each sensor would prove effective in distinguishing between the four fans in the experiment and identifying an individual fan's speed. For m sensors, The RMS of the time response was calculated and used as a signature for n distinct characteristics (for example, specific fans or fan speeds). These values were averaged over several data sets and placed in an $m \times n$ signature matrix $\mathbf{A}$. Given new data, the RMS from each sensor's time data was computed and placed in an $m \times 1$ vector $\mathbf{b}$. The theoretical relationship between the two are related as follows:

$$\boldsymbol{Ax} = \boldsymbol{b} \tag{2.1}$$

The system state vector $\mathbf{x}$ was then back-solved for using linear least squares.

Due to the nonlinear relationship between the different system states and the RMS values over the entire 1-min time response, the linear least squares approach was not effective for this study. Figure 2.3 shows plots of RMS values versus fan speed for a specific fan and sensor over several data collection instances. It is clear that as fan speed increases, the RMS value does not necessarily increase; in some sensors, data does not follow a consistent trend at all. In Fig. 2.4, RMS trends for specific sensors are shown for different numbers of fans running. The RMS values do not add linearly when multiple fans are running at the same time, with the exception of current. The linear model failed to correctly identify specific fans at one speed and specific fan speeds for one fan.

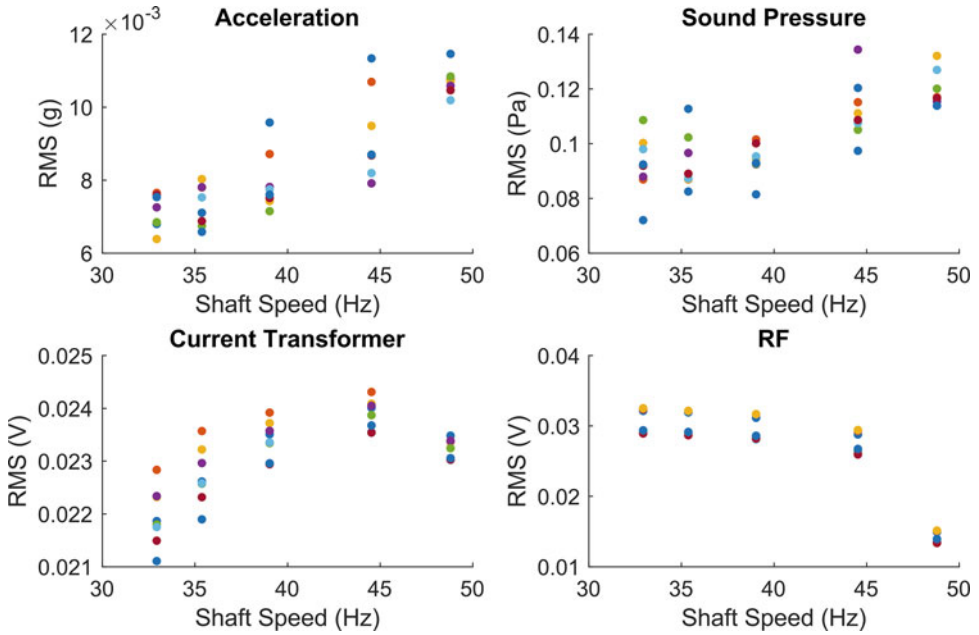

Fig. 2.3 RMS values for Fan C's five discrete shaft speeds for acceleration, sound pressure, current transformer, and radio frequency data. Each color represents a distinct data collection

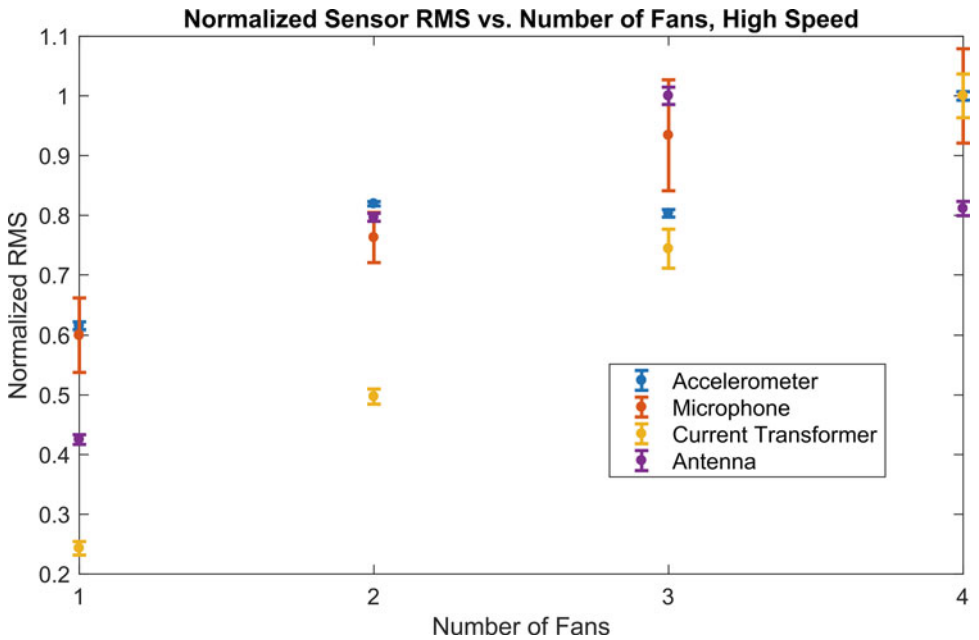

Fig. 2.4 RMS values for different numbers of fans running for acceleration, sound pressure, current transformer, and radio frequency data. The error bars represent one standard deviation from the mean

2.7 Brute-Force Optimization

A brute-force optimization approach was also explored for determining the state of each individual fan in the array. Each possible state of the system, represented as an $n \times 1$ vector of binary values, was tested using a similar $m \times n$ signatures matrix as in the previous method. The state that yielded the least error when compared to the data in question was determined to be the correct state of the system. The first attempt aimed to identify the speed (high, medium, or low; $n = 3$) of a known fan using the RMS value over the entire signal. The second attempt aimed to identify which fan was on (A, B, C, or D; $n = 4$) given signatures from a known speed, again using the RMS value over the whole time domain. The third attempt used

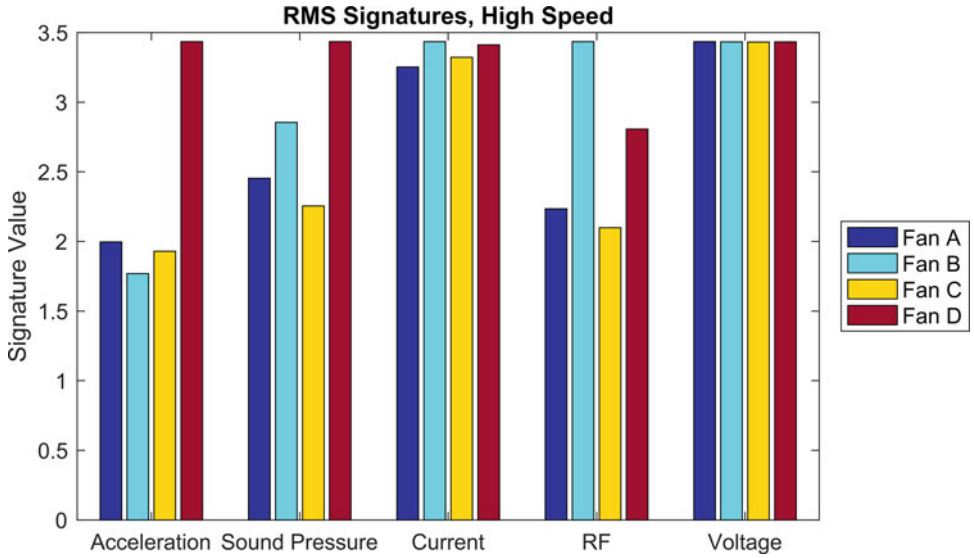

Fig. 2.5 Graphical representation of a signature matrix used to identify fans A–D at high speed

Table 2.1 Summary of brute force optimization results for a single fan running

Speed	Correct identification	Incorrect speed	Incorrect fan
High	16	0	0
Medium high	13	3	3
Medium	8	8	4
Medium low	12	4	8
Low	9	7	7
Total	58	22	22

The "Incorrect Speed" column indicates an instance where the correct fan was identified as present, but was labeled with the wrong speed. The "Incorrect Fan" column indicates an instance where the fan was wrongly identified but the speed that was identified was correct

different signatures than the previous two. The power values of small bandwidths of individual fan PSDs were computed and averaged over several data collection instances. These signatures were again used to identify an unknown fan running at a known speed.

Some applications of the brute-force optimization approach were more successful than others. In general, fan identification was much more difficult than speed identification. Most of the data from different fans running at the same speed was very similar; therefore, decisions made between fans were frequently under informed. Figure 2.5 provides a graphical representation of a signatures matrix for fans A–D at high speed when using RMS values constructed from the entire signal. Aside from Fan D's distinguishing RMS values in the acceleration and sound pressure categories, the fans are notably similar for each sensor domain, highlighting the ineffectiveness of using the RMS over the entire time response to identify an individual fan.

Implementing brute force with signatures constructed from the narrow-band power was accurate 76% of the time for a single fan running. However, when multiple fans in the system were operating, the brute-force approach was never correct.

Brute force optimization for fan speed identification was more successful, albeit not enough to be reliable. Identifying a fan in the high speed state was always correct. In general, identification accuracy decreased with fan speed apart from fans running at medium speed: they were incorrectly identified most frequently. The observed trend was likely due to the RMS values becoming more separable as fan speed increased. A summary of these results is shown in Table 2.1.

2.8 Machine Learning Approaches

The total power over small frequency ranges was also used as features in a machine learning approach. Unique, distinct peaks present in the PSD estimates, ranging across all sensor streams, were identified for each fan. Fourteen of these characteristic peaks were consistently found in the spectral data, despite the fans being nominally identical. Figure 2.6 shows an example of one such fingerprint for Fan C, present in the acceleration data from 650 to 660 Hz. Figure 2.7 shows a visual representation of the location of these signatures in frequency space. The fingerprints are also summarized in Table 2.2. The large blue band in Fan B ranging from 7000 to 10,000 Hz is the power computed over this entire range. This signature was added after observing that Fan B was significantly louder than the other three fans, and thus had a larger power value at higher frequencies. The power over these bands was calculated. The signatures were meant to create a fingerprint of a healthy fan, which would be absent if the motor dies or became damaged. Over 150 sets of minute-long data streams were averaged to find these signatures. The model's effectiveness was assessed using leave-one-out cross-validation.

Three detectors were investigated to determine whether these RMS values indicated the presence of each fan in a particular set of data. These detectors were implemented individually and judged as correctly characterizing the entire system when, given a minute-long set of new data, they were able to correctly identify which fans were on and off among the array. Only high speed fan data was used in the training and testing data. The algorithms' effectiveness was assessed using leave-one-out cross-validation.

The first detector used a manually set threshold value based on the typical power computation of each fingerprint. In Fig. 2.8, a histogram for a certain signature provides a visual representation of trends observed in the data; these narrowband RMS value trends were used to determine the threshold.

This algorithm correctly characterized the entire system 86% of the time. Fans A, B, and C were correctly identified as on or off 97% of the time. The presence of Fan D was correctly indicated just under 90% of the time.

The second detector used was a threshold set statistically at one half of one standard deviation below the mean value for each signature. This method correctly characterized the entire fan array only 69% of the time. The presence of Fan C, however, was correctly indicated 99% of the time.

The final algorithm first computed the RMS of the entire current signal in order to determine the number of fans present in the measured data. Figure 2.9 shows the linear relationship between current RMS and the number of fans in operation. Once the mean value of each fan's signature was computed, the model computed the distance from this mean related to a particular fan when it is running and added them together to form a "signature match value". Based on the known number of fans in operation, the largest signature match value(s) would be selected and the corresponding fans would be indicated as present. The presence of a certain fan is more likely to yield a signature close to or above the mean value for that particular signature. Thus, adding the distance each signature for a particular fan is from the mean value of each signature will yield a number that is more positive when the fan is present. For example, if three fans were present in the measured data, the three fans

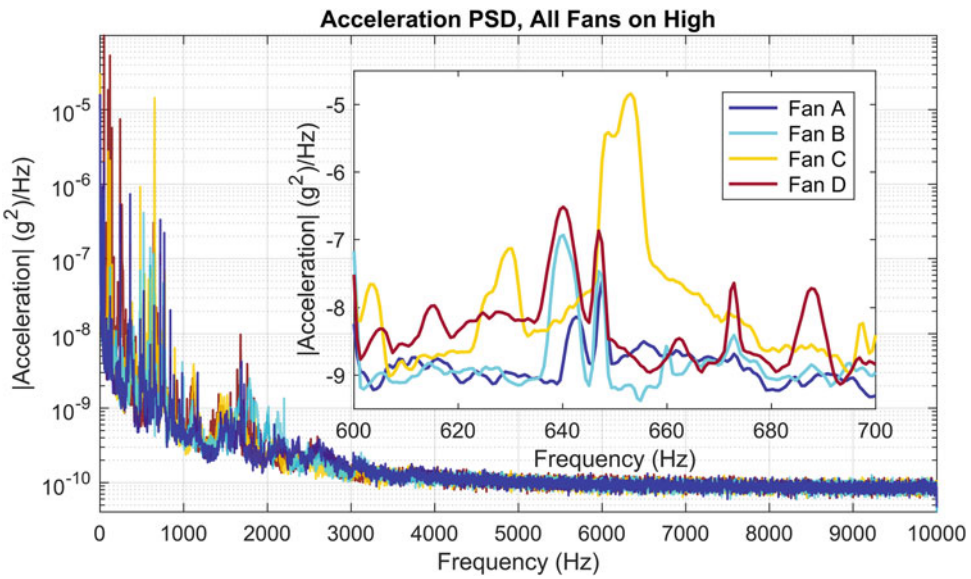

Fig. 2.6 Example fingerprint for Fan C in acceleration PSD

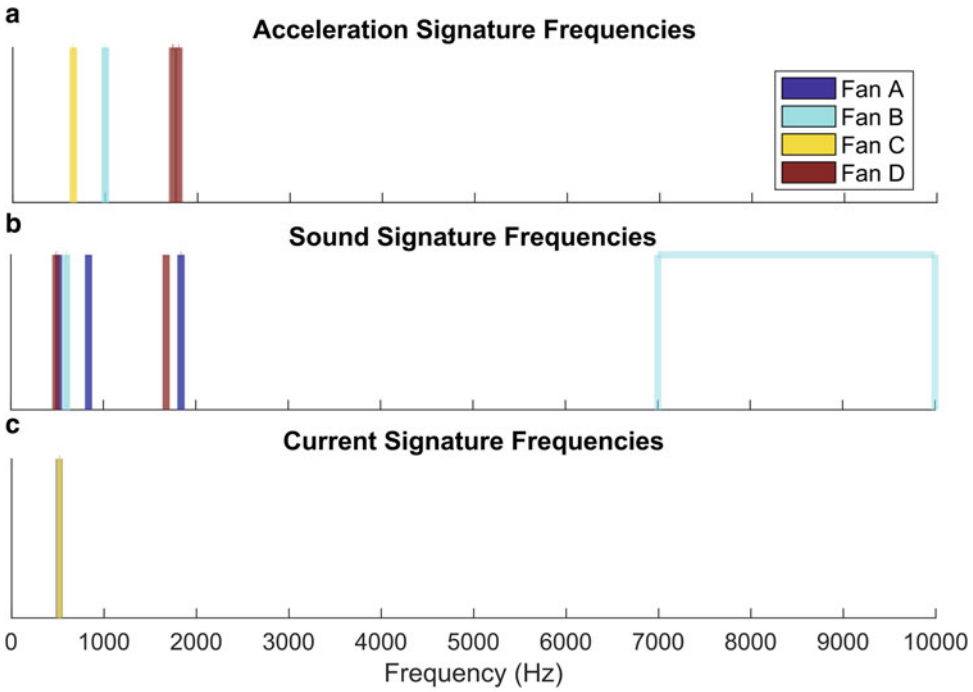

Fig. 2.7 Visual representation of the frequencies at which fingerprints of each fan were found. The large *blue* band in the sound fingerprints is due to Fan B being significantly louder at higher frequencies than the other fans

Table 2.2 Summary of fingerprint sensors and frequencies for each fan

Fan A		Fan B		Fan C		Fan D	
sensor	Freq (Hz)	sensor	Freq (Hz)	sensor	Freq (Hz)	sensor	Freq (Hz)
Mic.	839–841	Accel.	995–1005	Accel.	650–660	Mic.	1679–1680
Mic.	1837–1844	Mic.	7000–10,000	Current	516–519	Mic.	482–492
Current	513–516	Mic.	595–605			Accel.	1725–1740
Mic.	513–516					Accel.	1790–1800

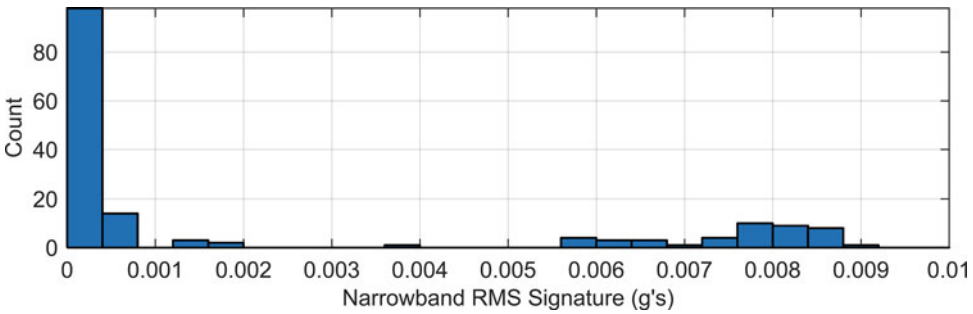

Fig. 2.8 Histogram used to set a threshold for a particular acceleration signature from Fan C

with the largest distances from the mean would be identified as running. This algorithm correctly characterized the entire system 95% of the time. Every "error" was associated with Fan D being wrongly identified as Fan A or B. Mathematically, the process is as follows:

$$N = 45 \times I \tag{2.2}$$

where N is the number of fans and I is the current measured in the system.

$$\mu = \frac{\sum_{k=1}^{K} s}{K} \tag{2.3}$$

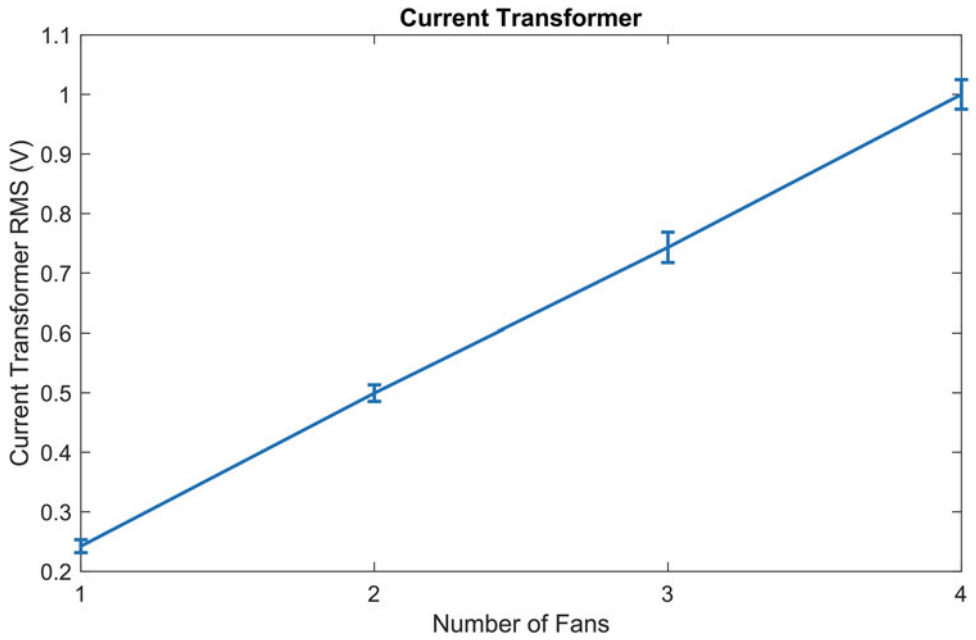

Fig. 2.9 RMS of current signal for different numbers of fans in operation

where s is a fingerprint value, K is the number of values known for a particular fingerprint (for example, the Fan B microphone fingerprint at 7–10 kHz may have 50 values measured from previous data collections), and μ is the mean of the fingerprint distribution.

$$\sigma = \sqrt{\frac{\sum_{k=1}^{K} (s-\mu)^2}{K}} \tag{2.4}$$

where σ is the mean standard deviation for the distribution of the fingerprint values.

$$d = \frac{x-\mu}{\sigma} \tag{2.5}$$

where x is the value measured for the fingerprint from the unknown system, and d is the distance of x from the mean, measured in standard deviations.

$$S_j = \sum_{m=1}^{M} d_m \tag{2.6}$$

where S_j is the sum of the distances of each of the fingerprints associated with a particular fan j, and M is the number of fingerprints associated with that fan (for example, for Fan B, $M = 3$ since Fan B has three fingerprints).

After S is calculated for each fan, the N fans with the largest values of S are chosen as the fans present in the system.

2.9 Evaluation

Of the many methods investigated in this study, the detector that computed the largest distances from the mean was the most successful for characterizing the entire system in terms of fan presence. The method of feature extraction used training data collected when each fan was operating individually, but was able to correctly identify the presence of each fan 95% of the time when multiple rans were running.

Table 2.3 Effectiveness of model with sensor omission

Sensor removed	One fan accuracy	Two fan accuracy	Three fan accuracy	Four fan accuracy	Overall accuracy
None	93%	100%	94%	100%	95%
Current	88%	100%	100%	100%	93%
Sound	78%	86%	71%	100%	82%
Accelerometer	95%	100%	94%	100%	96%

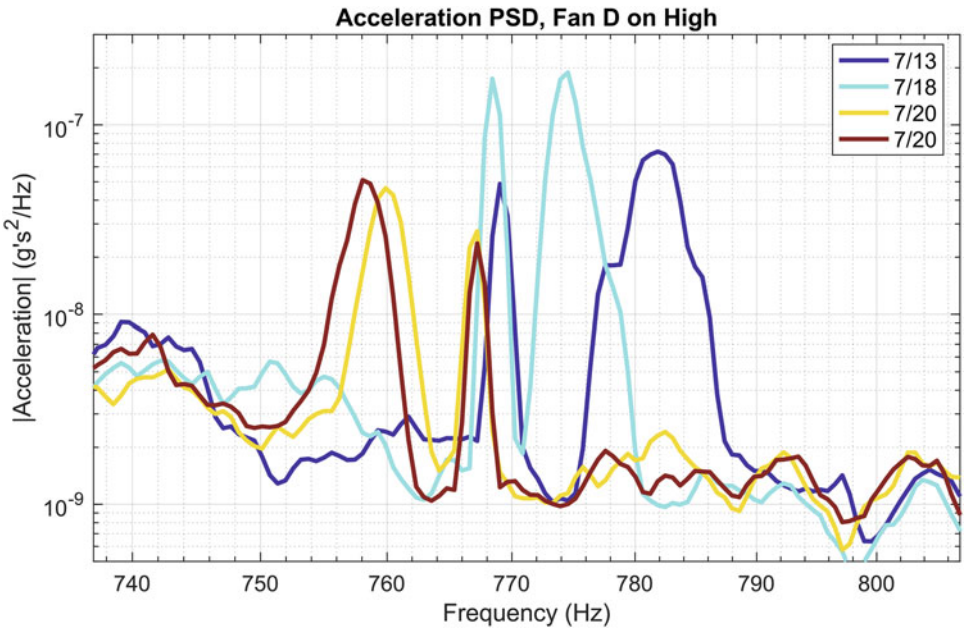

Fig. 2.10 PSD of Fan D's acceleration data from collection dates of 7/13/16, 7/18/16, and 7/20/26

The study aimed to use data from multiple sources in order to strengthen the inferences made by the condition monitoring system. In order to assess the effectiveness of the multi-source data, the third detector was applied while omitting, one at a time, each sensor that contributed to the signatures. The results are summarized in Table 2.3.

Notable is the model's increase in overall accuracy from 95 to 96% after the omission of the accelerometer data. This result was surprising, as it was assumed that an increase in fingerprints for each fan would correspond to an increase in accuracy. One possible explanation is that the signatures extracted from the acceleration PSD could have been inconsistent, in which case they may have hindered the model's ability to correctly characterize the system.

Even with sensors omitted, the model was always correct when all four fans were running. This accuracy results from the use of the current RMS (shown in Fig. 2.9) to identify the number of fans running in the system. If four fans were running, the model would select the fans with the four highest distances from the mean, which would be every fan in the array. Therefore, the model did not utilize the healthy fingerprints to identify the presence of the fans in the array when all four were operating. The model could be enhanced by identifying not only whether each fan was in operation, but also if the fan was in a healthy or unhealthy state.

During data collection, an effort was made to keep the experimental setup as consistent as possible. However, several sources of variability were still present in the data collection process. Any disturbance during data collection could be picked up by the accelerometer or microphone. Although data was collected with the lights off, the antenna data fluctuated between data runs based on the presence of other lights in surrounding rooms. The largest factor in fluctuation between data runs, however, was the baseline of the system. This variability was prevalent in the data from Fan D, which was the fan that was disassembled and reassembled the most often in order to induced artificial damage. Each time the fan was reassembled, shifts in the dominant frequencies would occur. See Fig. 2.10 for an example of Fan D's PSD over a small frequency range between different dates of data collection.

2.10 Further Research

The signatures used in the model only represented each fan in a healthy state, that is, under normal operating conditions. However, evidence exists that the RF spectra may contain signatures for fans in unhealthy states. Damage was introduced into the system by loosening screws on the motor plate and attaching a small mass to one of the fan blades. The RF PSD for Fan D, shown in Fig. 2.11, indicates a shift in peak locations based on the presence of damage. Further data from the unhealthy states is necessary in order to validate these damage signatures.

2.11 Conclusion

The condition monitoring system developed in this study utilized data from non-commensurate sensors, located remotely from the source signals, to characterize the state of a machine array. The "characterization" performed by this study's model refers to identifying the presence or absence of each fan in the array when operating at high speed. The most effective model investigated in this study was able to correctly characterize the array of fans 95% of the time, but its accuracy increased to 96% with the removal of the signatures from the acceleration data.

Several unique fingerprints were tested in a machine learning algorithm to identify the presence of each healthy fan in the array. The fingerprint of a healthy fan would disappear as the system transitioned to an unhealthy state; therefore, an absent fan signature provides a strong indication of damage. The training data used in the model was taken only while one fan was running at a time, and the features extracted from individual fan data proved to be effective in characterizing the system when more than one fan was running.

Data from multiple sources strengthened the model by providing more locations to identify each fan's fingerprint. Overall, the fans were difficult to distinguish from each other due to their nominally identical nature. Certain fans were easier to identify because they produced more peaks in the power spectra than others. The accelerometer and microphone PSDs supplied the most signatures for individual fans, while the RMS value over the entire current signal provided a consistently accurate way of indicating how many fans in the array were running. Although the accelerometer signatures actually weakened the model's ability to characterize the system, it is likely that the development of more optimal features from the acceleration data would increase the model's accuracy.

The implementation of multi-source, remote, centralized condition monitoring systems for machines in an industrial setting can reduce maintenance costs by identifying damage before failure occurs and providing ease of instrumentation,

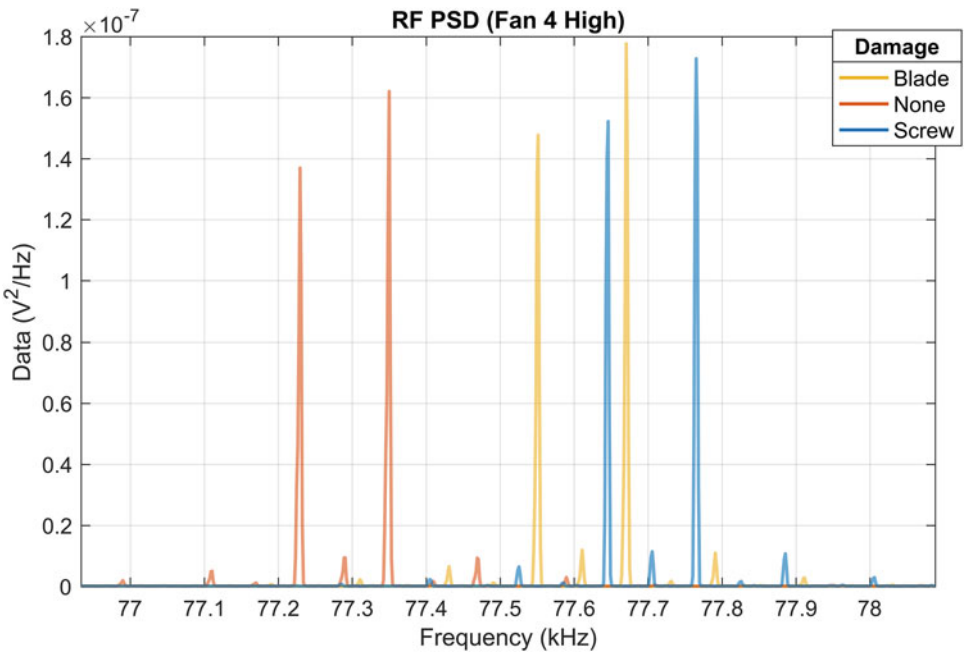

Fig. 2.11 Dominant frequencies before and after implementation of damage (loose screw, mass added to blade) in the RF PSD for Fan D

data acquisition, and retrofit. Future research should focus on collecting a greater amount of healthy system data to validate the existing features. The identification of additional features in both the healthy and unhealthy states will strengthen the model developed in this study. Signatures for each fan at medium and low speed could be identified as well, allowing the system to characterize fan speed as well as the presence of damage.

References

1. Farrar, C.R., Worden, K.: Structural Health Monitoring: A Machine Learning Perspective. John Wiley & Sons, New Jersey (2013)
2. Sohn, H., Farrar, C.R., Hemez, F.M., Shunk, D.D., Stinemates, D.W., Nadler, B.R., Czarnecki, J.J.. A review of structural health monitoring literature: 1996–2001. Los Alamos National Laboratory Report (2004)
3. Eisenmann Sr., R.C., Eisenmann Jr., R.C.: Machinery Malfunction Diagnosis and Correction: Vibration Analysis and Troubleshooting for the Process Industries. Prentice Hall, Upper Saddle River, NJ (1998)
4. Mitchell, J.S.: From vibration measurements to condition based maintenance: seventy years of continuous progress. J. Sound Vib. **41**(1), 62–75 (2007)
5. Sedding, H. and Brown, A., Review of effective diagnostic and condition monitoring methods for rotating machines. In: Proceedings of the IEEE Power and Energy Society General Meeting—Conversion and Delivery of Electrical Energy in the 21st Century, July 2008
6. Stone, G.C.: Condition monitoring and diagnostics of motor and stator windings—a review. IEEE Trans. Dielectr. Electr. Insul. **20**(6), 2073–2080 (2013)
7. Negoita, A., Scutaru, G., Ionescu, R.M.: A brief review of monitoring techniques for rotating electrical machines. Bull. Trans. Univ. Brasov. **3**(52), 277–284 (2010)
8. Nandi, S., Toliyat, H.A., Condition monitoring and fault diagnosis of electrical machines—a review. In: Proceedings of the IEEE Industry Applications Conference, vol. 1, pp. 197–204, Oct 1999
9. Lebold, M., McClintic, K., Campbell, R., Byington, C., Maynard, K., Review of vibration analysis methods for gearbox diagnostics and prognostics. In: Proceedings of the 54th Meeting of the Society for Machinery Failure Prevention Technology, pp. 623–634, May 2000
10. Tavner, P.J.: Review of condition monitoring of rotating electrical machines. IET Electr. Power Appl. **2**(4), 215–247 (2008)
11. Reichard, K.M., Van Dyke, M., Maynard, K.: Application of sensor fusion and signal classification techniques in a distributed machinery condition monitoring system. Proc. SPIE. **4051**, 329–336 (2000)
12. Kirkwood, L., Shehab, E., Baguley, P., Amorim-Melo, P., Durazo-Cardenas, I., Challenges in cost analysis of innovative maintenance of distributed high-value assets. In: Proceedings of the 3rd International Through-life Engineering Conference, pp. 148–151, October 2014
13. Hall, D.L., Llinas, J.: An introduction to multisensor data fusion. Proc. IEEE. **85**(1), 6–23 (1997)
14. Varshney, P.K. Multisensor data fusion. In: 13th International Conference on IEA/AIE, June 2000
15. Flammini, F., Marrone, S., Mazzocca, N., Vittorini, V.: Using Bayesian networks to evaluate the trustworthiness of '2 out of 3' decision fusion mechanisms in multi-sensor applications. Proc. IFAC. **48**(21), 682–687 (2015)
16. Simonson, K. M., Probabilistic Fusion of ATR Results. Sandia National Laboratories, Aug 1998
17. Kuttruff, H.: Acoustics: An Introduction. CRC Press, Boca Raton, FL (2011)
18. Gustrau, F.: RF and Microwave Engineering. John Wiley & Sons, New Jersey (2012)
19. Van Hulle, M.M., Clustering approach to square and non-square blind source separation. In: Proceedings of the 1999 IEEE Signal Processing Society Workshop, pp. 315–323, Aug 1999
20. Yang, Y., Nagarajaiah, S.: Output-only modal identification with limited sensors using sparse component analysis. J. Sound Vib. **332**, 4741–4765 (2013)
21. Gribonval, R., Lesage, S., A survey of sparse component analysis for blind source separation: principles, perspectives, and new challenges. In: ESANN Proceedings—14th European Symposium on Artificial Neural Networks, Apr 2006
22. Hastie, T., Tibshirani, R., Wainwright, M.: Statistical Learning with Sparsity: The Lasso and Generalizations. CRC Press, Boca Raton, FL (2015)
23. Bofill, P., Zibulevsky, M., Underdetermined blind source separation using sparse representations. In: Signal Processing 81, pp. 2353–2362, June 2001
24. Zibulevsky, M., Pearlmutter, B.: Blind source separation by sparse decomposition in a signal dictionary. Neural Comput. **13**, 863–882 (2001)

Chapter 3
Wavelet Transform-Based Damage Detection in Reinforced Concrete Using an Air-Coupled Impact-Echo Method

Tyler Epp and Young-Jin Cha

Abstract A large amount of infrastructure in North America is in need of repair or replacement. The cost of these improvements is a huge obstacle for governments and the issue will be exacerbated in the coming years as current infrastructure, including bridges, get closer to the end of their design life (The Age of Public Infrastructure in Canada http://www.statcan.gc.ca/pub/11-621-m/11-621-m2006035-eng.htm, 2009; 2013 Report Card for American Infrastructure http://www.infrastructurereportcard.org/bridges/, 2013). The use of prescribed maintenance is no longer efficient or cost effective enough to continue to be used as a means of upkeep for bridges. Indeed, new methods are being developed in order to gain a deeper understanding of the state of bridges so that more precise maintenance can be carried out.

Keywords Energy impact factor • Wavelet transform • FFT • SHM • NDT • Reinforced concrete

A large amount of infrastructure in North America is in need of repair or replacement. The cost of these improvements is a huge obstacle for governments and the issue will be exacerbated in the coming years as current infrastructure, including bridges, get closer to the end of their design life [1, 2]. The use of prescribed maintenance is no longer efficient or cost effective enough to continue to be used as a means of upkeep for bridges. Indeed, new methods are being developed in order to gain a deeper understanding of the state of bridges so that more precise maintenance can be carried out.

Within the field of structural health monitoring (SHM), non-destructive testing (NDT) of bridges has expanded immensely in the past decades to include applications such as vision-based damage detection [3–5], acoustic emission sensors [6–9], fibre-optic sensors [10], ground penetrating radar (GPR) [11, 12], acoustic-lasers [12], and impact-echo methods [13–23].

Impact-echo methods using air-coupled sensors have shown the ability to detect delaminations and voids in large concrete structures, including bridge decks [13–23]. The ability of the method to detect such damages generally relies on spectral information about acoustic signals [14, 16, 20–23]. The structure is excited in a point-by-point manner in order to receive signals using microphones. The signals can further be used to develop images of the internal condition of the structure by applying post-processing techniques to determine spectral information about the structure. A limitation of the impact-echo method using air coupled sensors is the time-consuming nature of the data acquisition. This work sets out to improve the accuracy of the method over increased spacing of the impact site and sensors used for signal collection.

Impact-echo signals are generally processed for spectral information using the Fast Fourier Transform (FFT) [14, 16, 20–23]. The FFT, however, does not retain temporal information about the signal and instead sums up spectral components, giving relative magnitudes of the frequencies contained within the signal. Wavelet transforms, on the other hand, are able to retain temporal information while identifying spectral information about the signal. The scale the wavelet is used at determines the frequencies the wavelet is most sensitive to. Several wavelets were used in this work at a large range of scales in order to get an extensive look at spectral information across the time domain of the collected signals.

(a) FFT cutoff of 40 for MIC 1 and 2 [23]
(b) Mexican Hat wavelet transform cutoff of 0.5 MIC 1 and 2 [23]

The images in Fig. 3.1 were created using data points on a large concrete beam (4000 × 360 × 300) that contains in-situ void and delamination damages. Cutoff values are defined for each the FFT and wavelet transform in order to determine intact and damaged points in the specimen. The cutoff values used with the FFT are based on the magnitude of the spectral

T. Epp
Department of Civil Engineering, University of Manitoba, 96 Dafoe Rd., Winnipeg, MB, Canada

Y.-J. Cha (✉)
Department of Civil Engineering, University of Manitoba, 15 Gillson St., Winnipeg, MB, Canada
e-mail: young.cha@umanitoba.ca

C. Niezrecki (ed.), *Structural Health Monitoring & Damage Detection, Volume 7*, Conference Proceedings of the Society for Experimental Mechanics Series, DOI 10.1007/978-3-319-54109-9_3

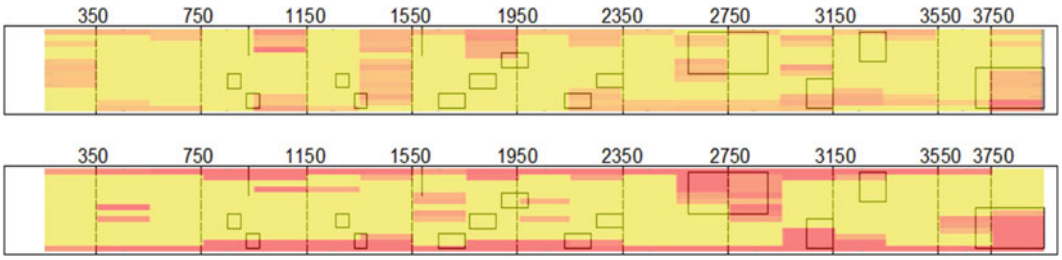

Fig. 3.1 Comparison of images created with FFT (*top*) and Mexican Hat wavelet (*bottom*) using two microphones spaced 200 mm from the impact location

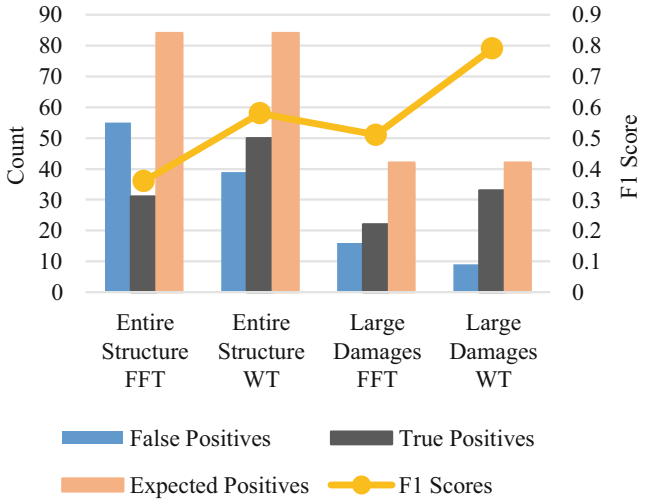

Fig. 3.2 Performance of FFT compared to Mexican Hat wavelet transform for test carried out with MIC 1 and 2200 mm from the impact location [23]

information. The cutoff values used with the wavelet transforms are developed using the energy impact factor developed from comparison of the low frequency band and high frequency damage sensitive band.

Figure 3.2 shows that the wavelet transform performed better over the entirety of the specimen, as well as over the area of well-identified large damages on the right side of the structure, measured in terms of the number of false damage sites reported, true positives identified, and F1 score.

The two post-processing methods were compared for accuracy of in-situ damage detection on a large concrete beam. The results show that wavelet transforms are more accurate compared to the results found using the FFT when the microphones are moved away from the point of excitation on the structure. This work could have applications in array-based sensing that would further improve the efficiency of the impact-echo method using air-coupled sensors.

References

1. The Age of Public Infrastructure in Canada. Retrieved April 26, 2016, from http://www.statcan.gc.ca/pub/11-621-m/11-621-m2006035-eng.htm (2009)
2. 2013 Report Card for American Infrastructure. Retrieved April 26, 2016, from http://www.infrastructurereportcard.org/bridges/ (2013)
3. Cha, Y.J., You, K.S., Choi, W.: Vision-based detection of loosened bolts using the Hough transform and support vector machines. Autom. Constr. **71**, 181–188 (2016)
4. Chen, J., Wadhwa, N., Cha, Y.J., Durand, F., Freeman, F., Büyüköztürk, O.: Modal identification of simple structures with high-speed video using motion magnification. J. Sound Vib. **345**, 58–71 (2015)
5. Cha, Y.J.; Chen, J.; Büyüköztürk, O. Motion magnification based damage detection using high speed video. In: Proceedings of the 10th International Workshop on Structural Health Monitoring (IWSHM), Stanford, CA, USA, 1–3 September 2015
6. Mirmiran, A., Philip, S.: Comparison of acoustic emission activity in steel-reinforced and FRP-reinforced concrete beams. Constr. Build. Mater. **14**, 299–310 (2000)
7. Oliveira, R., Marques, A.: Health monitoring of FRP using acoustic emission and artificial neural networks. Comput. Struct. 367–373 (2007)

8. Xidong, L., Ju, F., & Ling, C.. Research on the brittle fracture of FRP rods and its acoustic emission detection. In: 2000 IEEE Power Engineering Society Winter Meeting, Conference Proceedings (Cat. No.00CH37077) (2000)
9. Ghiassi, B., Verstrynge, E., Lourenço, P.B., Oliveira, D.V.: Characterization of debonding in FRP-strengthened masonry using the acoustic emission technique. Eng. Struct. **66**, 24–34 (2014)
10. Henault, J., Quiertant, M., Delepine-Lesoille, S., Salin, J., Moreau, G., Taillade, F., Benzarti, K.: Quantitative strain measurement and crack detection in RC structures using a truly distributed fiber optic sensing system. Constr. Build. Mater. **37**, 916–923 (2012)
11. Hugenschmidt, J., Mastrangelo, R.: GPR inspection of concrete bridges. Cem. Concr. Compos. **28**(4), 384–392 (2006)
12. Qiu, Q., Lau, D.: The sensitivity of acoustic-laser technique for detecting the defects in cfrp-bonded concrete systems. J. Nondestruct. Eval. **35**(2), 1–10 (2016)
13. Ham, S., Popovics, J.: Application of contactless ultrasound toward automated inspection of concrete structures. Autom. Constr. **58**, 155–164 (2015)
14. Oh, T., Popovics, J.: Application of impact resonance C-scan stack images to evaluate bridge deck conditions. J. Infrastruct. Syst. **21**(1), 21–26 (2014)
15. Beniwal, S., Ganguli, A.: Localized condition monitoring around rebars using focused ultrasonic field and SAFT. Res. Nondestruct. Eval. **27**(1), 48–67 (2015)
16. Carino, N.J.: The impact-echo Method: an overview. Structures 1–18 (2001)
17. Groschup, R., Grosse, C.: MEMS microphone array sensor for air-coupled impact-echo. Sensors. **15**(7), 14932–14945 (2015)
18. Ham, S., Popovics, J.: Application of micro-electro-mechanical sensors contactless NDT of concrete structures. Sensors. **15**(4), 9078–9096 (2015)
19. Hoegh, K., Khazanovich, L.: Extended synthetic aperture focusing technique for ultrasonic imaging of concrete. NDT E Int. **74**, 33–42 (2015)
20. Kundu, T., Ehsani, M., Maslov, K., Guo, D.: C-scan and L-scan generated images of the concrete/GFRP composite interface. NDT E Int. **32**(2), 61–69 (1999)
21. Zhu, J. Non-contact NDT of concrete structures using air-coupled sensors. Unpublished doctoral dissertation, University of Illinois at Urbana-Champaign (2005)
22. Zhang, Y., Wei, X., Tsai, Y., Zhu, J., Fetrat, F.A., Gucunski, N.: Multisensor data fusion for impact-echo testing of concrete structures. Smart Mater. Struct. **21**(7), 075021 (2012)
23. Epp, T., Cha, Y.J.: Air-coupled impact-echo damage detection in reinforced concrete using wavelet transforms. Smart Mater. Struct. **26**(2), 025018 (2016)

Chapter 4
Damage Detection Based on Strain Transmissibility for Beam Structure by Using Distributed Fiber Optics

Liangliang Cheng, Giorgio Busca, Paolo Roberto, Marcello Vanali, and Alfredo Cigada

Abstract Structural damage identification is a coral and challenging research topic. Research mainly focuses on identification and detection of linear damage in structures by using modal parameters such as change of natural frequency, frequency response function, mode shape, etc. Transmissibility is conventionally defined as the spectra ratio of two measurement points, which has been utilized for damage identification as a powerful damage indicator. In this paper, strain transmissibility, defined as ratio of strain response spectra, is proposed as a new damage indicator. In order to achieve more precise sensing information, distributed fiber optics has been applied to damage detection on a beam structure, which adds new capability of sensing with its combination of high spatial density sensing and dynamic acquisition over a single optical fiber sensor. A numerical simulation has been conducted to investigate the feasibility of strain transmissibility for damage detection which has revealed a better performance compared to traditional transmissibility. The applicability of the proposed method has been confirmed by applying distributed fiber optics on a clamped-clamped beam. Both simulation and experiment validate the effectiveness of damage detection approach based on strain transmissibility by using distributed fiber optics.

Keywords Strain transmissibility • Distributed fiber optics • Optical frequency domain reflectometer • Dynamic measurement • Damage detection

4.1 Introduction

Most of civil, mechanical and aerospace structures are vulnerable to damage due to human factors, natural disasters, prolonged fatigue or corrosion. Therefore, in the last 20 years structural health monitoring has been extremely attractive to supervise the health status of structures. Damage detection techniques are based on a wide variety of physical principles [1], mainly focused on vibrations and modal parameters. A review work of damage detection methods based on modal parameters was carried out by Doebling et al. [2–4].

Damage detection performed on modal parameters (natural frequency, mode shape and damping) has many advantages compared to other methods mainly due to the fact that modal parameters merely depend on the characteristics of structures themselves [5]. Since structural vibration characteristics depend on structural physical parameters, a change of the physical parameters due to a damage, for instance a stiffness reduction, will inevitably cause a change of the structural dynamic response.

Modal parameters identification during a continuous monitoring is usually performed by using only output measurement data and operational modal analysis. However, this could be a troublesome point in some cases, because the a priori hypothesis about independency of the modal parameters on the excitation level and the requirement of a flat spectrum of the driving force is not always respected. Among the operational feature that can be estimated from the structure response, transmissibility function drew the attention of many researchers, because it does not require any prior knowledge of the exciting force and no modal identification is needed. Transmissibility is conventionally defined as the ratio of the spectra of two different outputs of the system and it was proposed as damage feature firstly in [6]. The damage feature is usually the difference among the transmissibility functions of the health structure and an unknown scenario. Maia et al. [7] carried out a rather comprehensive analysis about transmissibility theory and they proposed the Detection and Relative Damage Quantification Indicator (DRQ) as a reliable damage detection indicator [8].

L. Cheng • G. Busca • P. Roberto • A. Cigada (✉)
Department of Mechanical Engineering, Politecnico di Milano, Via la Masa 1, 20156, Milan, Italy
e-mail: alfredo.cigada@polimi.it

M. Vanali
Department of Engineering and Architecture, Universita di Parma, Parco Area delle Science, 181/A-43124 Parma, Italy

C. Niezrecki (ed.), *Structural Health Monitoring & Damage Detection, Volume 7*, Conference Proceedings of the Society for Experimental Mechanics Series, DOI 10.1007/978-3-319-54109-9_4

In the papers [9–11], the authors have worked on the extension of transmissibility concept to multiple degree freedom. It is worth mentioning that Lang et al. proposed also to extend the transmissibility to nonlinear damage detection based on NOFRF (non-linear output frequency response functions) in [12, 13]. DRQ is calculated through evaluating integral difference over a fixed frequency band between intact transmissibility and damaged transmissibility. However, the outcomes of damage identification are extremely influenced by the choice of this frequency band as described in [14–16]. Recently, this issue was discussed by Patrick Guillaume's papers [17, 18] who proved that the limit value of the transmissibility function to the poles of the system converges to the ratio of the mode shapes of the two measurement points. They also pointed out that by using only a small frequency band around the resonance frequencies of structures, the outcomes of damage identification are more reliable and independent from the force location. A detailed review of transmissibility function can be found in [19].

The accuracy of damage localisation, based on the aforementioned transmissibility function, relies on the number of sensors as well. When dynamic test is performed on large structures such as bridges, tunnels and buildings, conventional sensors are extremely difficult to cover the entire target. Usually the number of sensors needed to do this it is too big and then the idea is impracticable mainly for economic reasons. Fortunately, distributed fiber optics techniques have kept developing rather maturely and they have been applied into various domains [20–22]. Distributed fiber optic sensors can measure continuously strain and temperature along the structure layout and in some cases they can also be embedded into concrete for checking the internal health status. Generally speaking, distributed fiber optic sensors can be classified into three categories based on Rayleigh, Brillouin and Raman scattering techniques [20] which can be chosen according to specific requirements.

This paper will report the developing of strain transmissibility function and its corresponding damage indicator by using distributed fiber optic sensor. A short review of damage detection based on traditional transmissibility function algorithm is described in Sect. 2. In Sect. 3, strain transmissibility has been proposed. Simulation and experiment have been discussed in Sects. 4 and 5 respectively. The last section gives the conclusion of this paper. It will be shown that strain transmissibility function is more sensitive to damage than traditional transmissibility functions based on acceleration and displacement data. Simulations and experiments are carried out and have proved the feasibility of damage detection by using strain transmissibility function.

4.2 Transmissibility Functions Algorithm

Transmissibility function is traditionally defined as the ratio of two different output spectra. As for a MDOF system, let $F_k(s)$ be driving force at DOF k, then the transmissibility function $T_{ij(k)}(s)$ can be calculated as

$$T_{ij(k)}(s) = \frac{X_{ik}(s)}{X_{jk}(s)} = \frac{H_{ik}(s)F_k(s)}{H_{jk}(s)F_k(s)} \tag{4.1}$$

where $X_{ik}(s)$ and $X_{jk}(s)$ are the system outputs at DOF i and DOF j respectively; H_{ik} and H_{jk} are the frequency response functions at DOF i and DOF j respectively.

Similarly, transmissibility functions can also be defined in the same way between the same pair DOF i and DOF j when there is damage in the structure:

$$T^D_{ij(k)}(s) = \frac{X^D_{ik}(s)}{X^D_{jk}(s)} = \frac{H^D_{ik}(s)F_k(s)}{H^D_{jk}(s)F_k(s)} \tag{4.2}$$

where superscript D stands for the damaged status of the structure.

Johnson [21] proposed the following damage indicator based on transmissibility function:

$$DI_{ij(k)} = \left| \sum_{\omega} \left(\frac{TP^D_{ij(k)}(\omega) - TP_{ij(k)}(\omega)}{TP_{ij(k)}(\omega)} \right) \right| \tag{4.3}$$

where $TP_{ij(k)}(\omega) = |\log(T_{ij(k)}(\omega))|$.

Additionally, literature also proposes a damage indicator based on occurrences that seems to provide more reliable and robust results according to the authors [18]. It can be briefly explained that an occurrence is counted for each frequency step at the location where the difference between intact and damaged transmissibility is maximum. Hence, the result of occurrence relies on the frequency band that you choose. The corresponding equation is

$$O_{ij(k)}(\omega) = Count\left(\max_{\omega} \left| TP^D_{ij(k)}(\omega) - TP_{ij(k)}(\omega) \right| \right) \tag{4.4}$$

From Eq. (4.3), it is shown that damage element could correspond to the maximum value of damage indicator integrated over a range of frequency band. The paper also demonstrates that the integration of frequency band could be applied to a small frequency band around the resonance frequencies of the structure under different loading conditions.

The limit value of the transmissibility function Eq. (4.1), when variable s (the generic pole) approaches the system's poles, depends only on the mode shapes [7]:

$$\lim_{s\to\lambda_m} T_{ij(k)}(s) = \frac{\phi_{im}}{\phi_{jm}} \tag{4.5}$$

where ϕ_{im} and ϕ_{jm} are the scalar mode-shape values.

It is obvious to observe that the limit value of transmissibility function is independent from the location and nature of the force. The variable k here defines the specific loading position. Therefore, the following equation is established:

$$\lim_{s\to\lambda_m} T_{ij(k)}(s) = \lim_{s\to\lambda_m} T_{ij(l)}(s) \tag{4.6}$$

Damage indicator can be calculated by using the difference between intact and damage transmissibility under integrating a small range around resonance frequencies independently from the forcing location [18].

4.3 Strain Transmissibility Function

Usually, traditional transmissibility function (TTF) is calculated by acquiring acceleration, velocity or displacement measurement data. In this paper strain data are considered as base for a new transmissibility function, named Strain Transmissibility Function (STF). The aim of this work is to prove that STF is more sensitive to damage compared to TTF, based on the research achievement of TM Whalen, who has proved that higher order mode shape derivatives (e.g., modal curvature, third derivatives, and fourth derivatives) show better performance in terms of damage than the mode shape for beam-like structures [23].

The strain frequency response function between the loading point k and measurement point i can be written as:

$$H_{ik}^{\varepsilon}(\omega) = \frac{X_i^{\varepsilon}(\omega)}{F_k(\omega)} = \sum_{r=1}^{N} \frac{\delta_{ir}\varphi_{kr}}{M_r\left(\omega_r^2 - \omega^2 + 2j\xi_r\omega_r\omega\right)} \tag{4.7}$$

where δ_{ir} and φ_{kr} are the rth order strain mode shape and displacement mode shape respectively while ω_r is the resonance frequency. Variable k and i represent loading point and measurement output point respectively. Then the strain transmissibility function (STF) between two strain frequency response functions becomes:

$$T_{ik}^{\varepsilon}(\omega) = \frac{H_{ik}^{\varepsilon}(\omega)}{H_{jk}^{\varepsilon}(\omega)} = \frac{\sum_{r=1}^{N} \frac{\delta_{ir}\varphi_{kr}}{M_r\left(\omega_r^2 - \omega^2 + 2j\xi_r\omega_r\omega\right)}}{\sum_{r=1}^{N} \frac{\delta_{jr}\varphi_{kr}}{M_r\left(\omega_r^2 - \omega^2 + 2j\xi_r\omega_r\omega\right)}} \tag{4.8}$$

when the variable ω approaches to the resonance frequencies ω_r, the limit value can be obtained according to STF definition Eq. (4.8).

$$\begin{aligned}
\lim_{\omega\to\omega_r} T_{ik}^{\varepsilon}(\omega) &= \lim_{\omega\to\omega_r} \frac{\sum_{r=1}^{N} \frac{\delta_{ir}\varphi_{kr}}{M_r\left(\omega_r^2 - \omega^2 + 2j\xi_r\omega_r\omega\right)}}{\sum_{r=1}^{N} \frac{\delta_{jr}\varphi_{kr}}{M_r\left(\omega_r^2 - \omega^2 + 2j\xi_r\omega_r\omega\right)}} \\
&= \lim_{\omega\to\omega_r} \left. \frac{\frac{\delta_{ir}\varphi_{kr}}{M_r\left(\omega_r^2 - \omega^2 + 2j\xi_r\omega_r\omega\right)}}{\frac{\delta_{jr}\varphi_{kr}}{M_r\left(\omega_r^2 - \omega^2 + 2j\xi_r\omega_r\omega\right)}} \right|_r \\
&= \frac{\delta_{ir}}{\delta_{jr}}
\end{aligned} \tag{4.9}$$

It is known that FRFs can be decomposed into SDOF in modal space. When ω approaches to resonance frequencies ω_r, the corresponding mode will dominate the whole FRF. Similar to Eq. (4.5), Eq. (4.9) demonstrates the limit value of STF in system poles is strain mode shape ratio.

Besides, it is known that the relationship between strain and bending moment according to beam's elastic theory:

$$\varepsilon = \frac{M}{EI} \cdot h_{\max} \tag{4.10}$$

where M is the section moment, EI is bending stiffness, h_{max} is the distance from the measurement point to the neutral axis.

However, bending curvature has the following relationship:

$$C = \frac{1}{\rho} = \frac{M}{EI} = \frac{d^2y}{dx^2} \tag{4.11}$$

where C is the curvature, $\rho$is the radius of curvature, y is the displacement normal to the neutral beam axis.

Therefore, the relationship between strain and displacement can be shown as:

$$\varepsilon = \frac{d^2y}{dx^2} \cdot h_{\max} \tag{4.12}$$

The dynamic displacement of beam structure at any position x and at any time t can be redefined as the product of space function and time function by applying separation variable method:

$$y(x,t) = \sum_{i=1}^{N} \phi_i(x)\eta_i(t) \tag{4.13}$$

where ϕ and η are mode shape and modal coordinate respectively.

Therefore, substitute Eq. (4.13) into (4.12), strain can be rewritten as:

$$\begin{aligned} \varepsilon(x,t) = \frac{d^2y(x,t)}{dx^2} \cdot h_{\max} &= h_{\max} \cdot \sum\nolimits_{i=1}^{N} \phi_i''(x)\eta_i(t) \\ &= h_{\max} \cdot \sum\nolimits_{i=1}^{N} \delta_i(x)\eta_i(t) \end{aligned} \tag{4.14}$$

where δ is strain mode shape.

According to Eq. (4.12), strain is equal to the product between the second derivative of displacement and a constant which is the distance from the measurement point to neutral axis. By combing this final statement with the conclusion proposed by TM Whalen, that second mode shape derivatives are better damage indicator compared to the mode shape in terms of beam-like structures [23], it is possible to declare that strain mode shape is more sensitive than displacement mode shape to damage. Therefore, the assumption that STF in correspondence of system's poles is more sensitive to damage than traditional TTF can be established.

4.4 Simulation Validation

In order to validate the effectiveness of the proposed assumption, harmonic response analysis has been performed on a simulated beam structure. Both displacement FRFs and strain FRFs have been extracted and used to calculate TTF and STF.

4.4.1 Simulation Model

A clamped- clamped steel beam structure has been simulated by means of the commercial software ANSYS©. The dimensions are 1.5 m × 0.04 m × 0.015 m. The beam is meshed with 25 beam elements and 26 nodes. Damage is simulated by adding a point mass (0.23 kg, approximately 3% of the total mass, black block shown in Fig. 4.1) on element 19, which

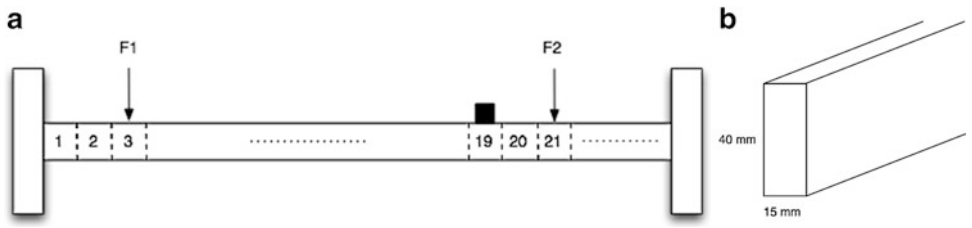

Fig. 4.1 The whole beam frame of FEM model and beam cross section

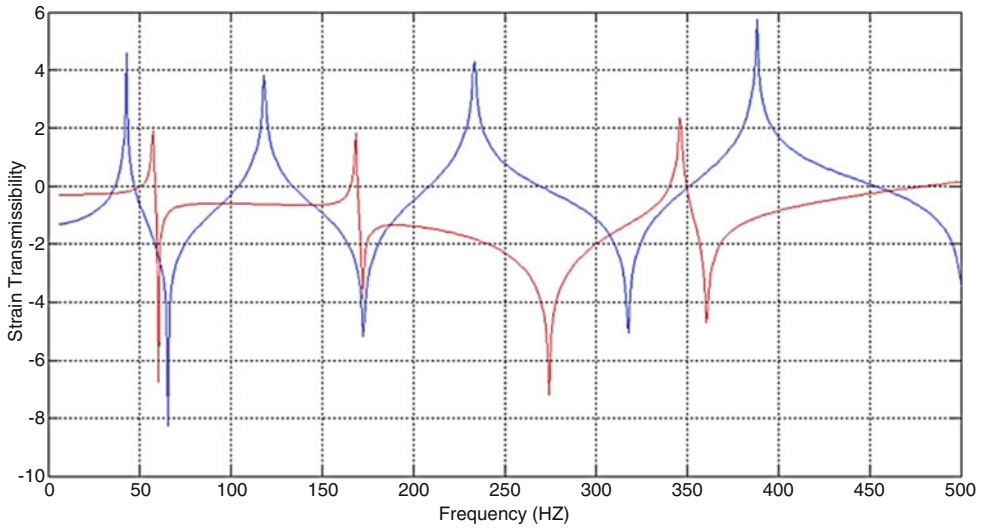

Fig. 4.2 10th measurement point STFs of intact beam for two different loading points

could be considered as linear damage that only changes the element mass between node 19 and node 20. Dynamic analysis is conducted for both intact and damaged beam, displacement responses and strain responses of all nodes have been acquired for both beams under two different scenarios. F1 and F2 are two impulse input forces on different node positions (node 3 and node 21 respectively) based on the fact that the intersections of two transmissibility functions on one specific measurement point under different loading situation corresponds to the natural frequencies of the system [18]. If there is damage, the intersections of those transmissibility functions are not coincidence with system's natural frequencies anymore and the damage indexes should reveal this fact.

4.4.2 Simulation Results

F1 and F2 have been imposed on the intact beam as shown in Fig. 4.1. According to Eq. (4.6), it is well known that the intersection of strain transmissibility functions under two different loading positions should be in accordance with systems' poles. Figure 4.2 shows the STFs acquired from 10th beam node of the intact beam under the loadings F1(3th beam node) and F2 (21th beam node) respectively.

In order to locate damage properly, TTFs and STFs are estimated on pairs of consecutive measurement points to calculate both intact and damaged beam structures. Applying Eqs. (4.1), (4.2), and (4.3), damage features could be obtained for TTFs and STFs. In this case, a small frequency band around the first resonance frequency of the intact beam (35 Hz) is selected to calculate the damage indicators by computing the difference between intact and damaged beam structure. The frequency band is fixed between 34–36 Hz around the first mode. Figures 4.3 and 4.4 show the damage indicator DI by using TTFs and STFs respectively.

The red bars point out the damage location, apparently both damage indicators are able to figure out the correct damage location 19th element. One more interesting thing needs to be noticed, damage indicator calculated by STFs seems more explicit compared to the one from TTFs. Basically, the maximum damage feature could correspond to the true damage

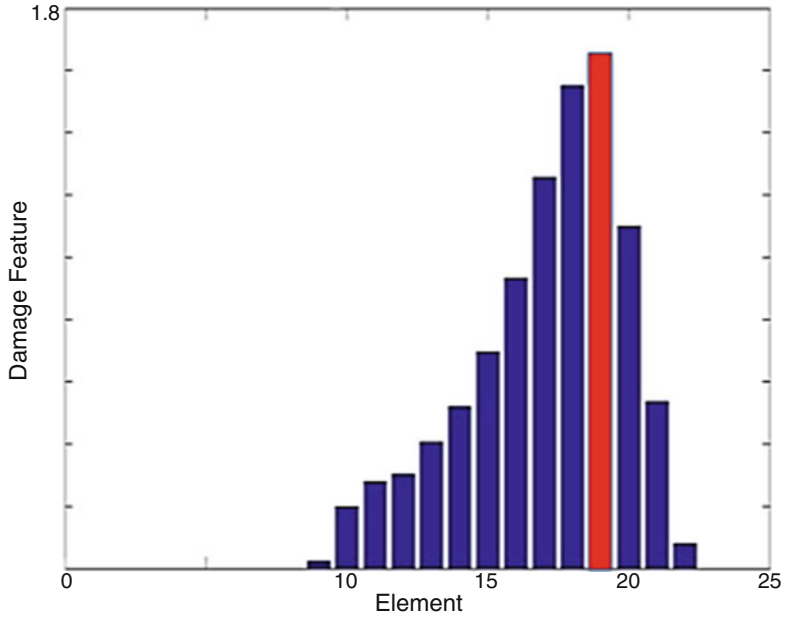

Fig. 4.3 Damage feature by using TTFs

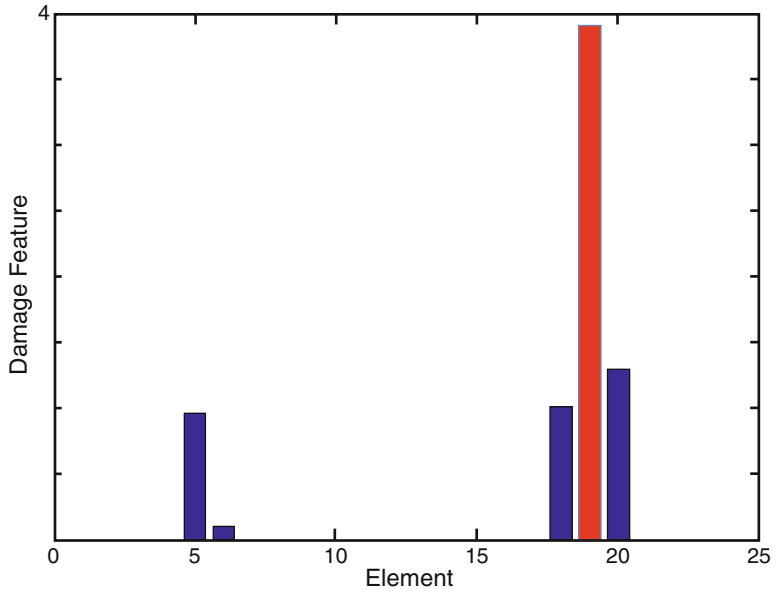

Fig. 4.4 Damage feature by using STFs

location which localizes at 19th element shown in Fig. 4.3, however, the difference between 18th and 19th beam element is quite small in terms of damage indicator, which might make the result ambiguous. In contrast, damage indicator by using STFs in Fig. 4.4 shows a very clear result since there is only one high value at the19th beam element obviously.

The simulated data were also processed by the damage feature based on occurrences to test its performance. Figures 4.5 and 4.6 show the results from occurrences and analogous conclusions to the previous case can be drawn. Both the measurements (displacement and strain) indicate precisely the damage location. Moreover, occurrences in Fig. 4.6 demonstrates that STFs are more sensitive than TTFs in terms of damage detection since only one damaged bar is shown.

Apparently, occurrence is able to locate damage in a more robust and effective way, though damage indicator by using difference between intact and damaged TFs is able to work properly. Besides, no matter which the damage feature is used, it has shown that STFs have better performance on damage identification with respect to TTFs.

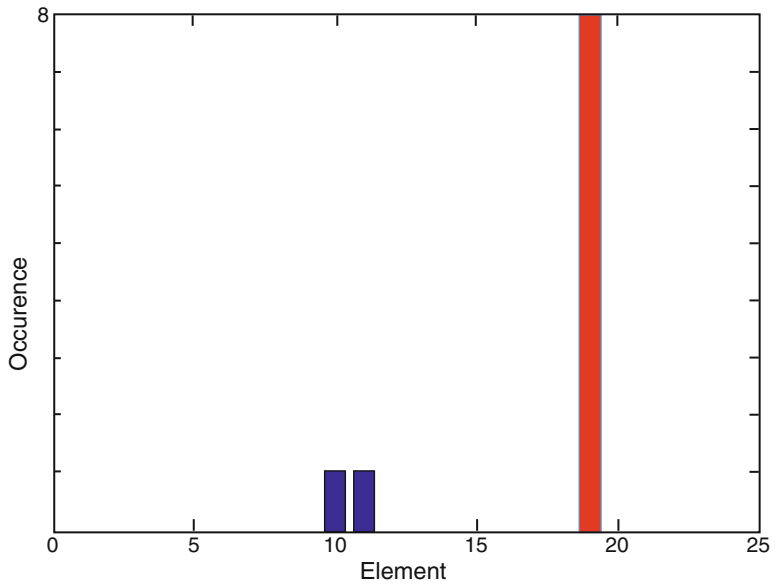

Fig. 4.5 Occurrence by using TTFs

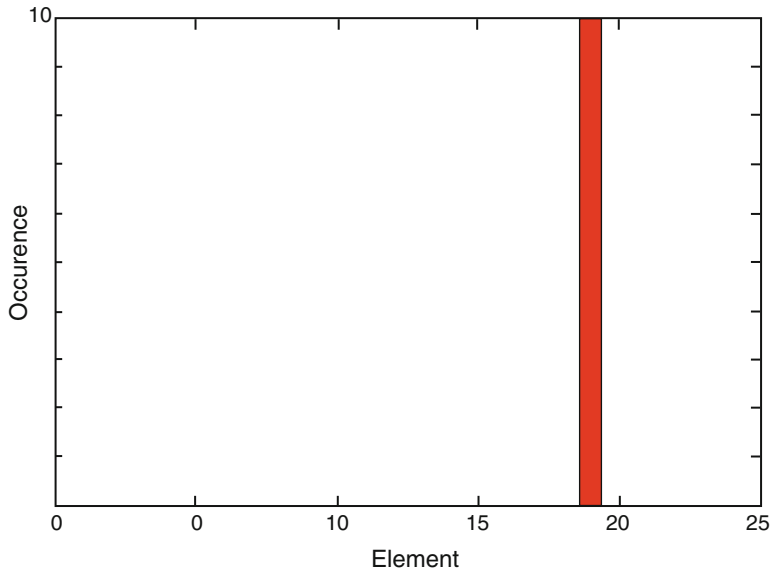

Fig. 4.6 Occurrence by using STFs

4.5 Experiment Validation

Since damage localisation depends on the number of sensing points, distributed fiber optics sensor has been applied for strain measurement because it is capable to provide numerous sensing points. Therefore, LUNA ODiSI-B optical distributed sensor interrogator has been adopted; which uses optical frequency domain reflectometry technique to measure strain along one single fiber.

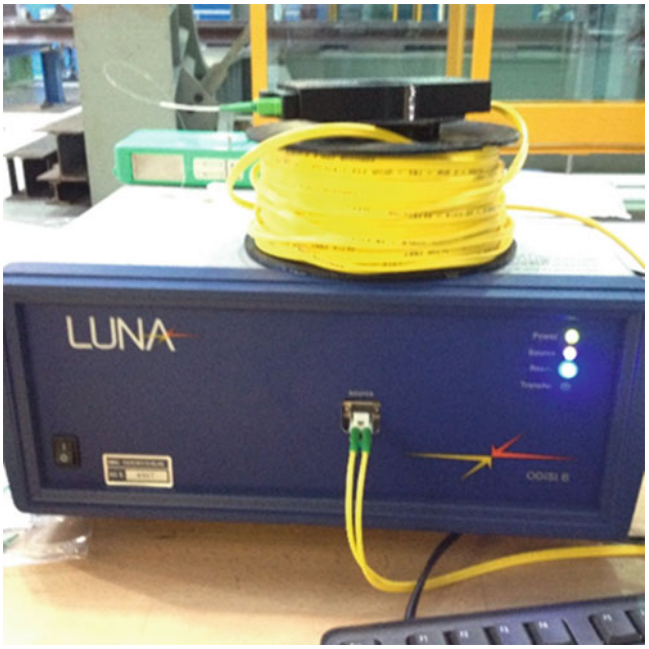

Fig. 4.7 Model ODiSI-B

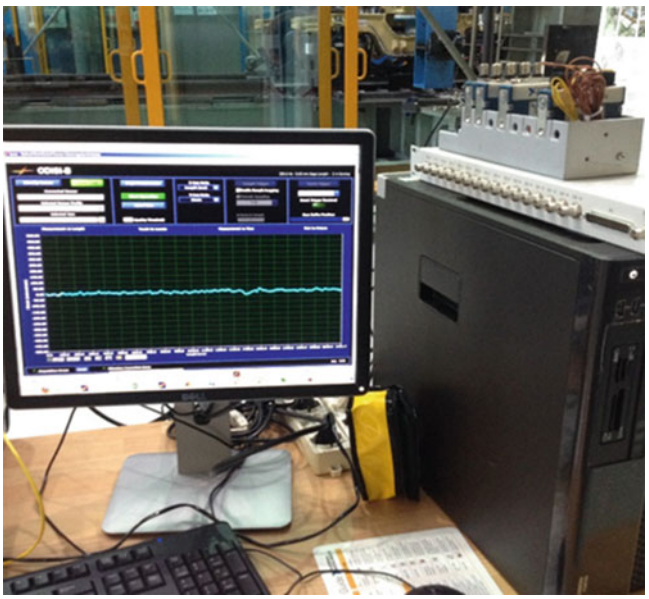

Fig. 4.8 Interface of DAQ system

4.5.1 Brief Introduction of ODiSI-B

Optical distributed sensor interrogator (Model ODiSI-B in Fig. 4.7) provides a paramount industrial solution for applications in many fields with outstanding spatial resolution. LUNA's ODiSI B is capable to cover more than 10 m of dynamic measurement range with a high density of measurement points. ODiSI B can simultaneously demodulate thousands sensing points over a single optical fiber at a frequency of 100 Hz. 10 m maximum sensing distance and spatial resolution of 2.56 mm make ODiSI B an extremely important tool as for strain and temperature sensing applications. Figure 4.8 shows the operational interface of data acquisition software for ODiSI-B.

4.5.2 Experimental Setup

A clamped-clamped steel beam has been utilized with dimension 1.5 m × 0.04 m × 0.015 m. In order to attach the fiber optics firmly, the steel beam surfaces were polished and then a specific glue was used to attach the fiber optics as shown in Fig. 4.9.

Figure 4.10 shows the whole frame of beam structure. Magnets are attached to the surface of the beam in order to increase the weight of beam itself, which is able to simulate linear damage situation due to the change of dynamic characteristic (Fig. 4.11). The weight of the magnets is about 0.23 kg over 7.1 kg of the beam.

Fig. 4.9 Beam attached with fiber optic

Fig. 4.10 Beam experiment setup

Fig. 4.11 Magnets added into beam

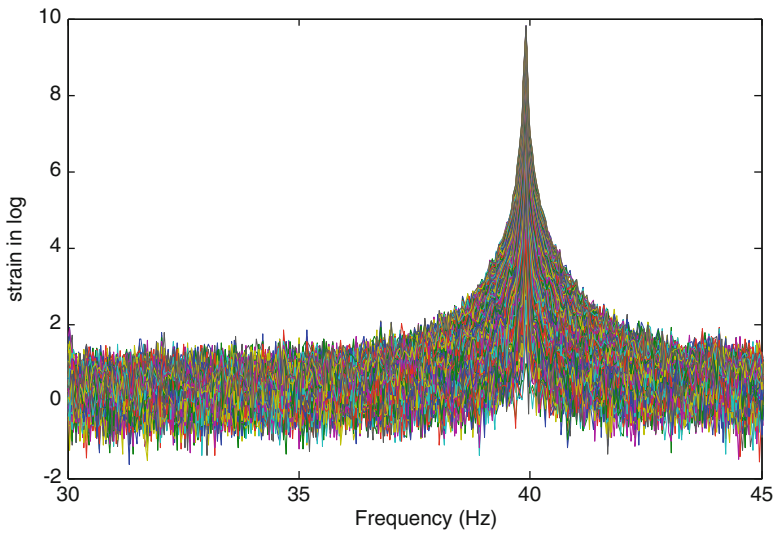

Fig. 4.12 Autospectrum from 100 fiber optic sensors for intact beam

4.5.3 Experimental Result

The fiber optic we chose is 2 m long and covers the full length of the beam, with sampling frequency 100 Hz and sensing space 2.56 mm. Two damage scenarios are performed by placing the magnetics at two different locations (285 mm left and 1170 mm left respectively). A small range 38–42 Hz around the first resonant frequency is chosen to estimate the damage features. Since sampling frequency is 100 Hz, the maximum frequency component can be observed at 50 Hz. Within the frequency range of 0–50 Hz, only the first strain mode is correctly acquired. Along this 2 m single fiber optic, 100 strain sensors with nearly 15 mm spacing are chosen. Figure 4.12 shows the autospectrum of the 100 strain sensing measurement points for intact beam.

The first scenario is adding magnetics on the left side of the beam.

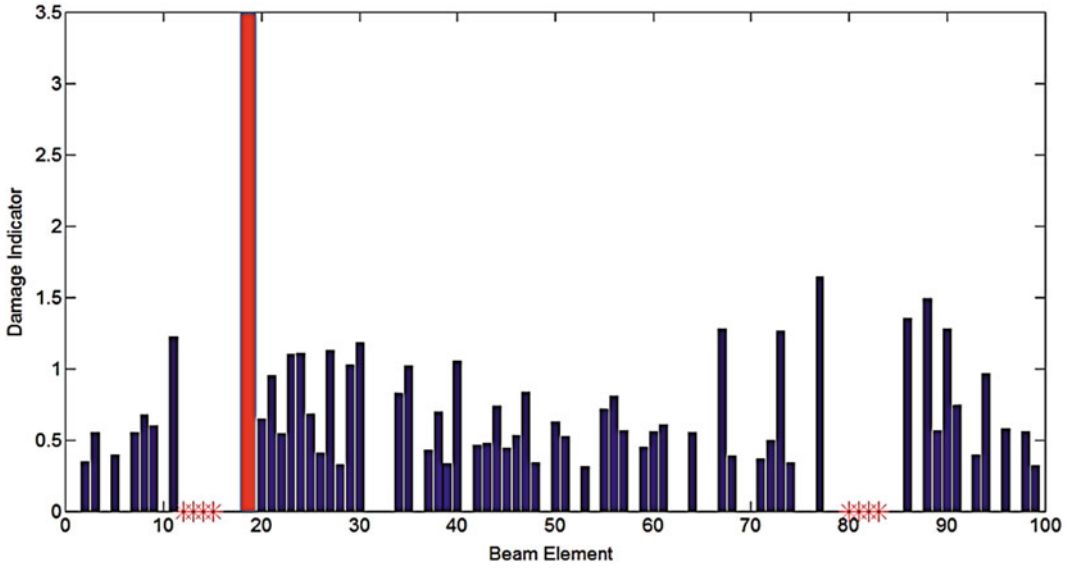

Fig. 4.13 Damage indicator of scenario 1

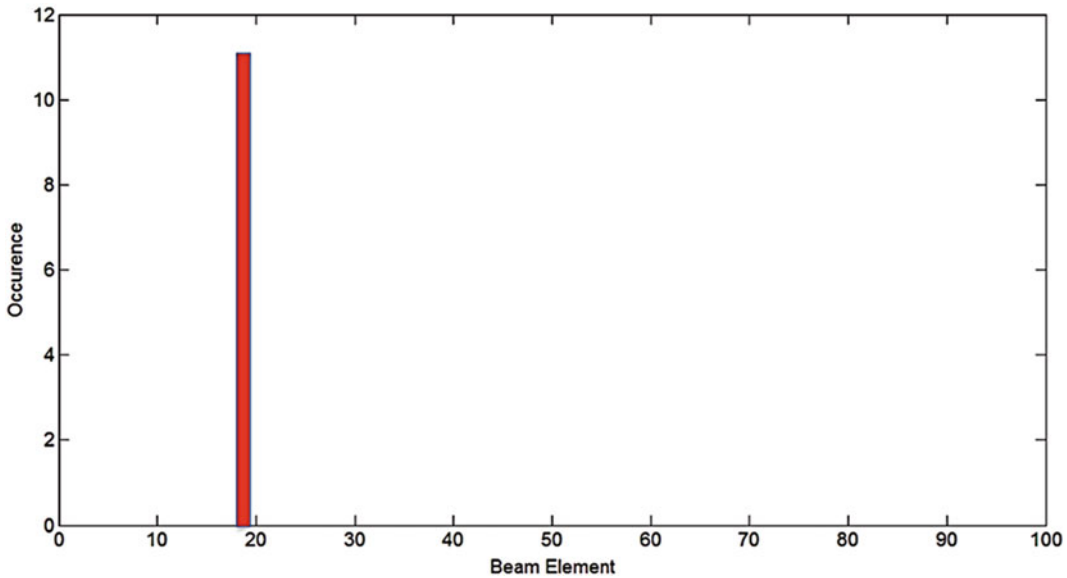

Fig. 4.14 Occurrence of scenario 1

In Fig. 4.13, red bar revealed the damage location at 19th beam element based on the damage index from Eq. (4.3) which is in accordance with the true location of additional magnets at 285 mm. Seemingly to simulations, the damage indicator in 19th element is prominent in comparison with others, which is easy to be recognized as damage component.

Occurrence damage feature has been taken into consideration as well and the identification result is shown in Fig. 4.14. Apparently, occurrence shows a clear recognition of the damage element in contrast with damage indicator of Fig. 4.13. Only one nonzero value can be seen at the 19th beam element where the magnets are placed.

Scenario two is made by adding magnetics on the right side of the beam.

In scenario 2, red bar indicates the location of additional magnets which appears at 78th beam element in Fig. 4.15. The damage identification result is in correspondence of the true location where the magnets are placed. Figure 4.16 shows the result of occurrence that points out correctly the damage location. Even though there are two small non-zero values at element 19th and element 67th but they can be neglected compared to element 78th.

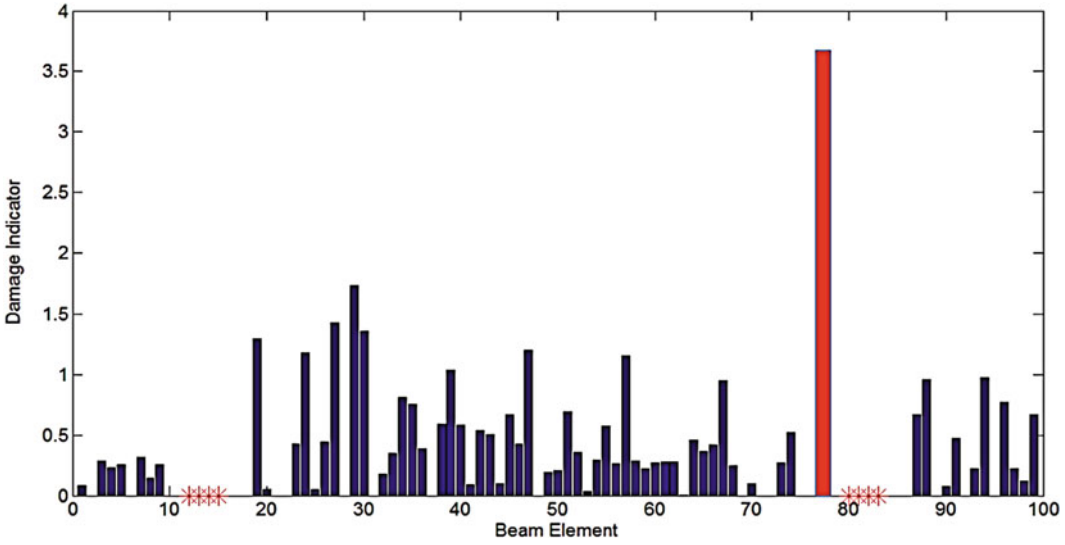

Fig. 4.15 Damage indicator of scenario 2

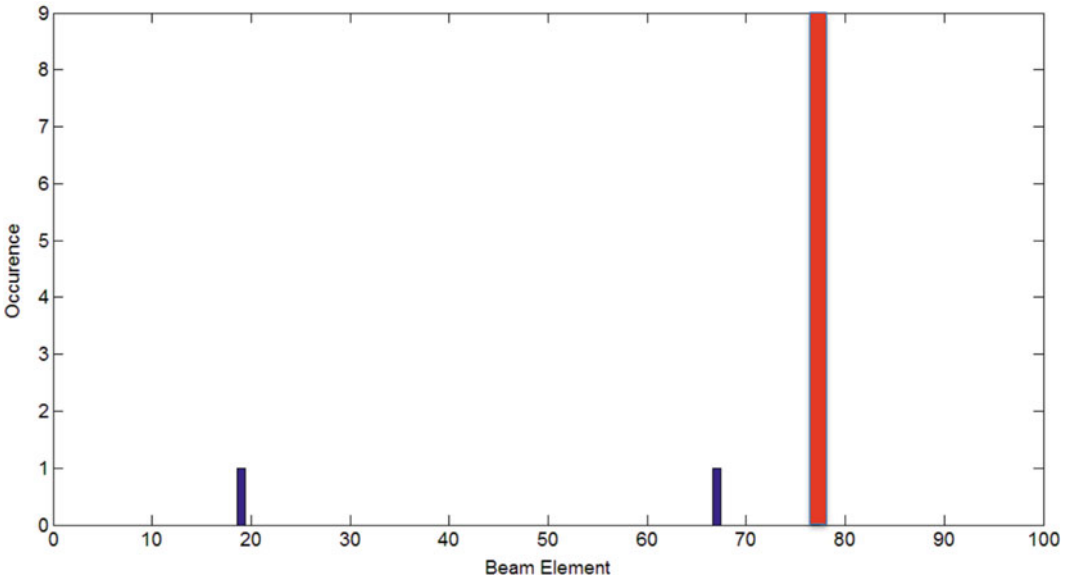

Fig. 4.16 Occurrence of scenario 2

Asterisks marked in Figs. 4.13 and 4.15 indicate the area where the damage feature is unreliable. This is due to the fact that those sensing points along the fiber are inside the area of strain nodes for the 1st strain mode which is basically equal to the curvature of the 1st mode shape of a clamped-clamped beam.

Transmissibility coherence function has been calculated in order to discard the unreliable damage indicators. It can be defined as follows:

$$C_{T_i^\varepsilon, T_{i+1}^\varepsilon}(f) = \frac{\left| G_{T_i^\varepsilon, T_{i+1}^\varepsilon}(f) \right|^2}{G_{T_i^\varepsilon, T_i^\varepsilon}(f) G_{T_{i+1}^\varepsilon, T_{i+1}^\varepsilon}(f)} \tag{4.15}$$

where $G_{T_i^\varepsilon, T_{i+1}^\varepsilon}(f)$ the cross spectral density between ith STF and $i+1$th STF, $G_{T_i^\varepsilon, T_i^\varepsilon}(f)$ and $G_{T_{i+1}^\varepsilon, T_{i+1}^\varepsilon}(f)$ are auto spectral density of ith STF and $i+1$th STF respectively. The value of $G_{T_i^\varepsilon, T_{i+1}^\varepsilon}(f)$ is always between 0 and 1 which reflects the extent of linearity between two consecutive nodes.

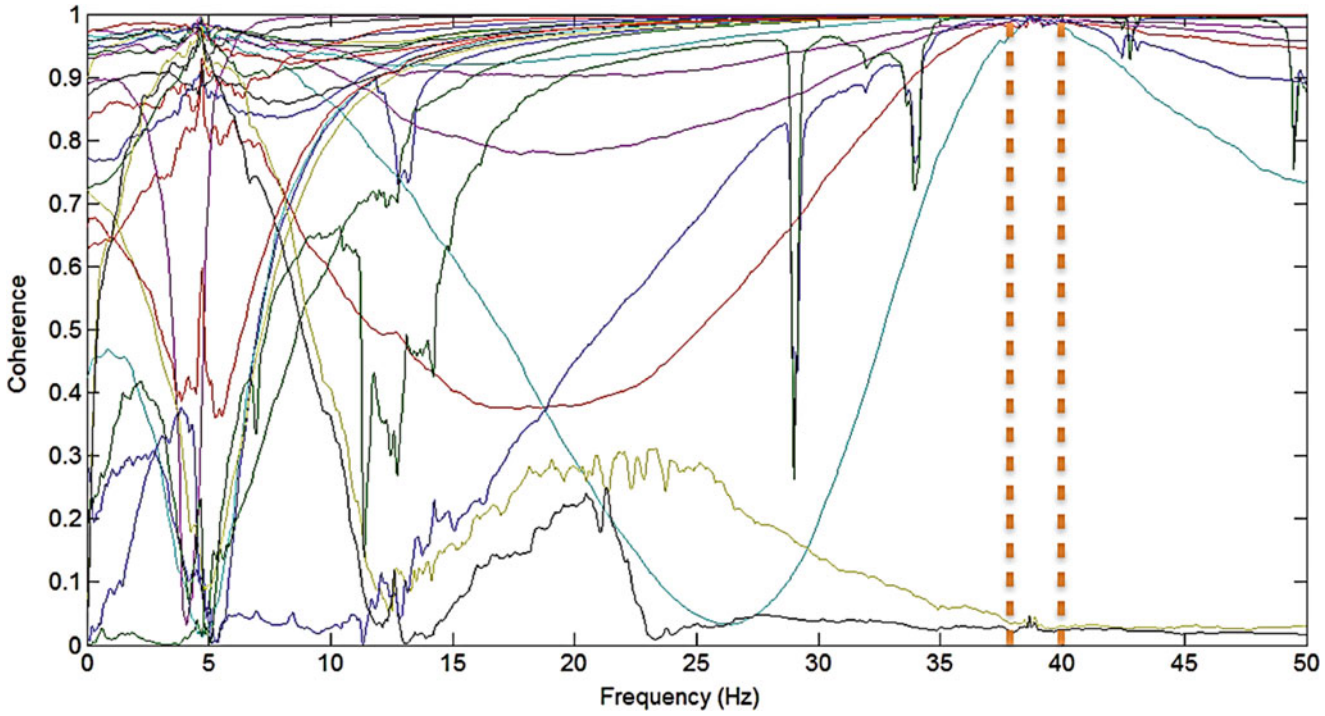

Fig. 4.17 Strain transmissibility coherence function

Figure 4.17 shows the result of coherence function among the points used to estimate the transmissibility function. In this figure, 25 beam elements (sensors) have been selected evenly from the entire 100 sensors and corresponding strain transmissibility coherence functions have been calculated. The first resonance frequency is located in the area between two dash lines. In order to discard the unreliable ones, threshold for coherence function is set as 0.9. If the coherence values are closer to 1 means the corresponding STFs are reliable. Since we are interested in the area around resonance frequency, it is easy to observe that there are two coherence functions under the threshold 0.9, actually lower than 0.1. Hence, these two corresponding damage indicators should be discarded. This gives an explanation for the results of Figs. 4.13 and 4.15 where the sensors placed near or at strain mode nodes are flagged as unreliable data.

4.6 Conclusion

In this paper, strain transmissibility function is applied to damage identification simulated by adding mass to a beam structure into one point. Based on the fact that the limit value of STFs into system poles is equal to the ratio of strain mode, which are more sensitive to damage than displacement modes, these damage features based on STF reveal to have good sensitivity to damage. Both simulation and experiment illustrate the feasibility and effectiveness of using STFs to damage identification. Concerning about the future work needed to be finished, more damage scenarios should be introduced into the structure that not only adding mass but cracks which can be regarded as nonlinear damage. More complicated structures should be testified by using STFs as well.

4.7 Funding

This study is supported by China Scholarship Council grant.

References

1. Sinou, J.-J.: A review of damage detection and health monitoring of mechanical systems from changes in the measurement of linear and non-linear vibrations. In: Sapri, R.C. (ed.) Mechanical Vibrations: Measurement, Effects and Control, pp. 643–702, 978–1–60692-037-4. Nova Science Publishers, Inc (2009)
2. Doebling, S.W., Farrar, C.R., Prime, M.B.: A summary review of vibration-based damage identification methods. Shock Vib. Dig. **30**(2), 91–105 (1998)
3. Fan, W., Qiao, P.: Vibration-based damage identification methods: a review and comparative study. Struct. Health Monit. **10**(1), 83–111 (2011)
4. Ren, W., Zong, Z.: Output-only modal parameter identification of civil engineering structures. Struct. Eng. Mech. **17**(3–4), 429–444 (2004)
5. Majumdar, A., Nanda, B., Maiti, D.K., Maity, D.: Structural damage detection based on modal parameters using continuous ant colony optimization. Adv. Civil Eng. **2014**, 174185 (2014). doi:10.1155/2014/174185
6. Chen Q., Chan Y.W., Worden K, Tomlinson G.R., Structural fault detection using neural networks trained on transmissibility functions. In: Proceedings of the International Conference on Vibration Engineering, pp. 456–646. Beijing, China (1994)
7. Sampaio R. C., Maia N. M. M., Ribeiro A. M. R. Silva J. M. M., Damage detection using the transmissibility concept. In: Proceedings of the 6th International Congress on Sound and vibration, pp. 2559–2568. Copenhagen (1999)
8. Maia, N.M.M., Ribeiro, A.M.R., Fontul, M., Montalvão, D., Sampaio, R.P.C.: Using the detection and relative damage quantification indicator (DRQ) with transmissibility. Key Eng. Mater. **347**, 455–460 (2007)
9. Liu W., Ewins D.J., Transmissibility properties of MDOF systems. In: Proceedings of the International Modal Analysis Conference No16, pp. 847–854. Santa Barbara, CA (1998)
10. Ribeiro, A.M.R., Silva, J.M.M., Maia, N.M.M.: On the generalisation of the transmissibility concept. Mech. Syst. Signal Process. **14**(1), 29–35 (2000)
11. Maia, N.M.M.: The transmissibility concept in multi-degree-of-freedom systems. Mech. Syst. Signal Process. **15**(1), 129–137 (2001)
12. Zhao, X.Y., Lang, Z.-Q., Park, G., Farrar, C.R., Todd, M.D., Mao, Z., Worden, K.: A New transmissibility analysis method for detection and location of damage via nonlinear features in MDOF structural systems. IEEE/ASME Trans. Mechatron. **20**(4), 1933–1947 (2015)
13. Lang, Z.Q., Park, G., Farrar, C.R., Todd, M.D., Mao, Z., Zhao, L., Worden, K.: Transmissibility of non-linear output frequency response functions with application in detection and location of damage in MDOF structural systems. Int. J. Nonlinear Mech. **46**(6), 841–853 (2011)
14. Lang, Z.Q., Billings, S.A.: Output frequency characteristics of nonlinear systems. Int. J. Control. **64**(6), 1049–1067 (1996)
15. Yi, X., Zhu, D., Wang, Y., Guo, J., Lee, K.-M. Transmissibility-function-based structural damage detection with tetherless mobile sensors. In: Bridge Maintenance, Safety, Management and Life-Cycle Optimization—Proceedings of the 5th International Conference on Bridge Maintenance, Safety and Management, pp. 328–335 (2010)
16. Siebel, T., Mayer, D.: Damage Detection on a Truss Structure using Transmissibility Functions, Eurodyn 2011. Leuven, Belgium (2011)
17. Devriendt, C., Guillaume, P.: Identification of modal parameters from transmissibility measurements. J. Sound Vib. **314**(1–2), 343–356 (2007)
18. Devriendt, C., Presezniak, F., De Sitter, G., Vanbrabant, K., De Troyer, T., Vanlanduit, S., Guillaume, P.: Structural health monitoring in changing operational conditions using tranmissibility measurements. Shock. Vib. **17**(4–5), 651–675 (2010)
19. Chesné, S., Deraemaeker, A.: Damage localization using transmissibility functions: a critical review. Mech. Syst. Signal Process. **38**(2), 569–584 (2013)
20. Measures, R.M.: Structural Monitoring with Fiber Optic Technology. Academic Press, San Diego, CA (2001.) Chapter 2
21. Bao, X., Chen, L.: Recent progress in distributed fiber optic sensors. Sensors (Switzerland). **12**(7), 8601–8639 (2012)
22. Hotate, K.: Distributed fiber sensing technology: currents and challenges. Opt. Pura Apl. **45**(2), 63–69 (2012)
23. Whalen, T.M.: The behavior of higher order mode shape derivatives in damaged, beam-like structures. J. Sound Vib. **309**(3–5), 426–464 (2008)

Chapter 5
Modal Parameters Estimation of an Offshore Wind Turbine Using Measured Acceleration Signals from the Drive Train

M. El-Kafafy, L. Colanero, N. Gioia, C. Devriendt, P. Guillaume, and J. Helsen

Abstract Offshore Wind Turbine (OWT) is complex structure that consists of different parts (e.g. foundation, tower, drivetrain, blades, ...). The last decade there is a continuous trend towards larger machines with the goal of cost reduction. Modal behavior is an important design aspect. For tackling NVH issues and validating complex simulation models it is of high interest to continuously track the vibration levels and the evolution of the modal parameters (resonance frequencies, damping ratios, mode shapes) of the fundamental modes of the turbine. Wind turbines are multi-physical machines with significant interaction between their subcomponents. This paper will exploit this and present the possibility of identifying and tracking consistently the structural vibration modes of the drivetrain of the instrumented offshore wind turbine by using signals (e.g. acceleration responses) measured on the drivetrain system. The experimental data has been obtained during a measurement campaign on an offshore wind turbine in the Belgian North Sea where the OWT was in standstill condition. The drivetrain, more specifically the gearbox, is instrumented with a dedicated measurement set-up consisting of 17 sensor channels with the aim to continuously track the vibration modes. The consistency of modal estimates made at consequent 10-min intervals is validated, and the dominant drivetrain modal behavior is identified.

Keywords Modal parameters • Offshore wind turbine • Drivetrain • Tower modes • Mode tracking

5.1 Introduction

There is a trend to increase the power produced by each individual turbine in order to reduce the cost of wind energy by the so-called upscaling trend. Bigger wind turbines have the advantage that they can harvest wind at higher altitudes, resulting in bigger wind speeds and allow the turbine to be equipped with bigger blades. Moreover, it is assumed that by decreasing the number of machines per Mega-watt the operations and maintenance costs of the wind park will decrease. Bigger wind turbines and corresponding blades impose higher loads on the wind turbine components, amongst others on the drive train. Moreover, these loads cannot be assumed to be quasi-static as in most industrial applications. Wind turbine loading includes aerodynamic loads at variable wind speeds, gravitational loads and corresponding bending moments, inertial loads due to acceleration, centrifugal and gyroscopic effects, operational loads such as generator torque and loads induced by certain control actions like blade pitching, starting up, emergency braking or yawing [1–4]. These dynamic loads are significantly influencing the fatigue life of the wind turbine structural components. In addition to the tower and blades also the drivetrain has several structural components for which the design is fatigue driven, such as for example the torque arms of the gearbox. In addition to turbine reliability also noise and vibration (N&V) behavior is becoming increasingly important for onshore turbines [5]. Since aerodynamic noise is decreasing by means of improved blade designs, the problem

M. El-Kafafy (✉)
Vrije Universiteit Brussel (VUB), Pleinlaan 2, B-1050 Brussel, Belgium

Helwan University, Cairo, Egypt
e-mail: melkafaf@vub.ac.be

L. Colanero • P. Guillaume • J. Helsen
Vrije Universiteit Brussel (VUB), Pleinlaan 2, B-1050 Brussel, Belgium

N. Gioia
Université Libre De Bruxelles, Brussles, Belgium

C. Devriendt
Vrije Universiteit Brussel (VUB), Pleinlaan 2, B-1050 Brussel, Belgium

OWI-lab, Brussel, Belgium

C. Niezrecki (ed.), *Structural Health Monitoring & Damage Detection, Volume 7*, Conference Proceedings of the Society for Experimental Mechanics Series, DOI 10.1007/978-3-319-54109-9_5

is shifting towards drivetrain tonalities. Accurate insights in the dynamic behavior are necessary to avoid these tonalities. This is because bigger turbines imply that the resonance frequencies of the drivetrain are decreasing towards the excitations coming from the wind turbine rotor and gears of the gearbox [4]. Therefore, the flexibility of the structural components of the drivetrain is becoming increasingly of influence on the dynamic design of the drivetrain [6]. Accurate knowledge about the resonance behavior of the drivetrain is as such essential for improved design both for fatigue and reliability as for noise. If resonances are coinciding with harmonic excitation frequencies, there is potential for increased fatigue life consumption and tonal excitation. Operational modal analysis (OMA) has proven its' use in aerospace and automotive and is increasingly used nowadays in the wind energy domain. There are different frequency ranges of interest for the wind turbine. The lower frequency range contains the more global modes of the wind turbine, such as the blade modes, tower modes and general drivetrain modes. For the drivetrain, the higher frequency ranges contain more localized modes of the gearbox and generator.

This paper discusses a preliminary study for characterizing the challenges for the use of OMA for characterizing the dynamic behavior of the wind turbine drivetrain and by extension the other main components of the turbine. In this study, we investigate both frequency ranges and show the potential for OMA techniques to characterize the eigenfrequencies value, damping and mode shape for these resonances. We want to take the initial step towards the full dynamic characterization of the wind turbine by means of accelerometers mounted on the drivetrain. Since there is the chance with OMA techniques that harmonics can be misinterpreted as resonances, we want to avoid these conditions. Therefore, the turbine is investigated while it is not producing energy. In this case, harmonics do not dominate the frequency spectrum and modal estimation can be done in a reliable way.

5.2 Data Acquisition

A long-term measurement campaign with duration of 6 months was performed on an offshore wind turbine. Instrumentation was limited to the drivetrain. In total 17 accelerometer channels were acquired. 14 channels were originating from accelerometers on the gearbox. This consisted of four tri-axial sensors and two uni-axial sensors. One tri-axial accelerometer was placed on the generator. All accelerometers used were ICP accelerometers and a sensitivity of 100 mV/g. Three accelerometers had a high sensitive frequency range between 2 and 5000 Hz, whereas the other sensors were tailored for a range between 0.5 and 5080 Hz. It can therefore be stated that the measurement set-up was tailored towards the higher frequency range identification. In addition to detailed accelerometer measurements, the speed of the wind turbine rotor is measured by means of an encoder at the low speed shaft with 128 pulses per revolution. All data is sampled at 5120 Hz. In total 160 min of data is used in the analysis done in this paper (16 datasets of 10 min each).

5.3 Operational Modal Analysis and Modal Parameters Tracking Approach

This paper investigates the turbine modal behavior while it is not producing energy. This specific operating condition will have an impact on the modal behavior observed in the drivetrain, since the teeth can be out of contact during these conditions; whereas this is necessarily the case for nominal power production [7]. Moreover, the damping properties of the wind turbine will change according to the operating conditions [8]. This study will first focus on the low frequency bandwidth to characterize the global wind turbine modes. These consist of the modes of the main turbine components such as the blades and tower. As will be shown the turbine is a multi-physical system with high interaction between the different subcomponents. Therefore, not only the drivetrain modes, but also the blade and tower resonance frequencies are present in the acceleration signals measured on the wind turbine drivetrain. This study will not go into detail on the tracking of these modes. They are used as a means to validate the validity of the measurements performed and to get confidence in the results of the OMA techniques for the estimation of the modal parameters.

For the higher frequency modes, a manual tracking approach validates the consistency of the OMA technique. Modal parameter estimations are performed for 16 consecutive time blocks of 10 min each. The eigenfrequencies and damping values of five main resonances modes are tracked for the consecutive time blocks. Peak selection is performed manually. This is done in order to show the repeatability of the analysis and to underpin the applicability of this technique for characterizing drivetrain modal behavior.

For the modal parameter estimation, the polyreference least squares complex exponential (pLSCE) estimator [9–11] was used to extract the modal parameters from the processed measured signals. The frequency-domain data, which is the input to the pLSCE estimator, is generated using the Correlogram approach [12]. So, for each data block the auto and cross correlation functions are calculated using some signals as references. Then, the spectrum for each data block is calculated by applying

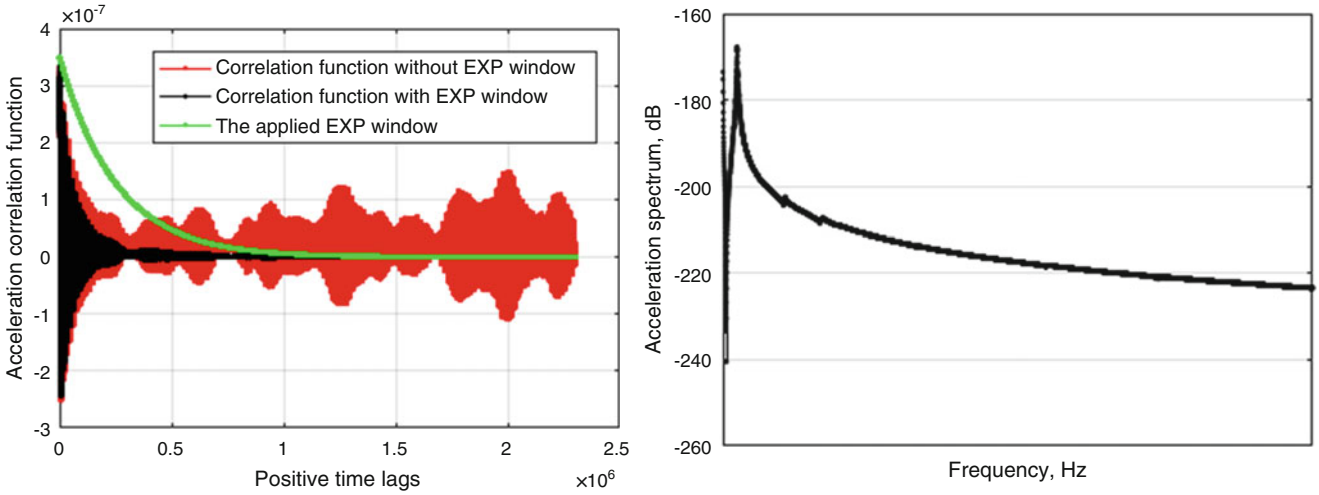

Fig. 5.1 Typical correlation function (*left*) and the corresponding spectrum (*right*) [the frequency axis is made hidden for confidentiality reason]

the FFT on the calculated auto and cross correlation functions. Figure 5.1 shows one typical correlation function and the corresponding calculated spectrum. An exponential window was applied to the correlation function before calculating the FFT to decease the leakage and noise effects. In the following, a brief description of the pLSCE estimator will be given, and the tracking steps will be summarized.

For operational modal analysis (OMA) applications, the pLSCE starts with the power spectrum of the measured outputs. The half power spectrum is defined as following in the form of a frequency-domain modal model assuming that the unmeasured inputs are white noise in the frequency band of interest:

$$S_{yy}^{+}(\omega_k) = \sum_{i=1}^{N_m} \frac{\Psi_r L_r^T}{j\omega_k - \lambda_r} + \frac{\Psi_r^* L_r^{*T}}{j\omega_k - \lambda_r^*} \in \mathbb{C}^{N_o \times N_{ref}} \tag{5.1}$$

where $\boldsymbol{S_{yy}^{+}} \in \mathbb{C}^{N_o \times N_{ref}}$ a matrix contains the positive (half) auto and cross power spectrum with $\boldsymbol{N_o}$ number of measured outputs and $\boldsymbol{N_{ref}}$ number of signals taken as references, $\boldsymbol{N_m}$ is the number of the identified modes, $\boldsymbol{\omega_k}$ is the circular frequency in r/s at frequency line $\boldsymbol{k}$, $\boldsymbol{\Psi_r} \in \mathbb{C}^{N_o \times 1}$ is the $\boldsymbol{r^{th}}$ mode shape, $\boldsymbol{L_r} \in \mathbb{C}^{N_{ref} \times 1}$ is the $\boldsymbol{r^{th}}$ operational reference factors vector, and $\boldsymbol{\lambda_r}$ is the pole of the $\boldsymbol{r^{th}}$ mode. The inverse Laplace transform of $\boldsymbol{S_{yy}^{+}(\omega_k)}$ gives the time-domain equivalent modal model that can be given as following:

$$h(kT_s) = \sum_{r=1}^{N_m} \psi_r z_r^k L_r + \psi_r^* z_r^{*k} L_r^* \tag{5.2}$$

with $z_r^k = e^{-\lambda_r k T_s}$ for the kth time sample ($k = 0, 1, 2, \cdots, N_s - 1$) and N_s is the number of time samples. Equation (5.2) is the time-domain version of the modal model (5.1) in which the "impulse" response function is decomposed as a sum of decaying sinusoids. The pLSCE estimator fits $h(kT_s)$ by means of a matrix polynomial model in a linear least-squares sense. Then, from the matrix coefficients of this polynomial the poles and the reference factors are calculated. In a second step, with having the calculated poles and the operational reference factors the mode shapes can be calculated from Eq. (5.1) as an explicit function of the poles, the operational reference factors, and the measured $S_{yy}^{+}(\omega_k)$ by solving a linear least-squares problem.

The different steps that are done to manually track the modal parameters of the different modes in the frequency-band of interest can be summarized as following:

1. Read and load the time-domain data (16 measured acceleration records of 10 min each)
2. Correlogram approach is applied to calculate the auto/cross power spectra matrix
   a. Specific signals are selected to be taken as reference signals
   b. The auto and cross correlation functions are calculated between the outputs signals and the selected reference signals
   c. Exponential window applied to the correlation functions to decrease the noise and leakage effects
   d. Fast Fourier Transform is applied to the correlation function to calculate the spectra matrix
3. The pLSCE estimator is applied to the spectra matrix with wide range of model orders

4. The stabilization diagram is constructed
5. The different physical modes are manually selected from the stabilization diagram
6. Damping is corrected to remove the exponential window effects
7. Tracking frequencies, damping values and mode shapes

This tracking approach will be applied to 16 datasets of 10 min collected during the measurements campaign on the drivetrain of the instrumented offshore wind turbine while the wind turbine was in stand still condition. It should be mentioned here that for the modes selection from the stabilization diagrams over the different datasets, efforts have been made to select as much as possible the same mode at the same model order.

5.4 Results and Discussions

As it was mentioned in the introduction and Sect. 5.3, the main objective of this measurement campaign was to do dynamic characterization of the drivetrain of the instrumented OWT. Since a detailed knowledge about the specifics of the drivetrain itself is not available, it is suggested to first validate the quality of the measurements and the reliability of the tracking approach (i.e. data preprocessing, modal parameter estimation step, etc). To do so, a short-term tracking of the modal parameters of the modes of the turbine's tower and blades will be done over the different 16 datasets measured from the drivetrain, and the results from this analysis will be compared to the ones obtained using signals acquired from sensors mounted on the tower of the same turbine. These modes are detected in the low frequency range. After validating the measurements quality and the reliability of the modes tracking approach, analysis in a bit higher frequency band will be done with the aim to track some physical vibration modes of the drivetrain itself. In the analysis of both the high and low frequency-bands, the frequency values will not be shown for confidentiality reason.

5.4.1 Low Frequency-Band Analysis

According to the results obtained using signals acquired from some accelerometers mounted on the tower of the instrumented turbine, It can be concluded that the physical vibration modes of the tower and the foundation system of the instrumented OWT are dominantly present in the low frequency band and they are labeled as following:

- First for-aft bending tower mode (FA1)
- First side-side bending tower mode (SS1)
- Mode with a second for-aft bending mode tower component (FA2)
- Mode with a second side-side bending mode tower and nacelle component (SS2N)
- Mode with a second for-aft bending mode tower and nacelle component (FA2N)

In addition to the tower modes, some other modes related to the blades and the drivetrain can be also detected in this low frequency band. Those modes are the first drivetrain torsional mode (DTT1), the first blade asymmetric flapwise pitch (B1AFP) mode, the 1st blade asymmetric flapwise yaw (B1AFY) mode, the 1st blade collective flap (B1CF) mode, and the 1st blade asymmetric edgewise yaw (B1AEY) mode.

The tracking approach explained in Sect. 5.3 is applied to the 16 datasets of 10 min each acquired from the accelerometers mounted on the drivetrain of the instrumented OWT. Figure 5.2 shows an example for the stabilization diagram constructed by the pLSCE estimator in the low frequency-band. The shown stabilization diagram indicates that there are several modes located in that band. The dominant peak corresponds to the first for-aft (FA1) and first side-side (SS1) bending modes of the tower, which are characterized by a lot of motion at the nacelle level according to the visualization of their mode shapes. The most dominant modes of the tower, blades, and drivetrain are estimated and tracked over the 16 datasets measured from the drivetrain sensors. The standard deviation values of the estimated resonance frequencies values of the tower and blades modes are presented in Tables 5.1 and 5.2. From Table 5.1, one can see that the most dominant tower modes are successfully detected except the third mode, i.e. FA2. Based on the mode shapes results of the tower modes estimated using sensors mounted on the tower itself, it was noted that the FA2 mode is mostly dominated by tower motion and not a motion at the nacelle level. This can explain why this mode is not well-detected using signals measured from the drivetrain system. It can be seen from Table 5.1 that the frequency of the third mode (i.e. SS2N) is estimated with a higher uncertainty in comparison with the other tower modes. This can be explained by the fact that it was noted from the tower mode shapes that the motion at the nacelle level is less for the SS2N mode in comparison with the FA1, SS1, and FA2N modes. In general, the low standard deviation values shown in Tables 5.1 and 5.2 confirms that the tower and the blades modes are successfully and consistently estimated over the different 16 datasets.

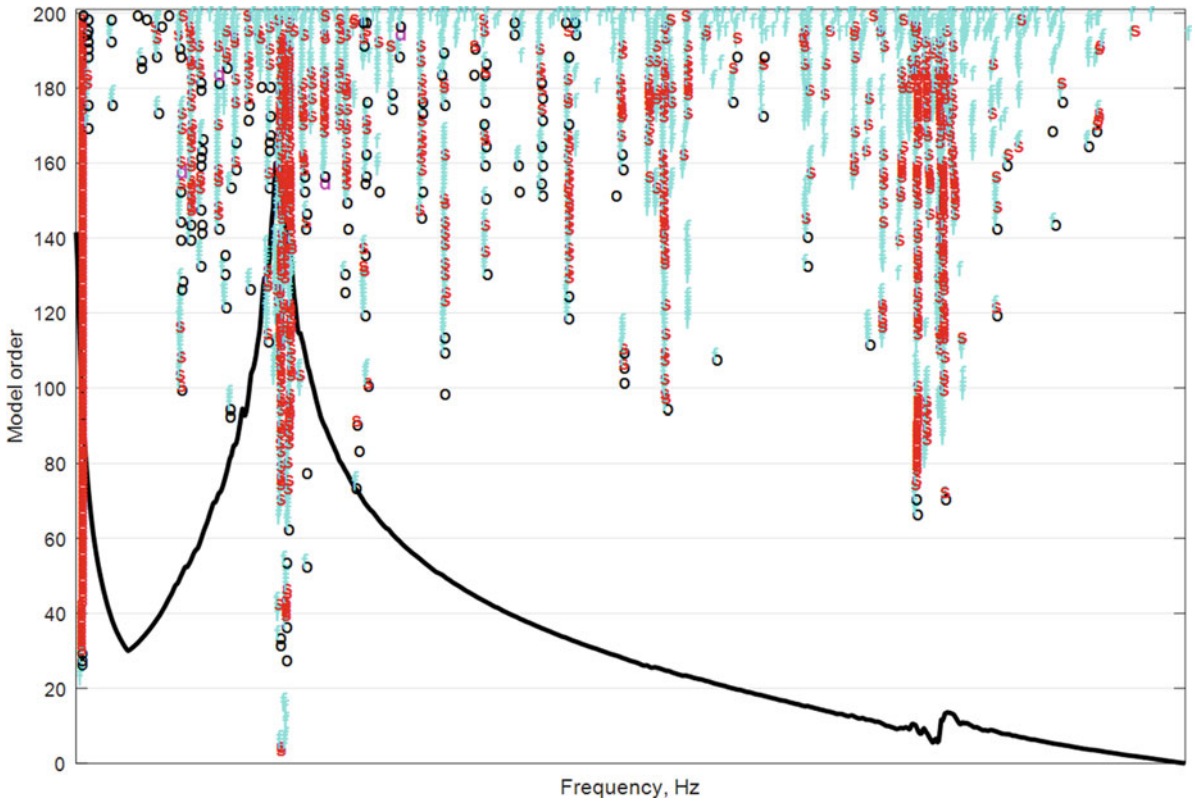

Fig. 5.2 Low frequency band analysis: typical stabilization diagram constructed by the pLSCE estimator

Table 5.1 Results of the short-term tracking of the low frequency-band modes (Tower modes)

Mode	Std freq. Hz
FA1	0.007
SS1	0.003
SS2N	0.022
FA2N	0.006

Table 5.2 Results of the short-term tracking of the low frequency-band modes (Blade and drivetrain modes)

Mode	Std freq. Hz
B1AEY	0.021
B1AFP	0.031
B1AFY	0.015
B1CF	0.005
DTT1	0.028

A comparison between the tower modes frequencies estimated using the drivetrain signals and the signals measured on the tower of the same turbine is shown in Fig. 5.3. From this figure it can be seen that the mean values agree very well and the confidence bounds are overlapping. The higher standard deviation on the SS1 and FA2N modes estimated using tower signals is really due to the fact that these estimates are calculated based on 2016 datasets representing a monitoring period of 2 weeks. Therefore, this higher standard deviation is mainly driven by the environmental variations rather than the quality of the estimation itself. It is also noted that the frequency values obtained for the blades modes agree very well with the ones estimated when processing the signals measured from sensors mounted on the tower. In Fig. 5.4, the mode shapes of the drivetrain system at the FA1 and SS1 resonance frequencies are shown. From these mode shapes, one can see that the movement of the drivetrain system resembles the tower movement where it goes in the for-aft direction (x-dir.) at the tower FA1 frequency and in the side-side direction (Y-dir.) at the tower SS1 frequency. Therefore, the consistency of the obtained results the ones obtained from signals measured directly on the tower of the same turbine confirms the correctness of the measurements, especially considering that the sensors that have been used on the drivetrain are aimed towards higher frequency region for dynamic analysis of the drivetrain.

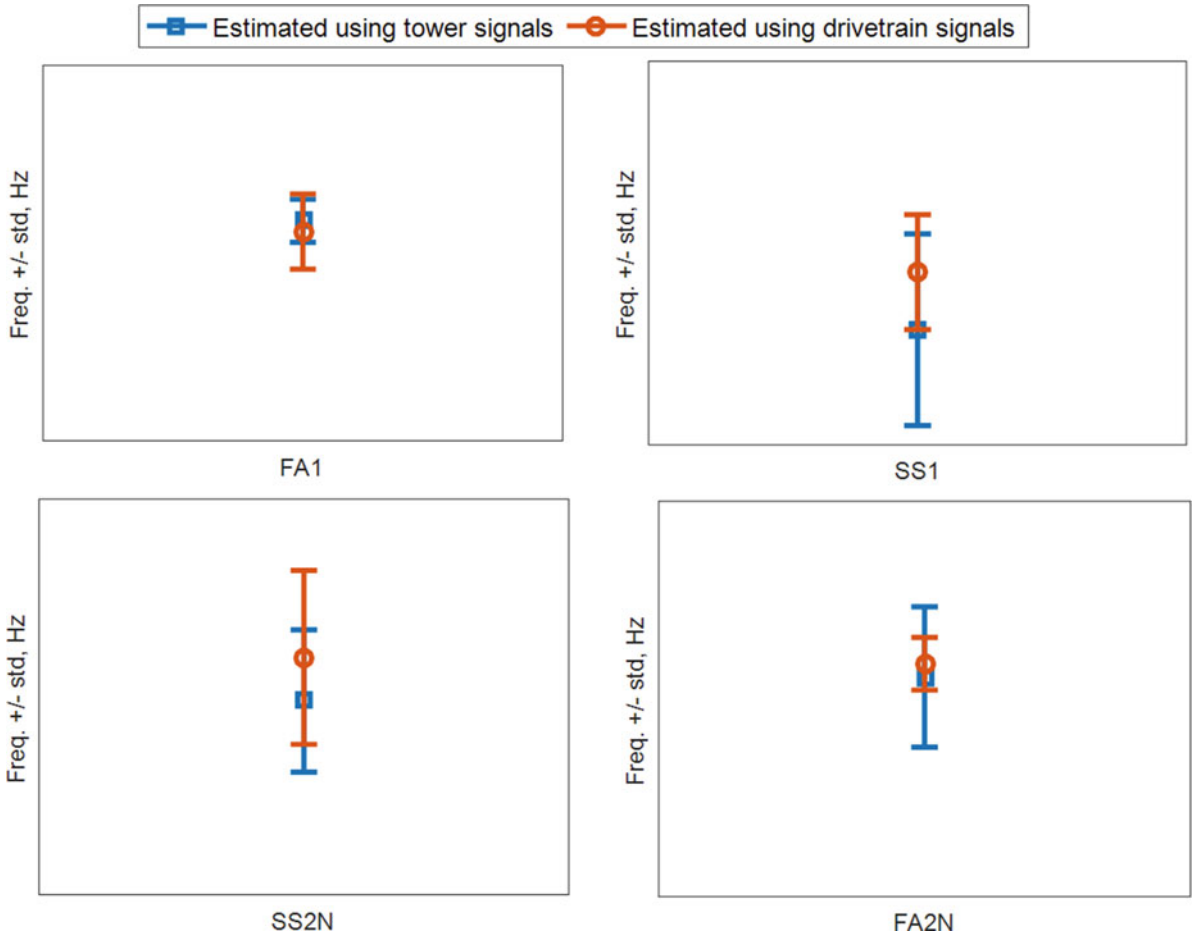

Fig. 5.3 Low frequency-band analysis: Comparison between the estimated resonance frequencies values of the tower global modes using the drivetrain signals and tower signals

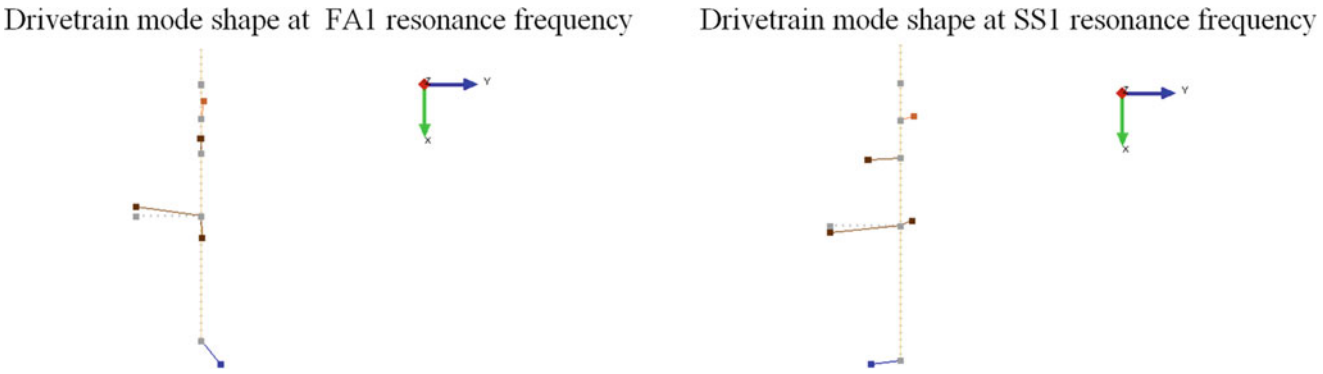

Fig. 5.4 The drivetrain mode shapes corresponded to the tower FA1 frequency (*left*) and at the tower SS1 frequency (*right*) (*Y*: Side-Side direction *X*: For-Aft direction *Grey dots*: undeformed model)

5.4.2 High Frequency-Band Analysis

Using the 16 datasets of the acceleration signals measured from the drivetrain system and by means of the tracking approach presented in Sect. 5.3 the first results of the short-term tracking of some modes of the drivetrain will be presented in this section. The analysis frequency band will be extended a bit in comparison to Sect. 5.4.1 to include some higher frequency modes, which are thought to be mainly the drivetrain modes. Figure 5.5 shows one stabilization diagram constructed by the pLSCE estimator in the frequency band of interest. The blue arrows in the stabilization diagram refer to the five modes

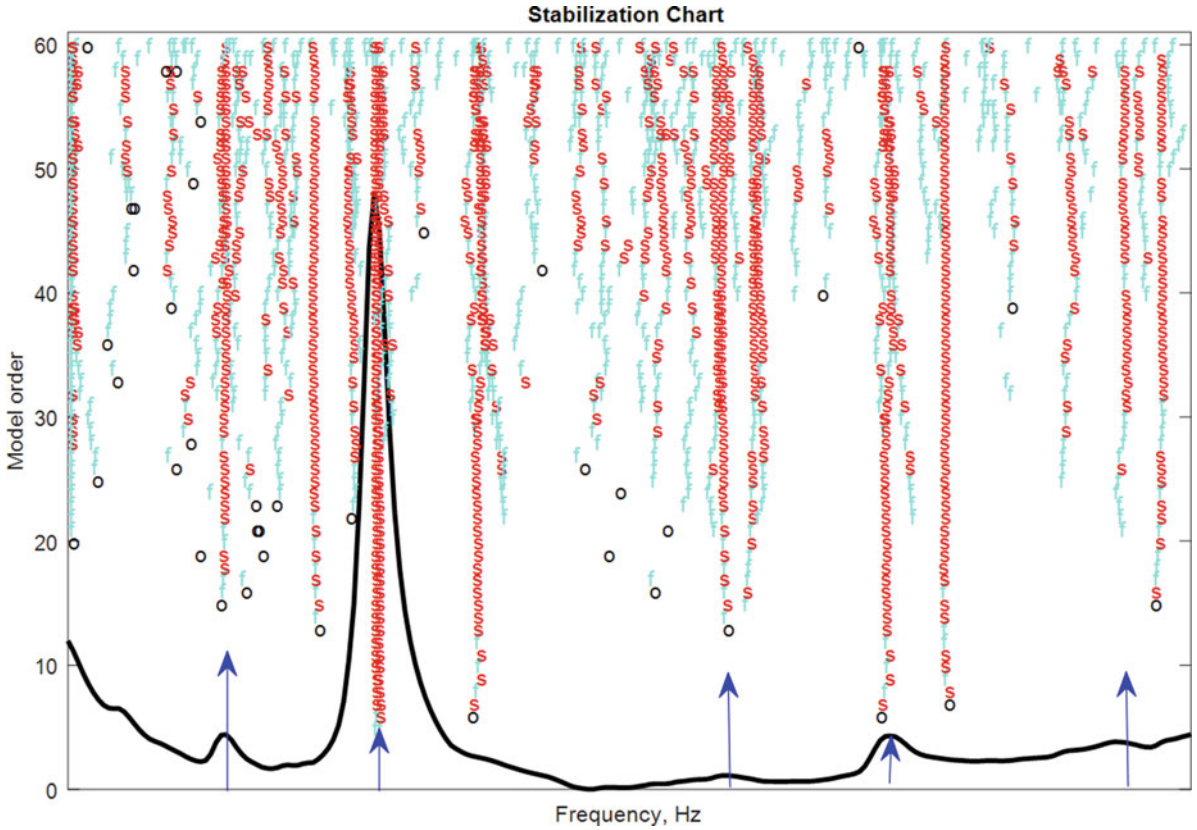

Fig. 5.5 Higher frequency-band analysis: stabilization chart constructed by the pLSCE estimator [the frequency axis is made hidden for confidentiality reason]

that will be tracked over the 16 datasets. These modes are selected after doing some preliminary analysis like, checking the correlation of the mode shapes between the different modes in the band (i.e. MAC criterion), checking the rate of the existence of the mode in all the 16 datasets, and the coincidence of the mode to a peak in the spectrum. The result of the short-term tracking in terms of the resonance frequencies and damping ratios of the five modes is shown in Fig. 5.6. This figure illustrates one box and whisker plot per frequency and damping value of each tracked mode. The results in this figure show that for all the modes the resonance frequency values show high level of consistency over the different data blocks. In terms of damping value, the second, third, fourth, and fifth modes show low scatter in comparison to the first mode. This level of the consistency of the results over the different 16 processed datasets shows the repeatability of the analysis and underpins the applicability of the measurements and the modal estimation approach for the characterizing drivetrain model behavior.

5.5 Conclusions

The modal behavior of an OWT is investigated while the OWT was in stand still condition. The investigation is done by performing a short-term manual tracking of the modal parameters of the different components of the turbine, e.g. tower, blades, and drivetrain system. The signals used to estimate the modal parameters are 17 acceleration signals acquired from tri-axial and uni-axial accelerometers mounted on the drivetrain system (i.e. gearbox and generator) of the turbine. In the low frequency-band analysis, the consistency of the obtained results with the ones obtained when using signals measured from sensors mounted on the turbine's tower confirms the validity of the measurements performed and give confidence in the OMA technique used for the estimation of the modal parameters. The analysis done in the high frequency-band is an initial step towards the full dynamic characterization of the modal behavior of the drivetrain system. The results there show the repeatability of the analysis and confirm the applicability of the used technique for characterizing the drivetrain modal behavior considering stand still condition. Further investigations for the modal behavior of the drivetrain will be continued, and an automatic tracking approach could be done.

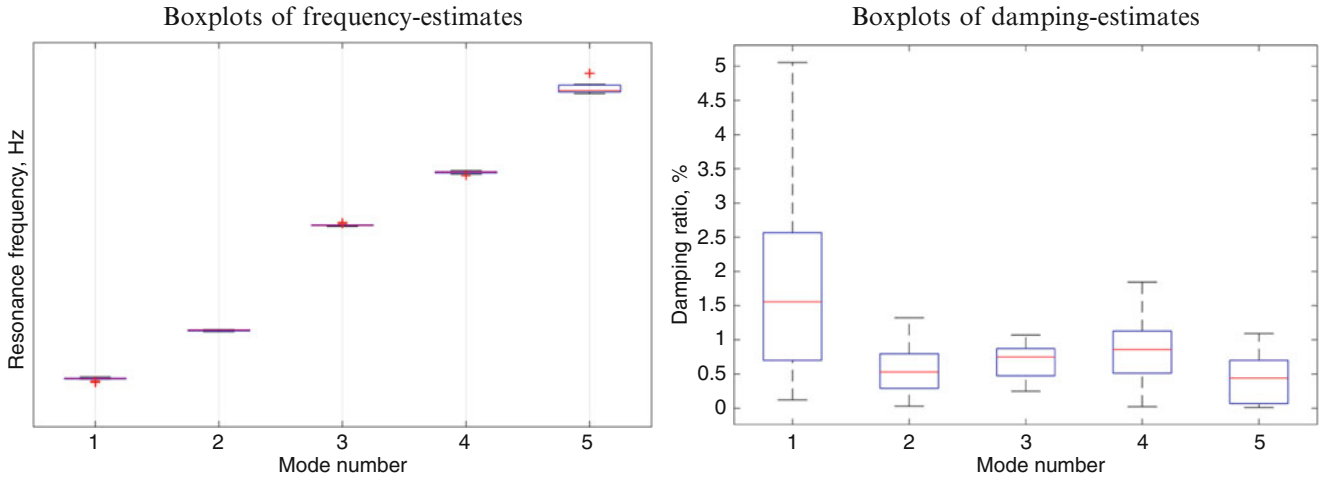

Fig. 5.6 Boxplots of the frequencies (*left*) and damping values (*right*) of the five dominant modes in the high-frequency band. On each box, the central mark is the median, the edges of the box are the 25th and 75th percentiles, the whiskers extend to the most extreme values that were not considered as outliers and the outliers are plotted individually using the '+' symbol

Acknowledgements The authors would like to acknowledge the VLAIO SBO HYMOP and Proteus Project, as well as the farm owner and OEM for facilitating the measurement campaign.

References

1. Veers, S.P.: Three-dimensional wind simulation. Technical report SAND88e 0152.UC-261, Sandia (1988)
2. Mann, J.: Wind field simulation. Prob Eng Mech. **13**(4), 269e82 (1998)
3. Peeters J. Simulation of dynamic drive train loads in a wind turbine. PhD thesis, Division PMA, Department of Mechanical Engineering, Belgium: Katholieke Universiteit Leuven, Leuven (Heverlee) (2006). Available online: http://hdl.handle.net/1979/344
4. Peeters, J., Vandepitte, D., Sas, P.: Analysis of internal drive train dynamics in a wind turbine. Wind Energy J. **9**, 141e61 (2006)
5. Goris, S., Ribbentrop, A., et al.: A validated virtual prototyping approach for avoiding wind turbine tonality. In: 5th International Conference on Wind Turbine Noise Denver (2013)
6. Helsen J. The dynamics of high power density gearboxes with special focus on the wind turbine application. PhD thesis, Division PMA, Department of Mechanical Engineering, Belgium: Katholieke Universiteit Leuven, Leuven (Heverlee) (2012)
7. Vanhollebeke, F., Peeters, P., Helsen, J., Di Lorenzo, E., Manzato, S., Peeters, J., Vandepitte, D., Desmet, W.: Large scale validation of a flexible multibody wind turbine gearbox model. J. Comput. Nonlinear Dyn. **10**(4), 041006 (2015)
8. Weijtjens W., Shirzadeh R., De Sitter G., Devriendt C. Classifying resonant frequencies and damping values of an offshore wind turbine on a monopole foundation for different operational conditions. In: Proceedings of EWEA, Copenhagen (2014)
9. Brown, D.L., Allemang, R.J., Zimmerman, R., Mergeay, M.: Parameter estimation techniques for modal analysis. SAE Transactions, paper No. 790221, vol. 1979, pp. 828–846 (1979)
10. Vold, H., Numerically robust frequency domain modal parameter estimation, Sound and Vibration, 24(1), 38–40.
11. Vold, H., Kundrat, J., Rocklin, G., Russel, R.: A multi-input modal estimation algorithm for mini-computers. SAE Trans. **91**(1), 815–821 (1982)
12. Bendat, J., Piersol, A.: Random Data: Analysis and meaurment procedures. Wiley, New York (1971)

Chapter 6
Structural Damage Detection in Real Time: Implementation of 1D Convolutional Neural Networks for SHM Applications

Onur Avci, Osama Abdeljaber, Serkan Kiranyaz, and Daniel Inman

Abstract Most of the classical structural damage detection systems involve two processes, feature extraction and feature classification. Usually, the feature extraction process requires large computational effort which prevent the application of the classical methods in real-time structural health monitoring applications. Furthermore, in many cases, the hand-crafted features extracted by the classical methods fail to accurately characterize the acquired signal, resulting in poor classification performance. In an attempt to overcome these issues, this paper presents a novel, fast and accurate structural damage detection and localization system utilizing one dimensional convolutional neural networks (CNNs) arguably for the first time in SHM applications. The proposed method is capable of extracting optimal damage-sensitive features automatically from the raw acceleration signals, allowing it to be used for real-time damage detection. This paper presents the preliminary experiments conducted to verify the proposed CNN-based approach.

Keywords Real-time structural damage detection • Damage identification • Structural health monitoring • Convolutional neural networks • Infrastructure health

6.1 Introduction

Regular inspection of large infrastructure is a time and resource consuming process. Therefore, several structural damage detection systems have been developed in an attempt to automatically identify and localize the damage. Previous studies suggest that nonparametric global damage detection methods are ideal for monitoring of large civil structures [1, 2]. These methods utilize statistical techniques to analyze the measured vibration response in order to evaluate the condition of the monitored structure [3].

Recently, researchers started to explore machine learning approaches to develop new nonparametric global methods for damage detection. Generally, the currently available machine learning based damage detection approaches involve two tasks, feature extraction and classification. The first task requires extracting hand-crafted features that capture the most distinctive information in the measured acceleration signals which can be correlated to the structural damage. The second task involves training a certain classifier that is used to classify the extracted features and identify the structural damage. Several features and classifiers have been implemented in structural damage detection systems. Examples of the feature extraction techniques used for machine learning based damage detection include principal component analysis [4], autoregressive modeling [5], simple statistical analysis [6], and wavelet transform [7]. Also, artificial neural networks [4] and support vector machine [8] are some examples of the classifiers used for feature classification.

It is obvious that the performance of machine learning based damage detection methods relies on the hand-crafted features as well as the selected classifier. Consequently, one should be careful when choosing the extracted features to ensure that they characterize the most important information in the analyzed signals. Additionally, based on the extracted features, a suitable classifier should be trained to classify these features correctly. Therefore, researchers usually follow a trial-and-error approach in an attempt to obtain the best features/classifier combination. However, there is no guarantee that a particular

O. Avci (✉) • O. Abdeljaber
Department of Civil and Architectural Engineering, Qatar University, Doha, Qatar
e-mail: onur.avci@qu.edu.qa

S. Kiranyaz
Department of Electrical Engineering, Qatar University, Doha, Qatar

D. Inman
Department of Aerospace Engineering, University of Michigan, Ann Arbor, MI, USA

C. Niezrecki (ed.), *Structural Health Monitoring & Damage Detection, Volume 7*, Conference Proceedings of the Society for Experimental Mechanics Series, DOI 10.1007/978-3-319-54109-9_6

Fig. 6.1 Qatar University grandstand simulator

combination which appeared to be appropriate for a certain structure would be a suitable choice for other structures. Certainly, extracting sub-optimal features or using unsuitable classifier will adversely affect the performance of the damage detection system. Another issue is that the feature extraction/classification approach requires large computational effort, which prevents the use of machine learning based methods for real-time SHM.

The study presented in this paper attempts to resolve the problems associated with the classical machine learning based methods by using 1D convolutional neural networks (CNNs). One of the most attractive attributes of CNNs is that they merge feature extraction and classification tasks into a compact learning body. Therefore, CNNs are capable of learning the optimal features and classifier parameters based on the raw data only. Recent studies have shown that CNNs outperform conventional machine learning methods in many problems such as object recognition in images [9], classification of electrocardiogram (ECG) signals [10], and fault detection in power engines [11].

Researchers at Qatar University (QU) are currently conducting extensive experimental and analytical studies on SHM of stadiums. Therefore, a large grandstand simulator with a footprint dimension of 4.2 × 4.2 m is being constructed at QU to serve as a test bed [12]. So far, only the main steel frame of the grandstand simulator has been constructed as shown in Fig. 6.1. This steel frame has several beam-to-girder connections which can be loosened to simulate structural damage (stiffness loss at the joints). The research team employs the structure to test different damage detection algorithms before finalizing the construction. This paper reports the preliminary experimental results on the QU grandstand simulator to validate the proposed CNN-based damage detection algorithm.

The rest of this paper is organized as follows. Section 6.2 briefly explains 2D and 1D CNNs. Section 6.3 introduces the proposed damage detection algorithm. Section 6.4 details the preliminary experiments conducted to verify the CNN-based algorithm. Finally, the experimental results are discussed in Sect. 6.5, while the conclusions are provided in Sect. 6.6.

6.2 1D and 2D CNNs

CNNs are feedforward neural network with a neuron pattern inspired by the structure of human visual cortex. Standard CNNs (i.e. 2D CNNs) are typically used for classifying two-dimensional inputs such as videos and images, while 1D CNNs are used to analyze 1D signals. A standard 2D CNN with an input layer of size 28 × 28 is shown in Fig. 6.2. This CNN contains alternating convolution and sub-sampling layers followed by a number of multi-layer perceptron (MLP) layers. The MLP layers process the outputs of the convolution layers to generate an output vector that represents the classification of the input signal. The architecture of a 2D CNN depends on the sizes of the convolution layers and the sizes of the MLP layers of the kernel size and the sub-sampling factor, which were set in Fig. 6.2 as 5 and 2, respectively. Unlike traditional filters that have predefined parameters, the parameters of the 2D filter kernels in CNNs are automatically optimized by back propagation.

1D CNNs are similar to their 2D counterparts but with some structural differences [10]. Obviously, the main difference is that the 1D CNNs deals with 1D arrays rather than 2D matrices, which means that 2D matrix operations in 2D CNNs should be replaced by their 1D equivalents. Also, similar to the 2D CNNs, the training of 1D CNNs is carried out through back propagation. The reader is referred to [10] for more details on the forward and back propagation operations in 1D CNNs.

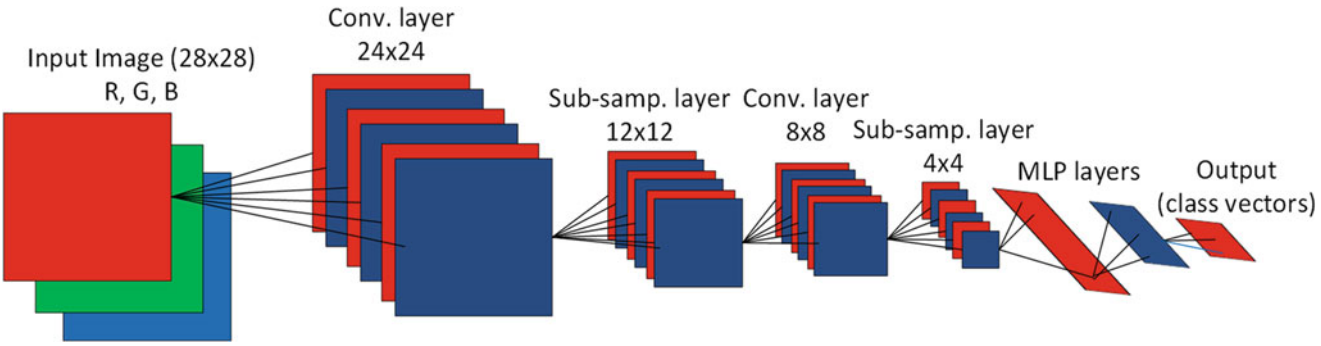

Fig. 6.2 A standard 2D CNN [10]

6.3 The Proposed CNN-Based Algorithm

As shown in Fig. 6.1, the steel frame of QU grandstand simulator has 25 filler beams connected to six horizontal beams. Structural damage can be simulated by loosening the bolts at beam-to-girder connections. In this preliminary study, only the five connections marked in Fig. 6.1 were considered. As explained in Sect. 6.4, an accelerometer is placed at each one of these five joints. Also, a modal shaker is used to apply random excitation to the structure. The proposed CNN-based algorithm is supposed to analyze the five acceleration signals in order to identify the damage and locate the damaged joint (if any).

The main idea of the proposed algorithm is to train a single 1D CNN classifier for each joint. This classifier is supposed to process the acceleration signal measured at its corresponding joint and determine whether this joint is damaged or not. To train the five CNNs corresponding to the five joints, it is required to obtain a data set that contains undamaged and damaged acceleration signals collected at each joint. To generate this data set, it is required to conduct a total of $5 + 1 = 6$ experiments. In the first experiment $E = 1$, the five acceleration signals are measured under random excitations while the five joints are undamaged. The signals measured in this experiment are denoted as $U_{E=1,J=1}, U_{E=1,J=2}, \ldots, U_{E=1,J=5}$, where J is the joint number, E is the experiment number, and U indicates that the signal was measured while the joint is undamaged. In each experiment $k + 1$ ($1 \leq k \leq 5$), the k^{th} joint is damaged by loosening its bolts, and the five acceleration signals are measured under random excitation. The resulting signals are denoted as $U_{E=k+1,J=1}, \ldots, D_{E=k+1,J=k}, \ldots, U_{E=k+1,J=5}$, where the notation D indicates that the signal was measured while the corresponding joint is damaged.

After conducting the experiments, the undamaged and damaged signals measured at each joint i are grouped together to create the vectors required for training the CNNs:

$$\text{Undamaged}_i = [U_{E=1,J=i} \quad \cdots \quad U_{E=i,J=i} \quad U_{E=i+2,J=i} \quad \cdots \quad U_{E=6,J=i}] \tag{6.1}$$

$$\text{Damaged}_i = [D_{E=i+1,J=i}] \tag{6.2}$$

Next, the vectors are divided to a large number of frames having n_s samples. The resulting frames at each joint i can be represented as:

$$\text{UF}_i = \begin{bmatrix} \text{UF}_{i,1} & \text{UF}_{i,2} & \cdots & \text{UF}_{i,n_{\text{uf}}} \end{bmatrix} \tag{6.3}$$

$$\text{DF}_i = \begin{bmatrix} \text{DF}_{i,1} & \text{DF}_{i,2} & \cdots & \text{DF}_{i,n_{\text{df}}} \end{bmatrix} \tag{6.4}$$

where UF_i and DF_i contain the undamaged and damaged frames corresponding to the joint i, respectively, and n_{uf} and n_{df} are the number of undamaged and damaged frames, respectively. Given the total number of samples in each acceleration signal n_T, n_{uf} and n_{df} can be computed as

$$n_{\text{uf}} = n \times \frac{n_T}{n_s} \tag{6.5}$$

$$n_{\text{df}} = \frac{n_T}{n_s} \tag{6.6}$$

After that, the frames stored in vectors UF_i and DF_i are normalized between -1 to 1 resulting in the vectors UFF_i and DFF_i. Finally, based on the data in UFF_i and DFF_i, a 1D CNN classifier CNN_i is trained using back-propagation algorithm.

Once the five CNNs are trained, they can be easily used to evaluate the condition of the five joints. The following procedure explain how to use each CNN to obtain an index that represents the probability of damage at joint i directly from the raw acceleration measurements:

1. Apply damage at one of the five joints (or keep them undamaged).
2. Apply a random shaker input.
3. Measure the acceleration signal at each joint.
4. Divide each acceleration signal to a number of frames each containing a total of n_s samples.
5. Normalize the frames between -1 to 1.
6. Feed the normalized frames measured at each joint to the corresponding CNN (CNN_i).
7. Compute the probability of damage (PoD_i) at the i^{th} joint as below:

$$\text{PoD}_i = \frac{D_i}{T_i} \tag{6.7}$$

where T_i is the total number of frames processed by CNN_i, and D_i is the number of frames which are classified as damaged. It is expected that the PoD computed at a damaged joint will be significantly high (close to 1.0), while the PoD obtained at an undamaged joint will be very low (close to 0.0).

6.4 Experimental Demonstration

In this section, the preliminary experimental work carried out to verify the proposed CNN-based algorithm is explained. As mentioned earlier, the objective here is to monitor five joints along a single girder in QU grandstand simulator. Therefore, five PCB model 393B04 accelerometers were attached to the girder at the locations of the five joints using 080A121 magnetic mounting plates. The random excitation was supplied by a TMS 2100E11 modal shaker. DT9857E-16 data acquisition module was used to generate the shaker's output and collect the acceleration signals.

As explained in Sect. 6.3, six experiments were conducted to collect the training data. In each experiment, the structure was subjected to 0–512 Hz random excitation and the five acceleration signals were measured at a sampling frequency of 1024 Hz. Each experiment was conducted for 256 s, which means that each acceleration signal contains $n_T = 262144$ samples. The number of samples in each frame n_s was taken as 128. A Matlab code was written and used to create the vectors UF_i and DF_i required for training the five CNNs as explained in Sect. 6.3. Also, the training of 1D CNNs through forward and back propagation was implemented in C++ using MS Visual Studio 2013 in 64-bit.

The structure of five CNNs was selected by trial-and-error. Each CNN has two convolution layers and two MLP layers. The number of neurons in the first and second convolution layers was set as 64 and 32, respectively, while the number of neurons in each MLP layer was set to 10. The kernel size K, and the sub-sampling factor ss for all CNNs are set to 41 and 2, respectively.

Once the training is complete, the performance of the five CNNs was tested against six structural cases according to the seven steps presented in Sect. 6.3. In Case 1, the five joints are kept undamaged, while the remaining cases involved damaging one of the joints. For each case, the response of the monitored girder under random excitation was collected, divided to frames, normalized, and then fed to the five CNNs to compute the PoD value at each joint. The resulting PoD distributions are presented in Fig. 6.3.

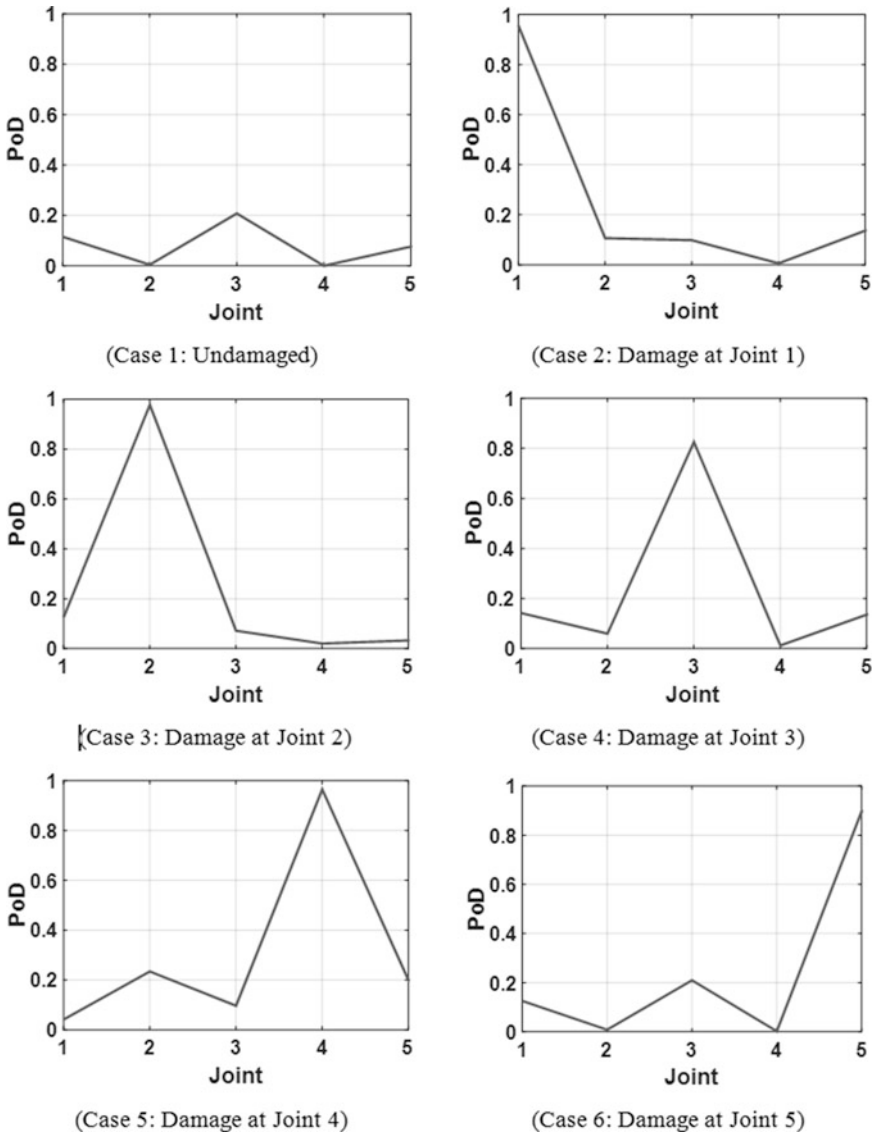

Fig. 6.3 PoD distributions computed for the six cases by the proposed algorithm

6.5 Discussions

The results of the preliminary experimental study demonstrate the efficiency of the proposed CNN-based algorithm. Looking at the PoD distributions presented in Fig. 6.3, it is clear that the PoD values computed at the undamaged joints are significantly higher than those assigned to the damaged joints. This clearly shows that the proposed algorithm was able to identify and localize very slight structural damage directly from the raw acceleration signals.

6.6 Conclusions

This paper presented a fast and accurate algorithm utilizing 1D CNNs for real-time damage detection and localization. A preliminary experimental study was conducted to verify the proposed CNN-based approach on the steel frame of QU grandstand simulator. The experimental results showed that the proposed algorithm is very promising as an alternative to the conventional machine learning based damage detection methods.

Acknowledgements The authors are grateful to SOLB26 WLL company of Qatar for providing the steel framing and installing it at the Qatar University Structures Laboratory.

References

1. Avci O, Abdeljaber O, Self-organizing maps for structural damage detection: a novel unsupervised vibration-based algorithm. J. Perform. Constr. Facil. **30**(3) 04015043 (2015). doi:10.1061/(ASCE)CF.1943-5509.0000801
2. Abdeljaber O, Avci O, Do N.T., Gul M., Celik O., Catbas F.N., Quantification of structural damage with self-organizing maps BT—Structural health monitoring, damage detection and mechatronics. In: Wicks A., Niezrecki C. (eds.) Proceedings of the 34th IMAC, A Conference and Exposition on Structural Dynamics 2016, vol. 7, pp. 47–57. Springer International Publishing, Cham (2016). doi:10.1007/978-3-319-29956-3_5
3. Abdeljaber O., Avci O., Nonparametric structural damage detection algorithm for ambient vibration response: utilizing artificial neural networks and self-organizing maps. J. Archit. Eng. **22**(2) 04016004 (2016). doi:10.1061/(ASCE)AE.1943-5568.0000205
4. Dackermann U., Li J., Samali B., Dynamic-based damage identification using neural network ensembles and damage index method. Adv. Struct. Eng. **13**, 1001–1016 (2010). doi:10.1260/1369-4332.13.6.1001
5. Figueiredo E., Park G., Farrar C.R., Worden K., Figueiras J., Machine learning algorithms for damage detection under operational and environmental variability. Struct. Health Monit. **10**, 559–572 (2011). doi:10.1177/1475921710388971
6. Chun, P., Yamashita, H., Furukawa, S.: Bridge damage severity quantification using multipoint acceleration measurement and artificial neural networks. Shock. Vib. **2015**, 1–11 (2015)
7. Liu Y.-Y., Ju Y.-F., Duan C.-D., Zhao X.-F., Structure damage diagnosis using neural network and feature fusion. Eng. Appl. Artif. Intell. **24**, 87–92 (2011). doi:10.1016/j.engappai.2010.08.011
8. Santos A., Figueiredo E., Silva M.F.M., Sales C.S., Costa J.C.W.A., Machine learning algorithms for damage detection: Kernel-based approaches. J. Sound Vib. **363**, 584–599 (2016). doi:10.1016/j.jsv.2015.11.008
9. Scherer D., Müller A., Behnke S., Evaluation of pooling operations in convolutional architectures for object recognition. In: Proceedings of the 20th International Conference on Artificial Neural Networks: Part III, pp. 92–101. Springer-Verlag, Berlin, Heidelberg (2010). http://dl.acm.org/citation.cfm?id=1886436.1886447
10. Kiranyaz S., Ince T., Gabbouj M., Real-time patient-specific ECG classification by 1-D convolutional neural networks. I.E.E.E. Trans. Biomed. Eng. **63**, 664–675 (2016). doi:10.1109/TBME.2015.2468589
11. Ince T., Kiranyaz S., Eren L., Askar M., Gabbouj M., Real-time motor fault detection by 1-D convolutional neural networks. IEEE Trans. Ind. Electron. **63**, 7067–7075 (2016). doi:10.1109/TIE.2016.2582729
12. Abdeljaber O., Younis A., Avci O., Catbas N., Gul M., Celik O., Zhang H.. Dynamic testing of a laboratory stadium structure. In: Geotechnical and Structural Engineering Congress, pp. 1719–1728 (2016). doi:10.1061/9780784479742.147

Chapter 7
Monitoring the Health of a Cantilever Beam Using Nonlinear Modal Tracking

Timothy A. Doughty, Alexandra K. Blaser, and Jacob R. Johnston

Abstract Cantilever beams can often be used as representative models for more complex systems and can accurately display the expected behavior of these systems under different loads. The health of a cantilever beam after being subjected to harmonic excitation at its second resonance frequency is determined using a nondestructive health monitoring technique. Nonlinear Modal Tracking assumes a second order differential equation that factors in mass, stiffness, and damping of the beam with a cubic nonlinearity parameter. Research so far has confirmed that a drastic shift in this nonlinear term is a result of crack initiation and an indicator of the beam's transition from healthy to unhealthy. Application of this Nonlinear Modal Tracking can be beneficial in monitoring the health of structures in order to predict catastrophic failure. The purpose of this study was to investigate several new techniques and conditions to verify the robustness of the model.

This experimental study included three newly considered beam geometries and then induced cracks using stress concentrations. Additionally, multiple frequency excitation was considered, and noise was added to the excitation frequency. This method of study is vital to future implementation of Nonlinear Modal Tracking in more complex systems. The technique successfully predicted the onset of beam failure during 5 of 6 beam experiments.

Keywords Nonlinear • Vibration • Health monitoring • Cantilever • Real-time

Nomenclature

Ω	Excitation Frequency
$\propto$	Nonlinear parameter
A	Vertical displacement
c	Damping
D_ξ	Bending stiffness
F	Input force
L	Length of total beam
m	Mass
NDE	Nondestructive evaluation technique
NMT	Nonlinear modal tracking
s	Horizontal displacement
t	Time

7.1 Introduction

In complex systems it is often very difficult to determine the current health and therefore the likelihood of detrimental failure. When a system is continuously in contact with oscillating loads, the system tends to fail through fatigue and crack propagation. The lifespan of some systems can be longer than several decades and it is extremely challenging to determine the current health and the remaining active life of these systems. Doing routine checks on the health of active systems can take quite a long time, cost a great deal, and cause delays in the activities and uses associated with these systems.

T.A. Doughty • A.K. Blaser • J.R. Johnston (✉)
University of Portland, 5000 N Willamette Blvd., Portland, OR 97203, USA
e-mail: doughty@up.edu; blaser18@up.edu; johnston17@up.edu

C. Niezrecki (ed.), *Structural Health Monitoring & Damage Detection, Volume 7*, Conference Proceedings of the Society for Experimental Mechanics Series, DOI 10.1007/978-3-319-54109-9_7

Table 7.1 Summary of previous using NDE and NMT research methods

Paper	Date	Type of test	Beam geometries and modifications	Frequency range
Loutridis [9]	2005	Instantaneous frequency (linear)	Unmodified	1st resonant frequency
Doughty [7]	2010	Nonlinear modal tracking	Unmodified	2nd resonant frequency
Doughty [13]	2016	Nonlinear modal tracking	Heat treated, weighted beams, asymmetric	2nd resonant frequency
This study	2016	Nonlinear modal tracking	Unmodified, tapered, parallel, induced stress concentrations	1st and 2nd resonantFrequency, noisy input Frequency, near-resonant frequencies

These constraints create a widespread need for a method of determining the health of these systems that also allows them to continue normal operations [1]. Research in the last few decades has yielded Nondestructive Evaluation Techniques (NDE) that provide useful information about the system without causing damage to that system [2–4]. This type of method may give significant warning to an expected failure when it recognizes crack initiation in a system. This technique could make routine checks on large systems obsolete as long as the health monitoring technique responds to the instigation of cracks or changes and alerts when maintenance is required. A robust method to recognize the growth of potentially catastrophic cracks and thereby predict and prevent failure would be very valuable. Millions of dollars could be saved in avoiding system health checks and lives could be saved by preventing failure.

This research is part of a progressive effort using the NDE technique known as Nonlinear Modal Tracking (NMT). This method has been proven successful at predicting the onset of failure for several test conditions [5–7]. The NMT method investigates the estimation of a nonlinear parameter in the equation of motion for a vibrating cantilever beam as a means to detect crack formation. This study expands the prior testing conditions to verify that the NMT method can predict the transition from healthy to unhealthy in a variety of systems. This work confirms that the NMT method can consistently detect changes in nonlinearity and report them prior to failure.

7.2 Background

Many of the current NDE methods detect crack initiation by tracking shifts in a system's natural frequency and using approximations based on linear parameters in the governing equations [8–12]. While these methods are popular and easier to implement, they often fail to recognize healthy nonlinear behavior that may be present in the system and then incorrectly diagnose the health of the system [7]. The NMT method can accurately assess the changes in a system's nonlinear behavior, and in turn, indicate the onset of failure. A summary of the NMT systems explored in prior work is shown in Table 7.1. For the purpose of this study, a cubic stiffness parameter was assumed to be used in the model. The cubic stiffness nonlinearity simplifies the model by absorbing the other system nonlinearities and will not misdiagnose the health of the system with small changes in the dynamics of the system [14].

In previous studies, the NMT method has been able to accurately predict the onset of failure without deriving a physically accurate model or the parameters associated with that model [13]. Other studies have shown that the model is successful when using minimal amounts of data, using a generic pre-collected data set, collecting data using strain gages instead of accelerometers, and testing various system geometries [5, 15]. Despite major changes in the system, the NMT model's resiliency points to its robustness and viability of real-world application.

7.3 Theoretical Model Development

For the purposes of this study, a cantilever beam is mounted horizontally and excited vertically at and near its second resonant frequency. This configuration is shown in Fig. 7.1.

In this theoretical model, several parameters are defined in the equations below. Mass is given by m, damping by c, bending stiffness by D_{ξ}, amplitude of vertical displacement by A, excitation frequency by Ω, time by t, horizontal displacement along the beam by s, and length of the total beam by L. The model for the transverse displacement of a cantilever beam with nonlinear bending stiffness is shown below [16]:

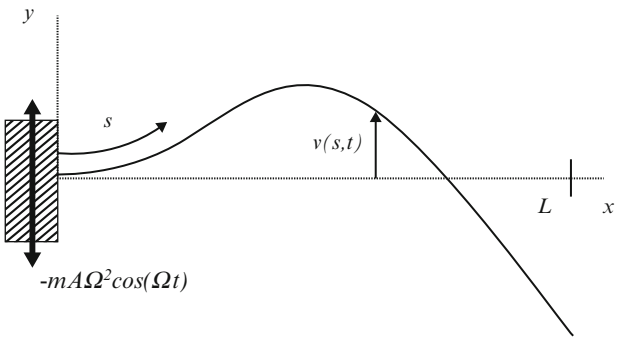

Fig. 7.1 Theoretical configuration for excited cantilever beam in second mode shape

$$m\ddot{v} + c\dot{v} + D_{\xi}\left\{v^{iv} + \left[v'\left(v'v''\right)'\right]'\right\} = -mA\Omega^2\cos\left(\Omega t\right), \tag{7.1}$$

$$v\left(0,t\right) = v'\left(0,t\right) = v''\left(L,t\right) = v'''\left(L,t\right) = 0. \tag{7.2}$$

Let ϕ(s) be the shape of the orthonormalized mode when the excitation is modal and the displacement spatially dependent given by:

$$\phi(s) = C\left[\sin\left(\boldsymbol{\beta}s\right) - \sinh\left(\beta s\right) - \Psi\left(\cos\left(\beta s\right) - \cosh\left(\beta s\right)\right)\right] \tag{7.3}$$

Where:

$$\Psi = \frac{\sin\left(\beta L\right) + \sinh\left(\beta s\right)}{\cos\left(\beta L\right) + \cosh\left(\beta L\right)} \tag{7.4}$$

Considering the second mode, [17] defines the following:

$$\beta L = 4.694. \tag{7.5}$$

Letting v(s,t) = α(t) •ϕ(s), then the nonlinear partial differential equation reduces to:

$$m\ddot{a} + c\dot{a} + ka + \propto a^3 = F(t) \tag{7.6}$$

Where:

$$k = \left\{D_{\xi}\int_0^L \phi\phi^{iv}ds\right\}, \tag{7.7}$$

$$\propto = \left\{D_{\xi}\int_0^L \phi\phi''^3 + 4\phi\phi'\phi''\phi''' + \phi\phi'^2\phi^{iv}ds\right\}, \tag{7.8}$$

And:

$$F(t) = -mA\Omega^2\cos\left(\Omega t\right) \bullet \int_0^L \phi ds. \tag{7.9}$$

The system's parameters can be estimated by collecting the input force, *F(t)*, and the measured response, *a(t)*, and the equation becomes a simple mass spring damping model. The nonlinear parameter $\propto$ then becomes the only unknown and is plotted with respect to time.

7.4 System Identification

The linear parameters of a mass spring damping model must be initialized to better estimate the nonlinear term. After the resonant frequency of a healthy cantilever beam is determined, response data is collected at six frequencies around resonance. The data collected assumes no nonlinearity due to the low response of excitation to the system, and the three linear terms m, k, and c, can be solved using a least-square regression.

Although it is expected that some of these parameters will fluctuate as time progresses during testing, these terms may lack physical meaning. For the purpose of this method, these values are required to solve for the nonlinear term.

Accelerometers are attached to the system to measure stimulus and response acceleration data, which is integrated to form a matrix of velocity and position vectors. These vectors are related to the forcing function through displacement, velocity, and acceleration by:

$$\left[\ddot{a}(t)\ \dot{a}(t)\ a(t)\ a(t)^3\right]\ [m\ c\ k\ \propto]^T = F(t), \tag{7.10}$$

Solving the equation for nonlinear term $\propto$ gives:

$$\propto = \{F(t) - m\ddot{a}(t) - c\dot{a}(t) - ka(t)\} \bullet \left\{a^3\right\}^T. \tag{7.11}$$

The nonlinear term is plotted with respect to time in MatLab using the above equation. Significant change in $\propto$ indicates the system's transition from healthy to unhealthy due to crack propagation, and therefore gives warning that predicts catastrophic failure.

7.5 Experimental Procedure

In this experiment, a 6061 Aluminum beam with dimensions 12.7 × 1.57 × 500 mm is clamped into a Vibration Exciter Type 4809 from B&K Instruments. The shaker receives a signal from a sinusoidal function generated from LabVIEW, which is then amplified using a B&K Power Amplifier Type 2706. Accelerometers are placed on the clamp (X) and 4.5 cm from the clamp on the beam (Y). The typical setup is shown in Fig. 7.2.

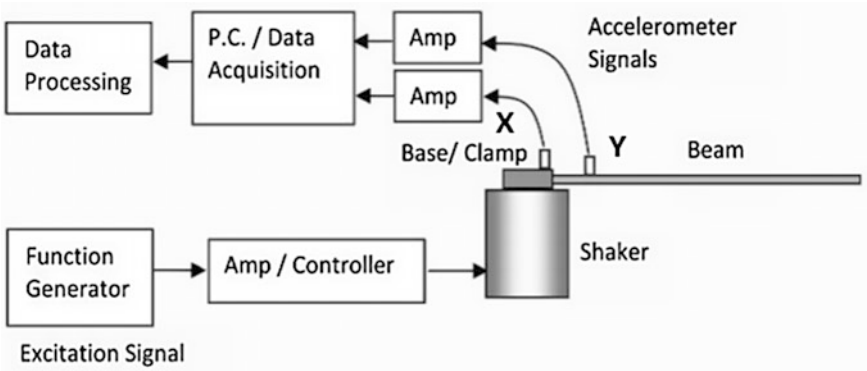

Fig. 7.2 System configuration

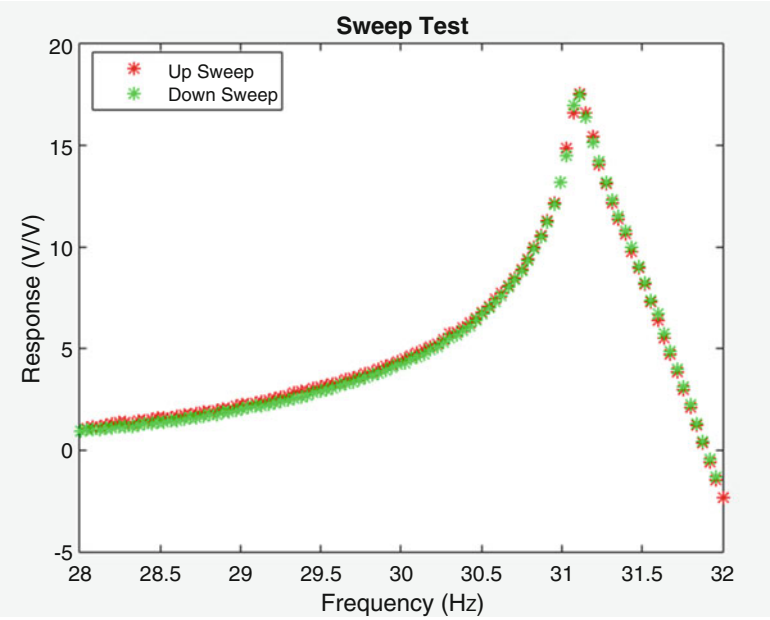

Fig. 7.3 Response of ratio of accelerometer data at a range of frequencies

X is read as the stimulus sinusoidal data and Y is read as the response sinusoidal data. During the Sweep, LabVIEW collects the acceleration data and plots the amplitude of the ratio of Y to X to determine resonant frequency. At the resonant frequency, the ratio of the Y to X is greatest in amplitude. Figure 7.3 shows a typical frequency vs response ratio from 28 Hz to 32 Hz.

The method of Steady State data collection has been proven to identify the linear parameters of the system [18]. At frequencies of ± 0.75, ± 1.25 and ± 2.0 Hz from the resonant frequency, acceleration data is collected by the accelerometers. This data is then input into MatLab and the linear terms are estimated using a least-squared method.

The beam is then set to vibrate at its second resonant frequency until it is broken. During this process, the acceleration data is collected from both accelerometers. Introduced in this study was the capability to plot the nonlinear term in near real-time. Immediately after the acceleration data is obtained, it is imported into MatLab for processing. Using Eq. (7.11), the nonlinear term is solved. The graph produced by MatLab updates the nonlinear term every two seconds creating a plot.

In order to determine the adaptability of the model to several real world applications, this method was tested on differing conditions. Varying beam geometry, addition of stress concentrations, excitation at multiple frequencies, and the implementation of noise to the stimulus were all considered during this investigation.

By implementing real-time analysis, monitoring the nonlinear parameter $\propto$ and noting significant changes can yield immediate results that indicate crack formation. This significant change has often occurred long before catastrophic failure. It is much more practical to use real-time analysis to determine the remaining health of the system.

7.6 Results

In order to check the robustness of the model, several different conditions were applied to the beams. Most systems are much more complicated than a single cantilever beam configuration, so there is a desire to test more intricate systems. Two beams were connected in parallel 26 mm apart by a link made of the same material through the process of welding. The link was placed 4.5 cm from the clamp and the accelerometer was placed directly on the link segment. The results of this test are shown in Fig. 7.4.

For the second beam geometry, the beam was tapered asymmetrically. At the clamp, the beam was left at a width of 12.7 mm and the end width was 2 mm with only one side being machined. As seen in Fig. 7.5, the significant change in alpha is apparent at minute 400 with a break around minute 480.

To create a stress concentration in the beam, a hole with a diameter of 6 mm was drilled at 38 mm from the clamp. Since the diameter of the hole is half the original width of the beam, the nominal stress is theoretically twice that of a regular beam

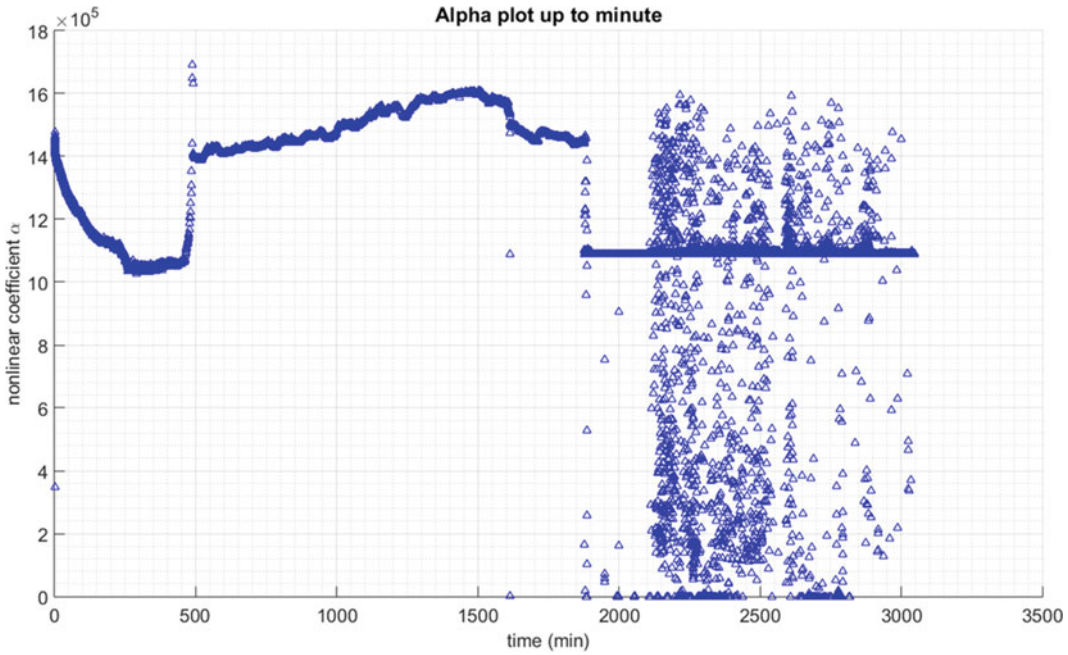

Fig. 7.4 Parallel beam configuration alpha plot

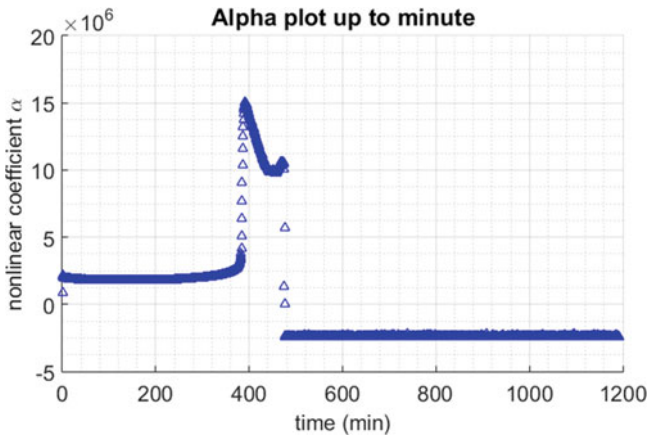

Fig. 7.5 Alpha plot for asymmetric tapered beam

at the same point. The force has remained the same but the cross-sectional area has decreased by half, meaning the stress must be doubled. The plot of Alpha is shown below in Fig. 7.6 with a significant increase around minute 275, just before the break.

In order to excite the beam at multiple frequencies, several sinusoidal inputs were added. Once the Sweep test confirmed values for the second resonance frequency, sine waves were added at frequencies of ± 0.5 Hz from resonance. This resulted in a beat or pulse that can be represented by the Fig. 7.7 below.

For these multi-frequency beams Fig. 7.8 alpha plot shows a beam with a resonant frequency of 32.07 Hz added to near-resonance frequencies 32.57 Hz and 31.57 Hz, both at an amplitude of 0.15. The significant change in alpha occurs around minute 275 with an abrupt spike from its downward trend. Figure 7.9 alpha plot shows a beam with a resonant frequency of 31.27 Hz added to near-resonant frequencies of 31.77 Hz and 30.77 Hz. This plot shows a significant change in alpha at around 1200 minutes with a break occurring at 1300 minutes.

Another test that was conducted during this study was a combination of the first and second mode resonances. A sweep test was conducted to identify both the first and second resonant frequencies. Once both were obtained, the first resonant frequency with a small amplitude was added to the second resonant frequency. This resulted in a visual of both first and second mode oscillations. These two modes can be seen in Fig. 7.10. A plot of the alpha value is shown in Fig. 7.11.

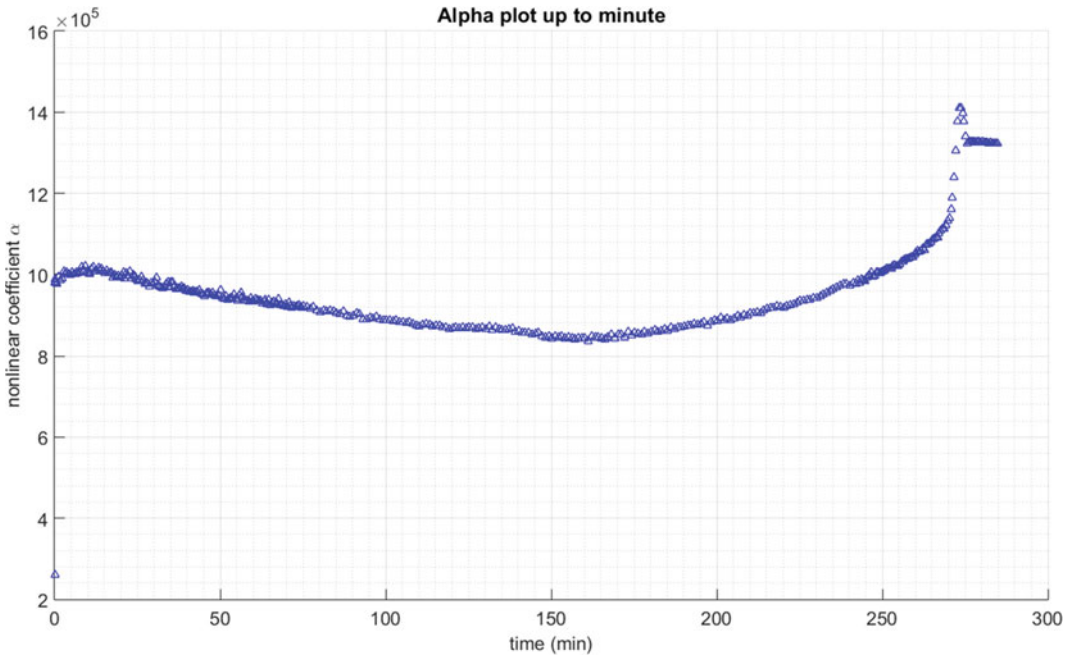

Fig. 7.6 Alpha plot for stress concentration beam

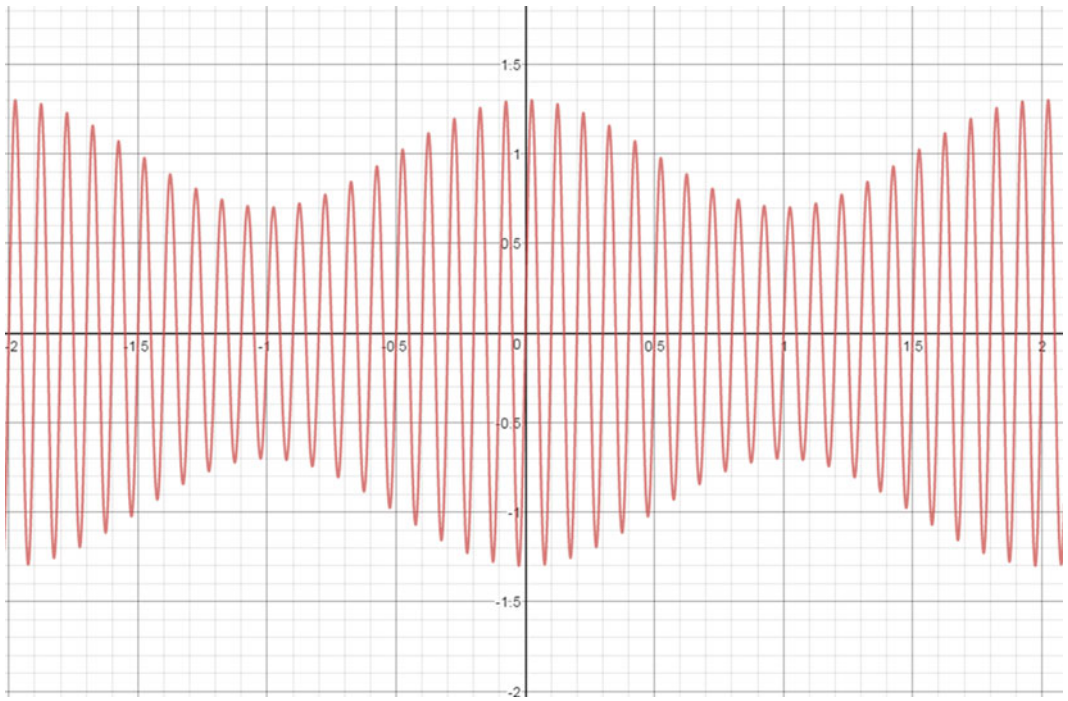

Fig. 7.7 Sinusoidal beat with resonance frequency 10 Hz

This plot displays a significant increase in alpha at minute 1400, when the crack growth initiated. The beam breaks at the peak of this increase at minute 1600 and alpha remains at a constant, confirming the beam has broken. While the value of alpha does gradually change and fluctuate, this can be attributed to irregularities in the beam or subtle shifts in beam stiffness. The large changes, however, are a direct result of crack formation and therefore crucial to note.

One last test that was conducted was the addition of noise to the input signal. This was to mimic the real world conditions which will not provide noise-free excitations to the system. The biggest struggle was determining how to simulate a noisy

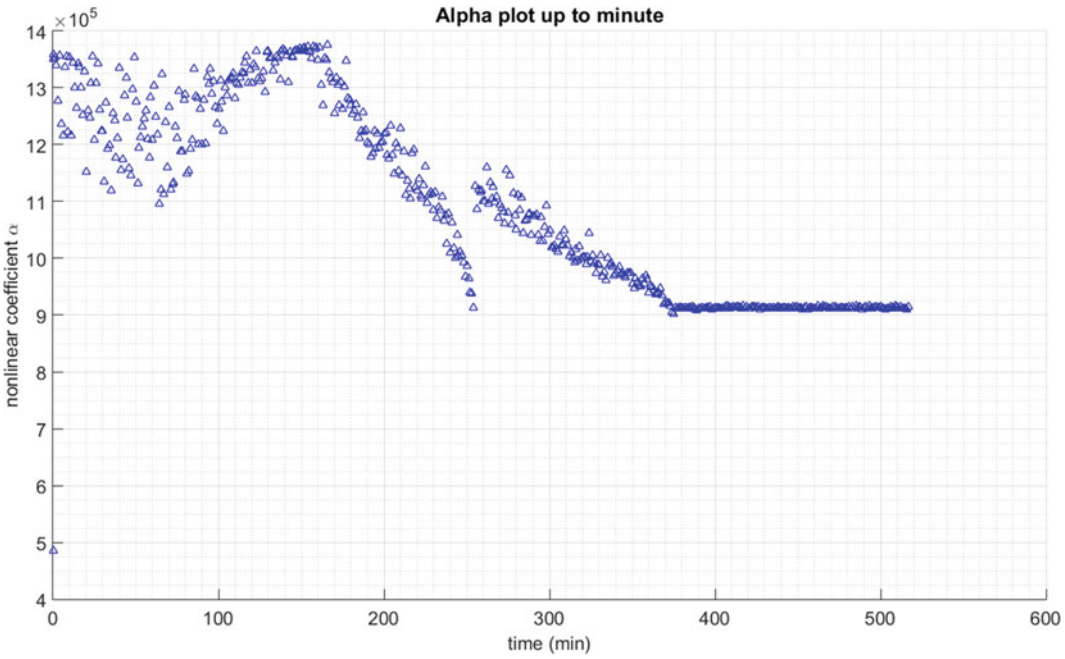

Fig. 7.8 Near-resonant frequency excitation alpha plot at 32.07 Hz

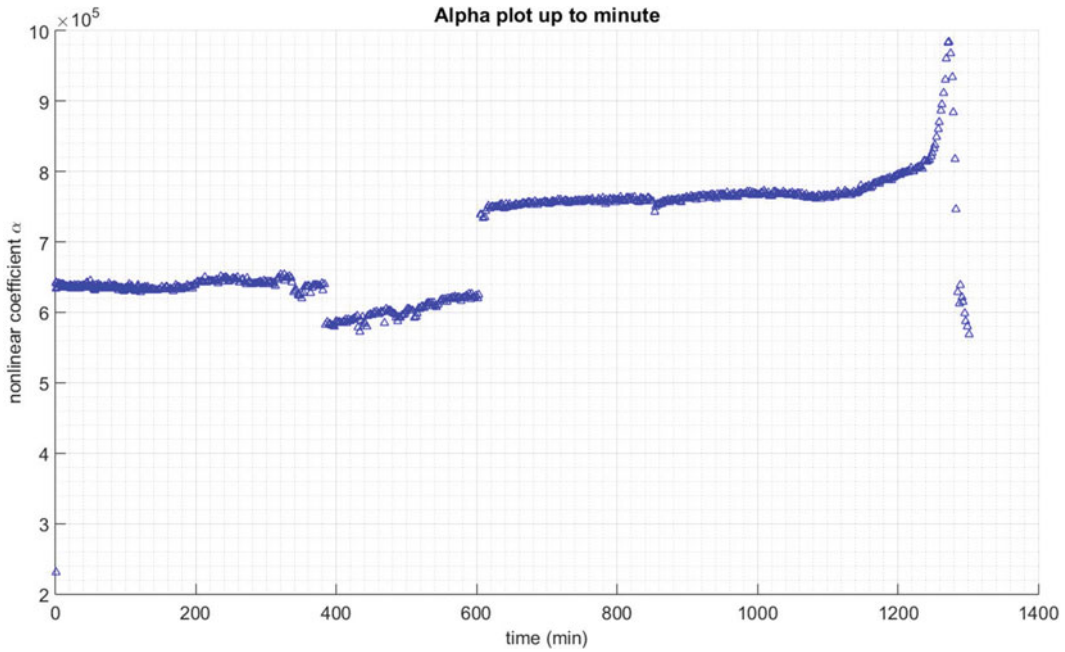

Fig. 7.9 Near-resonant frequency excitation alpha plot at 31.27 Hz

signal and input it to the shaker. In the end, a sinusoid with a random and varying amplitude was added to the resonant frequency to simulate noise. As shown in the alpha plot for this test in Fig. 7.12 below, a significant change in alpha can be seen in several places. The most notable change occurs at minute 3000, with the break occurring at roughly 4200 minutes.

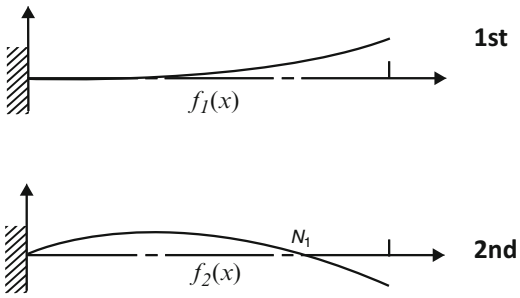

Fig. 7.10 Diagram of first and second mode shapes

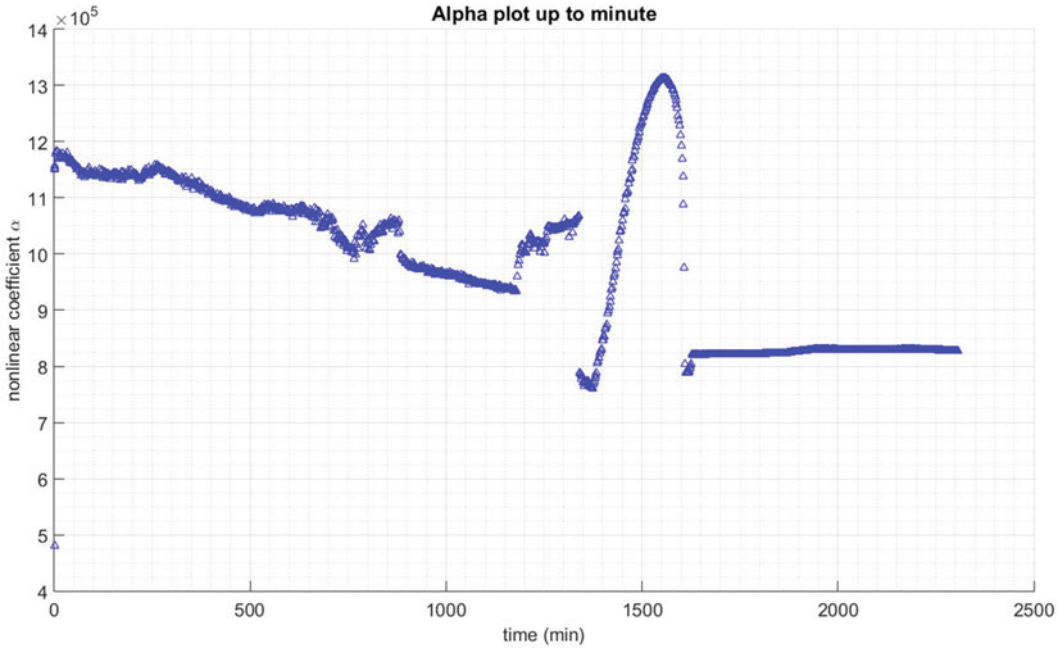

Fig. 7.11 Alpha plot of beam set to first and second mode

7.7 Discussion

For the parallel beam configuration, the alpha plot showed early indication of failure, roughly 500 minutes into the break stage. At 1900 minutes graph showed catastrophic failure. The use of NMT proved successful by indicating imminent failure at approximately 26% of total life of the beam. Although static is apparent in the plot, the constant nature of alpha during this period shows that the beam had been broken.

Through the use of real-time analysis, physical changes were noted in the amplitude of the beam's response at the same time that significant changes in alpha were found around minute 500 of testing. The ability to monitor the plot of the nonlinear term despite being unable to physically inspect the system while it is in use makes determining system health much more manageable and much less expensive.

The alpha plot for the tapered beam in Fig. 7.5 shows a clear transition from healthy to unhealthy, and from unhealthy to catastrophic failure. This is proof that the Nonlinear Modal Tracking method of health monitoring gives a distinct indication of break prior to failure even when the beam geometry has been altered in this fashion. The indication of unhealthy behavior occurs at roughly 83% of the beam's total lifespan, giving sufficient warning of the system's break.

Stress concentrations can often be found in many real world systems and therefore are crucial to be tested in this study. As seen in Fig. 7.6, the alpha plot remained relatively constant throughout the break stage until the last ten minutes of the beam's life. The indication of unhealthy behavior occurred 97% into the beam's life. Ideally, this significant change should occur well before the failure of the system so as to offer time to take action concerning the system's health.

Systems in use are often not excited at a single frequency. These systems undergo pulses or beats as a direct result of multiple frequencies whose values are similar. This can result in a vastly different response from the system. As seen in Fig. 7.8, this resulted in a very noisy plot of the alpha value, but ultimately responded positively to the NMT method with a

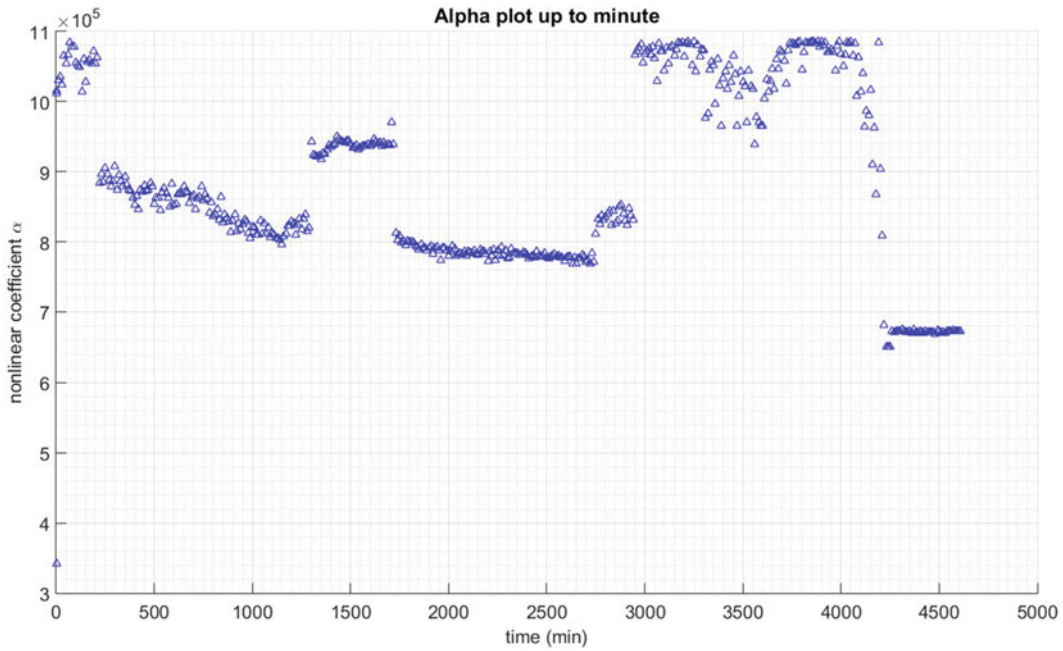

Fig. 7.12 Alpha plot for beam with noise addition

significant change in the trend of alpha 68% into its total life. In Fig. 7.9, the irregularity in the jump in alpha around minute 600 is a direct result of an error in the data collecting hardware. The significant change of alpha at 1200 minutes, however, does indicate a transition from healthy to unhealthy at roughly 92% of the total life of the beam.

All physical objects have infinite resonant frequencies and some of them may become excited at the same time. In order to test this likely phenomenon, the first and second resonant frequencies were added and input to the system. Figure 7.11 shows a significant change in alpha at minute 1400 and the beam breaks at 1600 minutes. The indication of the transition occurs at 87% of the total life of the beam.

Previous studies have looked into the use of NMT with noise added to the data post collection. In this study, noise added was added to the input signal in order to determine the effects that noise has on the system during testing. As seen in Fig. 7.12, this resulted in unpredictable changes in alpha. Each significant change in alpha over the course of the test is a result of some nonlinear change in the system, the greatest of which occurring around the minute 3000. This shows indication of transitioning from healthy to unhealthy at 70% of the life of the beam. This shows that without perfect conditions of frequency excitation, the NMT method is still valid in determining failure.

7.8 Conclusion

This study introduced the NMT method in order to predict failure in an oscillating cantilever beam. In order to do this, the nonlinear parameter alpha was plotted over the time of this oscillation and several new testing conditions were implemented. This was in hope of determining if the transition from healthy to unhealthy could be recognized prior to the break.

This study concludes that the use of NMT is effective in determining the health in systems with varying geometries, multiple frequency excitation, and input noise through the use of a nondestructive technique. While this method was also accurate in determining the health of a beam subject to stress concentrations, the crack indication on the alpha plot appeared significantly late in the life of the beam. It is recommended that further study be completed in order to verify the robustness of this model in determining beam health under this condition.

The use of real-time analysis and alpha tracking further enhanced the ability to analyze the health of the system. For most of the conditions tested during this study, the plots gave significant warning of failure once crack initiation began. Systems would benefit from being monitored continuously in the real world; this real world application would be irrelevant if the nonlinear parameter could not be monitored in real-time.

The NMT method has shown real prospect for future use in monitoring the health of more complicated systems. With further study, this method could be viable in determining the health of systems such as bridges and airplanes. Implementing this method could very much reduce unnecessary maintenance costs or give warning that a system needs to be shut down before failure. Future research should investigate possible reasons for the smaller changes in alpha that occur due to fluctuation of the linear nature of the system.

References

1. Doebling, S.W., Farrar, C.R., Prime, M.B.: A summary review of vibration-based damage identification methods. Shock Vib. Dig. **30**, 91 (1998)
2. Bovsunovsky, A.P., Bovsunovsky, O.: Crack detection in beams by means of the driving force parameters variation at non-linear resonance vibrations. Key Eng. Mater. **347**, 413–420 (2007)
3. Andreaus, U., Casini, P., Vestroni, F.: Nonlinear features in the dynamic response of a cracked beam under harmonic forcing. In: 5th International Conference on Multibody Systems, Nonlinear Dynamics, and Control, Parts A, B, and C, vol. 6, pp. 2083–2089. ASME, Long Beach, CA (2005)
4. Doughty, T.A., Leineweber, M.J.: Investigating nonlinear models for health monitoring in vibrating structures. Mech. Solids, Struct. Fluids. **11**, 57–62 (2009)
5. Doughty, T.A., Dally, M.R., Bacon, M.R., Etzel, N.G.: Nonlinear Model Tracking for Varying System Geometries, pp. 167–175. Springer, New York (2013)
6. Doughty, T.A., Higgins, N.S., Etzel, N.G.: Nonlinear model tracking in application to failed nondestructive evaluations. Mech. Solids, Struct. Fluids; Vib., Acoust. Wave Propag. **8**, 1009–1016 (2011)
7. Doughty, T.A.: Effect of nonlinear parametric model accuracy in crack prediction and detection. In: Experimental and Applied Mechanics, vol. 6, pp. 549–556. Springer, New York (2010)
8. Khiem, N.T., Lien, T.V.: Multi-crack detection for beam by the natural frequencies. J. Sound Vib. **273**(1), 175–184 (2004)
9. Loutridis, S., Douka, E., Hadjileontiadis, L.J.: Forced vibration behaviour and crack detection of cracked beams using instantaneous frequency. NDT E Int. **38**(5), 411–419 (2005)
10. Lee, Y.Y., Liew, K.M.: Detection of damage locations in a beam using the wavelet analysis. Int. J. Struct. Stab. Dyn. **1**(3), 455–465 (2001)
11. Gudmundson, P.: Changes in modal parameters resulting from small cracks. Proc. Int. Modal Anal. Conf. Exhib. **2**, 690–697 (1984)
12. Kim, J.-T., Ryu, Y.-S., Cho, H.-M., Stubbs, N.: Damage identification in beam-type structures: frequency-based method vs mode-shape-based method. Eng. Struct. **25**(1), 57–67 (2003)
13. Doughty, T.A., Belle-Isle, A.W., Pendowski, N.: Experimental validation of nonlinear model tracking with varying conditions. In: Topics in Modal Analysis and Testing, vol. 10, pp. 139–153. Springer International Publishing, New York (2016)
14. Doughty, T.A., Davies, P., Bajaj, A.K.: A comparison of three techniques using steady state data to identify non-linear modal behavior of an externally excited cantilever beam. J. Sound Vib. **249**(4), 785–813 (2002)
15. Doughty, T.A., Hector, M.J.: Numerical enhancement of nonlinear model tracking for health monitoring. In: Dynamics of Civil Structures, vol. 2, pp. 191–199. Springer International Publishing, New York (2015)
16. Crespo da Silva, M.R.M., Glynn, C.C.: Nonlinear flexural-flexural-torsional dynamics of inextensional beams. II. Forced motions. J. Struct. Mech. **6**(4), 449–461 (1978)
17. Benaroya, H., Nagurka, M.L.: Mechanical Vibration: Analysis, Uncertainties, and Control. CRC/Taylor & Francis, Boca Raton, FL (2010)
18. Doughty, T.A.: System identification of modes in nonlinear structures. Ph.D. Thesis, Ray W. Herrick Laboratories, School of Mechanical Engineering, Purdue University (2002)

Chapter 8
Using Modal Parameters for Structural Health Monitoring

Shawn Richardson, Jason Tyler, Brian Schwarz, Patrick McHargue, and Mark Richardson

Abstract In two recent papers, we introduced the idea of numerically comparing currently acquired operating data with archived data to identify faults in rotating machinery (Ganeriwala et al.: Using operating deflection shapes to detect unbalance in rotating equipment. In: IMAC XXVII. Orlando, FL (2009); Richardson et al.: Using operating data to locate and quantify unbalance in rotating machinery. In: IMAC XXXIV, January 25–28, 2016). We introduced a new metric for comparing two operating deflection shapes called the *Shape Difference Indicator (SDI)*. In another previous paper (Richardson et al.: A new measure of shape difference. In: IMAC XXXII, February 3–6, 2014), we used SDI to measure the difference in modal frequencies from before and after a stiffness change was made to a mechanical structure.

In this paper we provide more details of how experimental modal frequency and damping parameters can be used together with the SDI metric as a means of detecting and quantifying changes in the physical properties of a structure.

Also, we have implemented SDI together with a search method for ranking the differences between currently acquired modal parameters and archived modal parameters. We call this new method Fault Correlation Tools (FaCTs™). FaCTs™ can be used in multiple applications, including structural health monitoring, production qualification testing, and recertification of machinery in field maintenance applications.

Keywords Fourier spectrum • Auto power spectrum • Cross power spectrum • Frequency response function • Experimental mode shape • Operational mode shape • Modal assurance criterion • Shape difference indicator

8.1 Introduction

It is well known that any change in a physical property of a mechanical structure (e.g. its mass, stiffness, or damping) has a direct effect on its resonant vibration. If the stiffness of a structure is increased, its resonant frequencies will increase. Likewise, if its stiffness is decreased, its resonant frequencies will decrease. Alternatively, if the mass of a structure increases, its resonant frequencies will decrease [1, 2]. If the mass decreases, its resonant frequencies will increase. If the damping forces applied to a structure are increased, the damping of its resonances will increase [3].

Each resonance is mathematically characterized by its three modal parameters (natural frequency, modal damping, and mode shape).

Modal parameters can be extracted from acquired vibration data using a wide variety of sensors and instrumentation, under a wide variety of operating conditions.

In this paper we show how experimental modal frequency and damping can be used together with the SDI metric as a means of detecting and quantifying changes in structural stiffness. SDI is similar to the Modal Assurance Criterion (MAC), which provides a numerical comparison between two mode shapes [4, 5]. Like MAC, SDI is a *correlation coefficient* with values that range between 0 and 1. A value of 1 indicates no difference between two shapes. A value less than 1 indicates that two shapes are different.

The SDI metric has been implemented together with a search algorithm to correlate currently acquired modal parameters with parameters stored in an archival data base. We call this new search method Fault Correlation Tools (FaCTs™). The result of each database search is a display of the **Top Ten FaCTs™ bars** (highest SDI values) between the current modal parameters and modal parameters stored in the database.

S. Richardson • J. Tyler • B. Schwarz • P. McHargue • M. Richardson (✉)
Vibrant Technology, Inc., Centennial, CO 80112, USA
e-mail: mark.richardson@vibetech.com

C. Niezrecki (ed.), *Structural Health Monitoring & Damage Detection, Volume 7*, Conference Proceedings of the Society for Experimental Mechanics Series, DOI 10.1007/978-3-319-54109-9_8

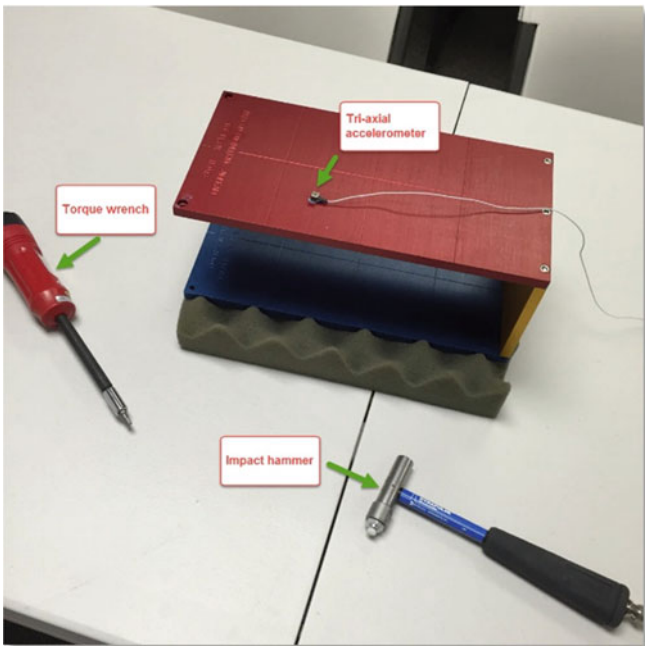

Fig. 8.1 Jim beam test structure

FaCTs™ can be used in several ways.

1. To indicate *slowly occurring changes* in the modal properties of a machine or structure from monitored data
2. To *identify specific mechanical faults* which have been associated with certain modal parameters archived in a **database**
3. *In qualification testing were the experimental modal parameters of each test article are used to determine its pass-fail* condition

In this paper, we will revisit the use of FaCTs™ to identify the torque used to tighten one of the cap screws of the Jim Beam structure shown in Fig. 8.1 [3]. It will be shown that FaCTs™ can *uniquely identify* the amount of torque applied to the cap screw from among five different test results.

The Jim Beam was impacted with the instrumented hammer shown in Fig. 8.1. Three FRFs were calculated between the acquired impact force and the tri-axial accelerometer response signals. The locations of the impact force and the accelerometer are not critical. However, if their locations are chosen closer to the anti-node (large mode shape amplitude) of a mode, any physical change will potentially have more influence on that mode.

After impacting the structure, the resulting FRFs were curve fit to extract the frequency and damping of six modes. The number of modes used is also not critical, but higher frequency modes will typically be more sensitive to physical changes.

When multiple modal frequencies are used, they are stored as a "shape". In this use, the term "shape" simply means that two or more modal frequencies are stored and treated mathematically like a vector. MAC correlates two mode shapes [4, 5]. SDI was developed for the same purpose; to correlate two shape vectors of data.

It will be shown that FaCTs™ can identify each of the five different test cases by comparing the modal frequencies acquired from each impact test with archived frequencies associated with a specific amount of torque applied to the cap screw.

Before discussing the test results, the Modal Assurance Criterion (MAC) and the Shape Difference Indicator (SDI) will be reviewed to point out their differences. It will then be shown that by increasing its sensitivity, SDI can be used as a reliable metric for uniquely identifying modal frequencies associated with specific joint stiffnesses.

8.2 Review of Modal Assurance Criterion (MAC)

You might be wondering, *if MAC is used for numerically correlating two shapes, why introduce another correlation method?* SDI was developed to overcome two limitations of MAC, namely,

1. MAC only indicates the *co-linearity* of two shapes
   MAC = 1 if two shapes lie on the same straight line
2. MAC cannot measure the difference between two numbers MAC = 1 if two shapes only have one component

MAC is defined with the formula,

$$\mathrm{MAC} = \frac{\left\| \{A\}^h \{B\} \right\|^2}{\{A\}^h \{A\} \{B\}^h \{B\}} \tag{8.1}$$

{A} = shape A (complex m-vector)
{B} = shape B (complex m-vector)
m = number of matching DOFs between the shapes
h–denotes the transposed conjugate vector

Figure 8.2 depicts two possible cases for MAC values. If two shapes lie on the same straight line, then **MAC = 1**. If two shapes do not lie on the same straight line, then **MAC < 1**.

MAC cannot answer the question, "If two shapes lie on the same straight line, are they different from one another?" To answer that question, a measure of the *difference* between two shapes was developed [3].

Fig. 8.2 MAC cases

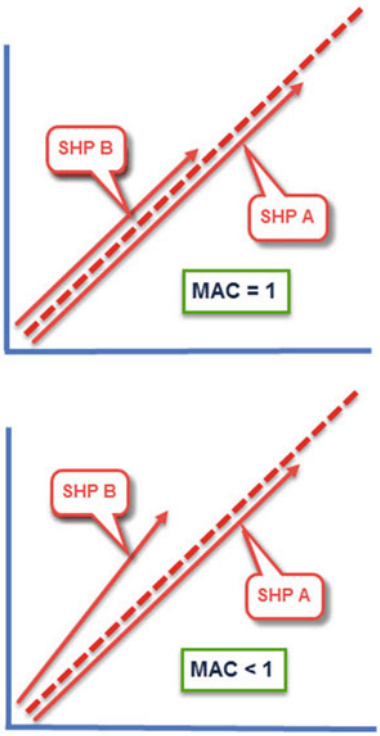

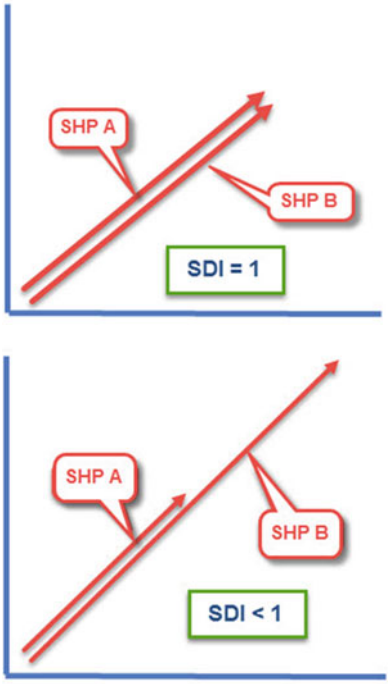

Fig. 8.3 SDI cases

8.3 Review of Shape Difference Indicator (SDI)

The shape difference indicator is defined with the formula,

$$\mathrm{SDI} = \left(1 - \frac{\|\{A\} - \{B\}\|^2}{\{A\}^h \{A\} + \{B\}^h \{B\}}\right)^2 \tag{8.2}$$

or

$$\mathrm{SDI} = \left(\frac{2\, real\left(\{A\}^h \{B\}\right)}{\{A\}^h \{A\} + \{B\}^h \{B\}}\right)^2 \tag{8.3}$$

real = real part of the shape product

SDI values also range between **0 and 1**. If two shapes have *identical shape components*, **SDI = 1**. If two shapes have *different shape components*, **SDI < 1**. Several examples illustrate typical SDI values.

- If {A} = {B}, SDI = 1
- If {A} = {0} *or* {B} = {0}, SDI = 0
- If {A} = 2{B}, SDI = 0.64
- If {A} = 10{B}, SDI = 0.04

8.4 Identifying Cap Screw Torque

SDI can be used to detect differences between two shapes, no matter what type of data they contain. To illustrate this, different amounts of torque where applied to one of the Allen screws that attach the top plate to the back plate of the Jim Beam, shown in Fig. 8.4.

Six different torque values were applied to the Allen screw on the Jim Beam;

Case 1: 10 in-lbs.

Case 2: 15 in-lbs.

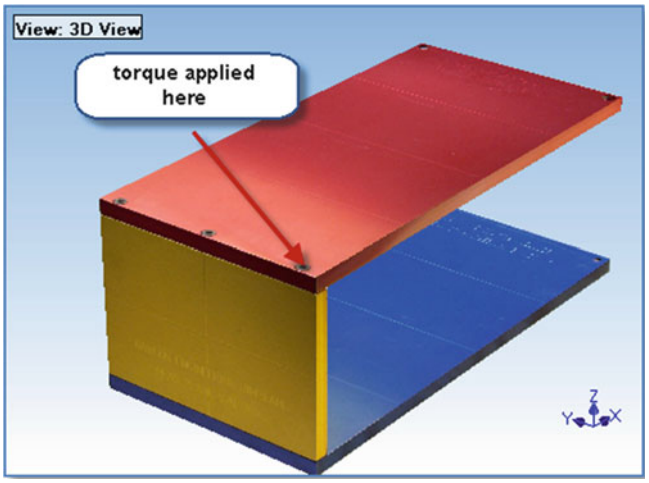

Fig. 8.4 Torque applied to Allen screw

SHP: All Frequencies

Select Shape	Frequency (or Time)	Damping	Units	Damping (%)	Label
1	0	0	Hz	0	10 IN-LBs
2	0	0	Hz	0	15 IN-LBs
3	0	0	Hz	0	20 IN-LBs
4	0	0	Hz	0	25 IN-LBs
5	0	0	Hz	0	30 IN-LBs
6	0	0	Hz	0	35 IN-LBs

Modal frequencies stored as shapes

Select M#	Shape 1 Magnitude	Shape 2 Magnitude	Shape 3 Magnitude	Shape 4 Magnitude	Shape 5 Magnitude	Shape 6 Magnitude
M#1	155.4	155.5	156.1	156.3	156.5	156.3
M#2	189.2	190.4	191.2	191.7	192.1	192.4
M#3	341.2	341.6	342	342.2	342.4	342.4
M#4	429.2	430.1	430.8	431.2	431.6	431.8
M#5	481.8	482.6	483.3	483.8	484.2	484.4
M#6	562.7	564.6	565.7	566.5	567.1	567.7

Fig. 8.5 Modal frequency shapes

Case 3: 20 in-lbs.
Case 4: 25 in-lbs.
Case 5: 30 in-lbs.
Case 6: 35 in-lbs.

The Jim Beam was impact tested after each of the 6 torques was applied to the Allen screw. For each case, three FRFs were calculated (between the force and the three acceleration responses), and the FRFs were curve fit to extract the modal frequency and damping of six modes.

The frequency and damping of six modes of the Jim Beam were stored as shape components in two shape tables. The "modal frequency shapes" are listed in Fig. 8.5, and the "modal damping shapes" are listed in Fig. 8.6.

The expected result regarding modal frequency is in evidence by examining each row of modal frequencies in Fig. 8.5. As the screw torque was increased (from Shape 1 to Shape 6) the modal frequencies of all six modes increased compared to the previous case.

A (perhaps unexpected) result occurred with the modal damping values, however. By examining each row of modal damping values in Fig. 8.6, the damping of the structure was not significantly affected by changes in the torque applied to the Allen screw. The modal damping values in each row *did not change significantly* from one shape to the next one.

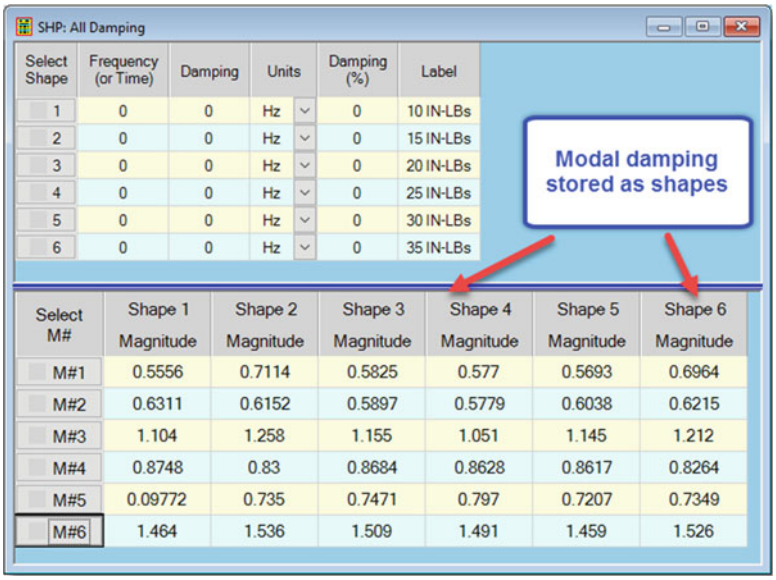

Select Shape	Frequency (or Time)	Damping	Units	Damping (%)	Label
1	0	0	Hz	0	10 IN-LBs
2	0	0	Hz	0	15 IN-LBs
3	0	0	Hz	0	20 IN-LBs
4	0	0	Hz	0	25 IN-LBs
5	0	0	Hz	0	30 IN-LBs
6	0	0	Hz	0	35 IN-LBs

Select M#	Shape 1 Magnitude	Shape 2 Magnitude	Shape 3 Magnitude	Shape 4 Magnitude	Shape 5 Magnitude	Shape 6 Magnitude
M#1	0.5556	0.7114	0.5825	0.577	0.5693	0.6964
M#2	0.6311	0.6152	0.5897	0.5779	0.6038	0.6215
M#3	1.104	1.258	1.155	1.051	1.145	1.212
M#4	0.8748	0.83	0.8684	0.8628	0.8617	0.8264
M#5	0.09772	0.735	0.7471	0.797	0.7207	0.7349
M#6	1.464	1.536	1.509	1.491	1.459	1.526

Fig. 8.6 Modal damping shapes

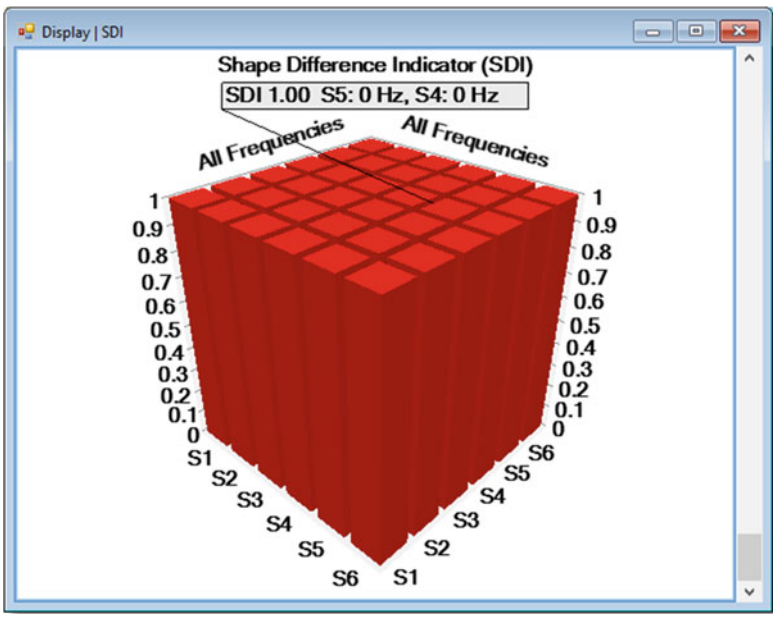

Fig. 8.7 SDI values of modal frequency shapes

8.5 SDI and MAC with Modal Frequency Shapes

The bar chart in Fig. 8.7 is the SDI values for all pairs of modal frequency shapes in Fig. 8.5. Each *diagonal bar* is the SDI value for a case with itself, which has the expected value of 1. Each *off-diagonal bar* is the SDI value for a pair of dissimilar stiffness cases.

OFF-DIAGONAL PROPERTY: If an *off-diagonal* bar is *less than 0.9* in a chart of bars between different pairs of shapes, the SDI (or MAC) metric can be used to *uniquely distinguish* between the two cases associated with the shapes.

The desired off-diagonal property *is not exhibited* in the SDI bar chart in Fig. 8.7, nor in the MAC bar chart in Fig. 8.8. Both bar charts show that *neither SDI nor MAC could be used as a metric* for distinguishing between the modal frequencies for the five stiffness cases.

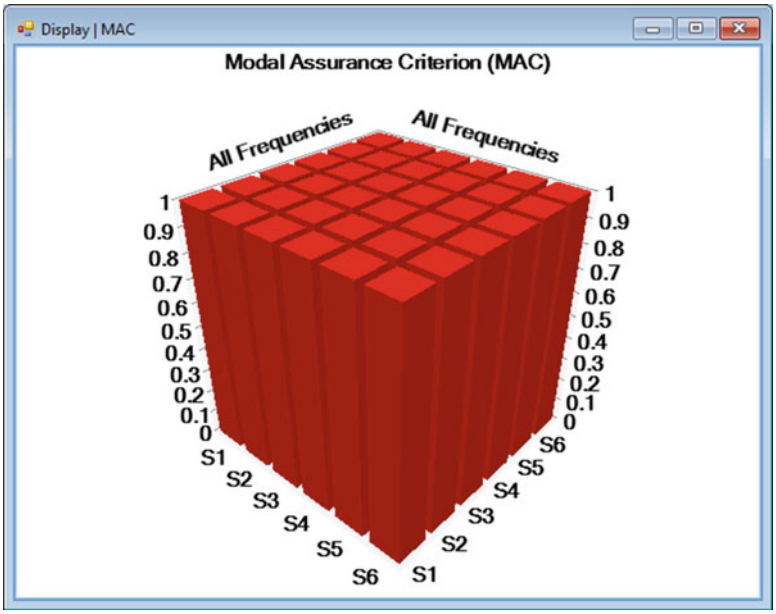

Fig. 8.8 MAC values of modal frequency shapes

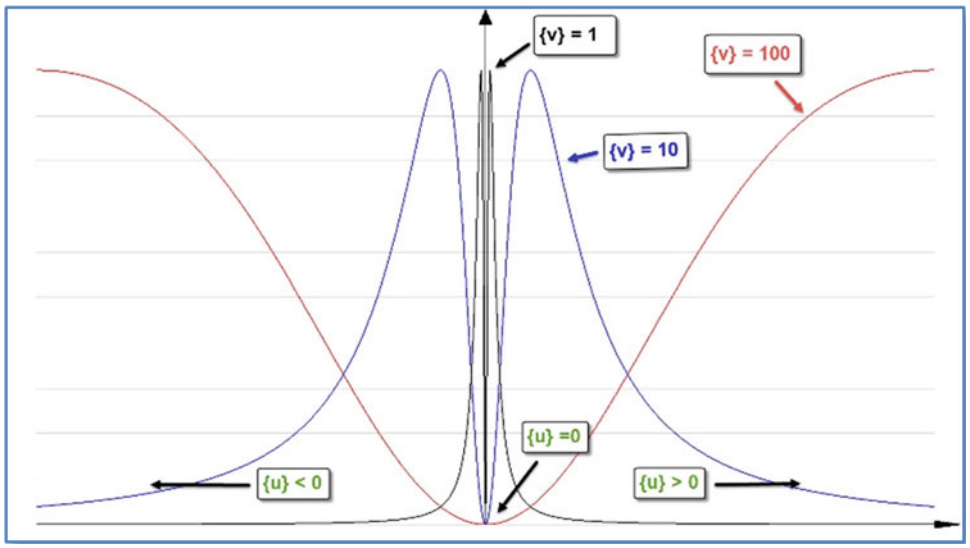

Fig. 8.9 SDI curves for {u} and {v}

However, a *unique characteristic* of the SDI metric can be exploited to increase its sensitivity. With increased sensitivity, SDI can be used to distinguish the difference between all pairs of frequency shapes in Fig. 8.5.

8.6 Increased SDI Sensitivity

Figure 8.9 is a plot of three SDI curves for different values of two shapes {u} and {v}. In general, {u} and {v} are vectors, but in this case each vector only has a real component. Three curves are plotted for the shape $\{v\} = 1, 10, 100$.

These SDI curves have two unique properties,

1. When $\{u\} = 0$, SDI $= 0$
2. The SDI curve *flattens out* for large values of {v}, and *sharpens up* for small values of {v}

Another way of interpreting the curves in Fig. 8.9 is that *SDI is more sensitive to shape differences when the shape values are smaller*.

All of the frequency shape values in Fig. 8.5 are above 100, so the SDI values in Fig. 8.7 when calculated using a *very flat SDI surface*. For shapes with multiple components (**m > 1**), SDI is a surface instead of a line like that in Fig. 8.9. Hence the SDI bars in Fig. 8.7 are not a very sensitive measure of the shape differences.

However, the curves in Fig. 8.9 show that the sensitivity of SDI can be increased if the vectors {u} and {v} are replaced with the following new vectors, which are both closer to the origin of the SDI surface.

{v} = {small number} where (small number > 0)

{u} = {v} + ({u} – {v})

Replacing {u} and {v} with {u} and {v}, where {v} contains small numbers, moves the peak in the SDI surface closer to the origin where it *makes faster transitions between 0 and 1*. This makes the SDI calculation more sensitive to the difference between {u} and {v}.

8.7 Modal Frequency Shapes with Increased Sensitivity

Figures 8.10, 8.11, and 8.12 contain SDI bar charts of the modal frequency shapes for the six stiffness cases, but with increased sensitivities using *small numbers = 0.5, 0.125, and 0.01*.

Clearly, increasing the sensitivity of SDI turned it into a useful metric for *uniquely identifying all six torque cases*. An off-diagonal SDI value *less than 0.90* makes it useful for distinguishing one stiffness case from another.

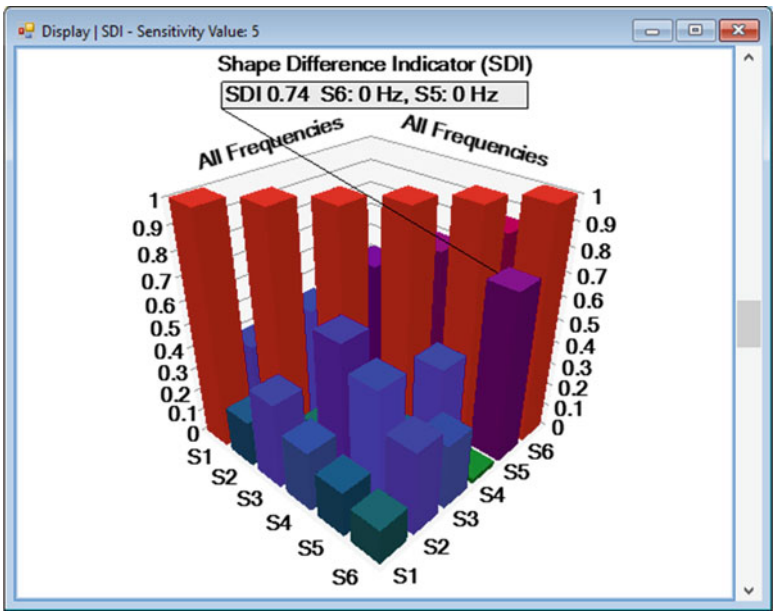

Fig. 8.10 SDI for frequency shapes (Sensitivity = 0.5)

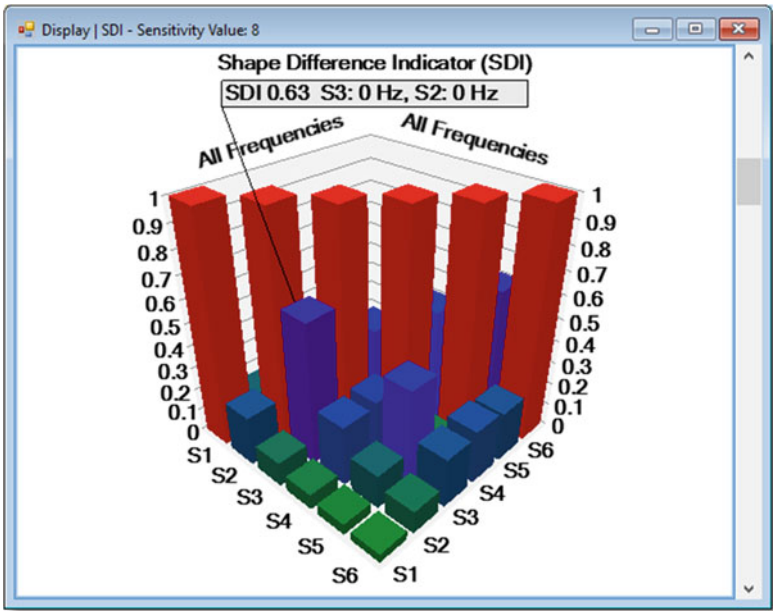

Fig. 8.11 SDI for frequency shapes (Sensitivity = 0.125)

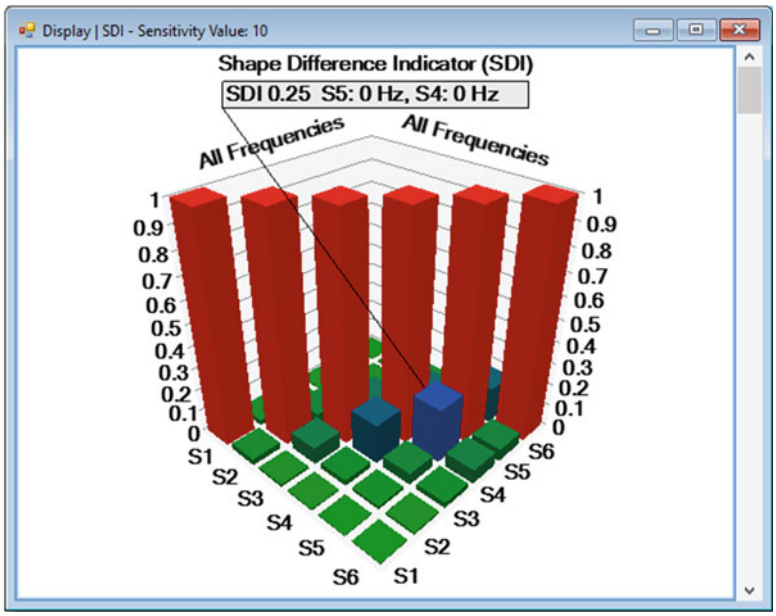

Fig. 8.12 SDI for Frequency Shapes (Sensitivity = 0.01)

8.8 Modal Damping Shapes with Increased Sensitivity

Figures 8.13 and 8.14 contain SDI bar charts of the modal damping shapes for the five stiffness cases. No sensitivity was used in Fig. 8.13, and a *sensitivity of 0.01* was used in Fig. 8.14.

Even with a high sensitivity, some of the SDI bars in Fig. 8.14 have values *higher than 0.9*. This means that those pairs of stiffness cases are *not distinguishable* from one another.

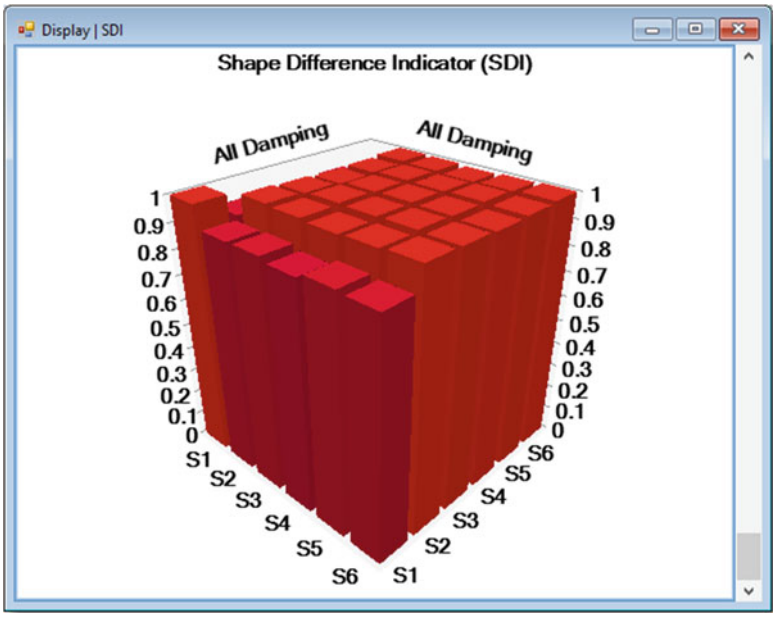

Fig. 8.13 SDI for damping shapes (no Sensitivity)

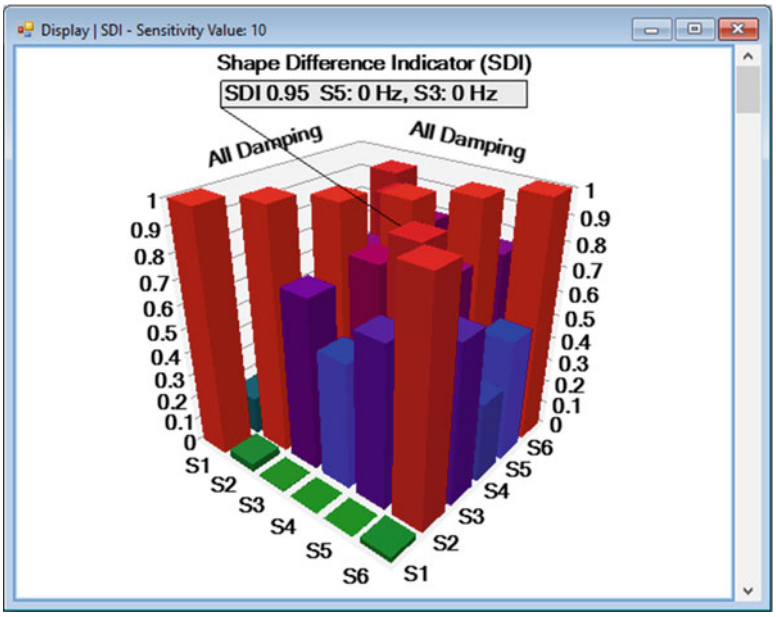

Fig. 8.14 SDI for damping shapes (Sensitivity = 0.01)

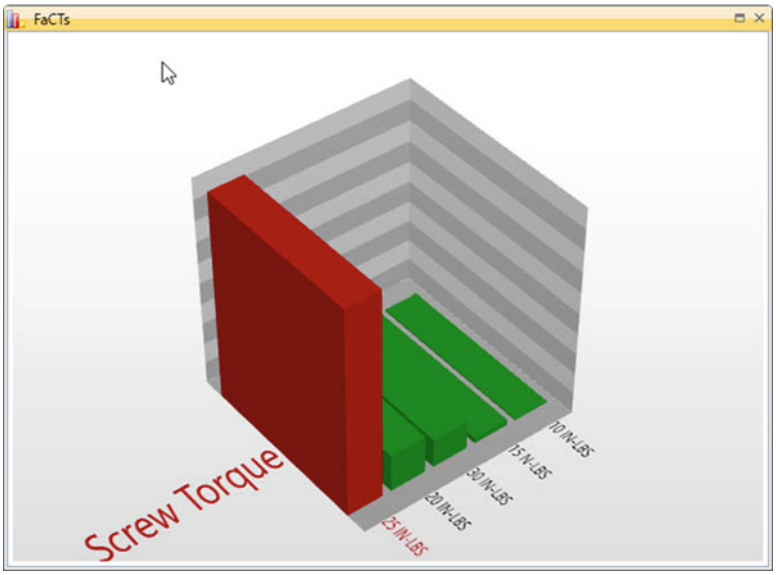

Fig. 8.15 FaCTs™ identifying 25 in-lbs of torque

8.9 Fault Correlation Tools (FaCTs™)

Using SDI as a search criterion for correlating a currently acquired shape with shapes archived in a database has been trade marked as **FaCTs™**, an acronym for **Fault Correlation Tools**. If each of the archived shapes has been associated beforehand with a *known mechanical fault or condition* (cap screw torque in this case), SDI can be used to identify the specific fault. Using the FaCTs™ search method, the FaCTs™ bars with highest SDI values between the current shape and archived shapes are displayed in a bar chart. Each bar is labeled with the fault or condition that correlated highest with the current shape.

In Fig. 8.15, the highest FaCTs™ bar identified the current shape as being associated with the Case 4 of cap screw torque.

FaCTs™ can be used in a number of ways for post-processing data in an online machine health monitoring or structural health monitoring system. As part of an on-line monitoring system, FaCTs™ can be used to graphically indicate any change in a machine operating condition, or to identify a specific structural change such as the torque changes illustrated in this paper.

FaCTs™ can also be used as a pass-fail indicator in a qualification testing system. Vibration parameters, or any other types of engineering parameters acquired from a test article can be numerically compared with archived parameters as a means of passing or failing the test article. FaCTs™ has been implemented in the Vibrant Technology ME'scope software.

8.10 Conclusion

The example used in this paper illustrated a well known fact, namely that *resonant vibration is very sensitive* to changes in the physical properties of a structure. When a physical change in a structure occurs, that change can be detected by measuring changes in the modal parameters of the structure. Furthermore, modal parameters can be used to identify a specific physical change by correlating them with archived parameters stored a shapes.

Stiffness changes were introduced into the Jim Beam by applying different amounts of torque to one of the cap screws used to attach the top plate to the back plate. The amounts of torque applied were different by a *very small amount, only 5 in-lbs*.

The Jim Beam was impact tested after each of the five different torques was applied to the Allen screw. Then the resulting FRFs were curve fit to extract the modal parameters of six modes. These parameters were assembled into two tables of shape vectors, one for the modal frequencies and the other for modal damping.

Two different measures of shape correlation, MAC and SDI, were applied to the modal parameters in the two shape tables. Both measures indicate the likeness of a pair of shapes. Each is a *correlation coefficient* for a pair of shapes, with values between 0 and 1. A value of 1 means that the two shapes are the same, and a value less than 1 means that they are different.

MAC only measures the *co-linearity* of two shapes however, and did not indicate any difference between pairs of modal frequency shapes for the six stiffness cases.

SDI measures the *true difference* between two shapes, but it also did not initially indicate any difference between pairs of modal frequency shapes for the six stiffness cases.

However, a unique property of SDI was used to increase its sensitivity, namely that when the *values of the shapes are closer to the origin,* SDI transitions more rapidly between 1 and 0 when the two shapes are different.

Thus, by using *two modified shapes*, one with *values close to 0*, and the other containing those values plus the *difference between the two original shapes*, the sensitivity of SDI was increased. With increased sensitivity, SDI could be used to clearly identify all six torque cases based on differences between their modal frequency shapes.

SDI was also applied to the modal damping shapes, but even with increased sensitivity, most but not all of the torque cases could be distinguished.

References

1. Ganeriwala, S.N., Schwarz, B., Richardson, M.: Using operating deflection shapes to detect unbalance in rotating equipment. In: IMAC XXVII. Orlando, FL (2009)
2. Richardson, S., Richardson, M., Tyler, J., McHargue, P.: Using operating data to locate and quantify unbalance in rotating machinery. In: IMAC XXXIV, January 25–28, 2016
3. Richardson, S., Tyler, J., McHargue, P., Richardson, M.: A new measure of shape difference. In: IMAC XXXII, February 3–6, 2014
4. llemang, R.J., Brown, D.L.: A correlation coefficient for modal vector analysis. In: Proceedings of the International Modal Analysis Conference (1982)
5. Allemang, R.J.: The modal assurance criterion (MAC): twenty years of use and abuse. In: Proceedings of the International Modal Analysis Conference (2002)

Chapter 9
Current Challenges with BIGDATA Analytics in Structural Health Monitoring

Nur Sila Gulgec, Golnaz S. Shahidi, Thomas J. Matarazzo, and Shamim N. Pakzad

Abstract In SHM, fixed sensor networks with long-term monitoring capabilities, dense sensor arrays, or high sampling rates are perceived to produce BIGDATA. As the temporal and spatial resolution of monitoring data is improved by advances in sensing technology and with the adaptation of new data collection techniques, it is expected that efficient BIGDATA analysis strategies will become highly desirable. In addition to the massive quantity of data collected from these applications, the data's prospective heterogeneity poses a processing challenge. As capable sensing devices become more abundant and economical, it may be beneficial to integrate data collected by traditional means with emerging data types obtained by smartphones or image-based sensing systems. Previous studies have investigated the relationship between sensor network size and the corresponding information extracted by typical SHM methods. The scalability and computational sensitivity of these SHM processes in consideration of large SHM datasets have also been quantified. This paper intends to detail the current challenges posed by analyzing BIGDATA for SHM. This includes both the characteristics of BIGDATA sets produced by SHM and the expected processing challenges associated with these datasets. Novel approaches developed to overcome these challenges are reviewed and the continually evolving nature of BIGDATA is discussed.

Keywords Structural health monitoring • BIGDATA • Signal processing • System identification • Damage detection

9.1 Introduction

There has been a notable increase in public awareness of the U.S.'s aging infrastructure problem. In 2013, the American Society of Civil Engineers (ASCE) declared one in nine of the nation's bridges to be structurally deficient, impacting roughly 210 million daily bridge trips in the nation's 102 largest metropolitan areas [1]. Independently, the U.S. Department of Transportation has come to similar conclusions, estimating "between $123.7 billion and $145 billion per year to maintain and improve the condition of roads and bridges alone" [2]. The ASCE report outlined several solution strategies that directly call for an increase in infrastructure data and implicitly request for Structural Health Monitoring (SHM) methods, e.g. by prioritizing the "the repair of structurally deficient urban bridges" based on risk models.

With over 600,000 US bridges in deteriorating condition, the prioritization of their repairs suggests a need to collect large quantities of data, which contain condition information, over an extended period of time. In this context, the widespread structural deterioration in the US can be addressed by considering BIGDATA. BIGDATA has its first widely accepted definition traced to Laney [3] where it is characterized with the "3 V's: Volume, Velocity, and Variety. The evolution of data storage capacity and processing techniques since this definition (as well as BIGDATA applications in other fields) has led to new BIGDATA descriptions [4]. For example, in addition to the original 3 V's, data complexity [5] and the

N.S. Gulgec (✉)
Department of Civil and Environmental Engineering, Lehigh University, ATLSS Engineering Research Center, 117 ATLSS Drive, Imbt Labs, Bethlehem, PA 18015, USA
e-mail: nsg214@lehigh.edu

G.S. Shahidi
Rutherford and Chekene, 375 Beale Street, San Francisco, CA 94105, USA

T.J. Matarazzo
Senseable City Laboratory, Massachusetts Institute of Technology, 77 Massachusetts Avenue, Cambridge, MA 02139, USA

S.N. Pakzad
Department of Civil and Environmental Engineering, Lehigh University, 117 ATLSS Drive, Imbt Labs, Bethlehem, PA 18015, USA

C. Niezrecki (ed.), *Structural Health Monitoring & Damage Detection, Volume 7*, Conference Proceedings of the Society for Experimental Mechanics Series, DOI 10.1007/978-3-319-54109-9_9

developing relationship among networks and digital devices [6] are mentioned in more recent definitions of BIGDATA. Thus, the BIGDATA problem is defined by more than just the sizes of the anticipated data sets.

Finally, US bridge vibration data is primarily collected for research purposes, which can only provide support to a fraction of the structures in need of repair. In this digital age, over 200 million Americans own a smartphone [7] which is constantly connected to the internet, often embedded with a camera, GPS, and/or accelerometer (among other sensors), and has advanced computing capabilities. It would worthwhile to motivate the SHM community to consider this technological boom as an opportunity to extract infrastructure condition at an unprecedented rate. Ultimately, the challenges of compiling and analyzing mass smartphone data for SHM purposes are consistent with those of BIGDATA.

In this paper, the BIGDATA challenges associated with the general field of SHM are outlined and recent progressions are highlighted. The remainder of this paper is organized as follows: Section 9.2 defines BIGDATA characteristics and considers SHM implementations; Section 9.3 discusses the scalability of processing BIGDATA for typical SHM problems; Section 9.4 reviews developing SHM methods, designed with BIGDATA in mind; finally, Section 9.5 presents the conclusions.

9.2 Bigdata Characteristics

9.2.1 Variety

Data variety—structured, unstructured, and semi-structured—produced by different sources presents a challenge for BIGDATA analytics. Structured data is relatively easy to store and query in a relational database due to its known schema, whereas semi-structured and unstructured data require further data mining in order to organize and analyze [8].

According to a survey conducted by Intel, 84% of 200 IT companies currently analyze unstructured data and list the top five data sources as documents, business transactions, e-mail, imaging data and sensor or service data [9]. SHM has primarily focused on direct instrumentation of a structure with sensors, which provides data that is relevant to the analysis. Typical selections include but are not limited to accelerometers, strain gauges, inclinometers, thermometers and wind pressure sensors, creating semi-structured data. In addition to the resulting data matrix entries, metadata about sensors (e.g. type, sensitivities, locations, orientations) are necessary in monitoring applications [10].

Furthermore, new image-based sensing systems have recently been used for infrastructure monitoring. Image-based and video-based SHM infer information about changes in structural behavior from pictures and digital videos. As an example of a more computer-based vein of image-based SHM, utilization of Digital Image Correlation (DIC) can determine the shifts and/or rotations of elements of a reference image in an image taken under different loading conditions [11]. The unstructured format of such sensing systems obstructs the extraction of SHM information from data.

9.2.2 Volume

The volume of a dataset is an important characteristic for defining BIGDATA. Based on the Intel IT Center survey, large data analytics companies generate a median of 300 terabytes (TB) of data [9]. These volumes can also be produced in SHM from dense sensor networks that collect data during the lifetime of infrastructure. Such data is typically stored over many years to construct a baseline in many SHM procedures.

Present SHM technology measures structural response through wired and wireless contact sensors, as well as the full-field imaging techniques. Wired and wireless dense fixed sensor arrays generally produce a multivariate time series, whose size depends on the number of sensors and samples. To exemplify the storage requirements for such data sets, consider the Tsing Ma, Kap Shui Mun and Ting Kau Bridges in Hong Kong, where approximately 800 sensors (i.e. accelerometers, displacement transducers, strain gauges, level and temperature sensors, weight-in-motion sensors) are monitoring 24 hours per day and are producing 140 megabytes (MB) per hour [12].

In some studies, vibration sensor data are supplemented by other digital devices to help build a more complete structural assessment. For example, the sensor network installed on the Holland Bridge produces 4 GB of data daily from 145 sensors and also incorporates weather station data and a live traffic video feed [13].

Besides contact sensors, full-field imaging generates large datasets. As an example, typical camera frame rates range between 25 and 60 frames per second (fps) and can be increased to up to 240 fps in high-speed cameras [14]. This number increases to 500 fps for full-field data in dynamic applications [15]. Considering the size of each photo to be 2 MB as per Wu et al. [6], monitoring of even a single structure can easily produce terabytes of data per week.

9.2.3 Velocity

One of the main challenges in BIGDATA management is for data transmission, storage, and processing to keep up with the high velocity of data generation. Processing these datasets can be difficult with increasing velocity (i.e., batch to real-time processing). Current IT managers conduct their data analytics by using both batch and real-time processing equally [9].

In this context, SHM data is not an exception. While continually improving sensing technology enables structural data collection with high resolution in time and space, the SHM objective has not been served unless such high-resolution datasets are processed and decisions regarding structural health are inferred in a timely manner. This is a major challenge for rapid decision making after extreme events such as natural and man-made disasters in structures equipped with real-time SHM.

9.2.4 Complexity

Dataset complexity and the evolving relationships among measurements represent another challenge for SHM. Data source uncertainty and dataset variability as a result of long-term health monitoring result in difficulties for managing SHM applications.

Dataset complexity is mostly affected by the inevitable uncertainty in data sources. This uncertainty includes data quality problems such as noise and missing observations [16], as well as data being sourced from uncontrolled environments. The introduction of uncertainty into a dataset leads to a need for additional processing steps not needed for "clean" data that affect the complexity and scalability of SHM algorithms.

Noise is present in SHM datasets for a variety of reasons depending on the type of sensing equipment used. Accelerometers, for example, tend to have increased noise with increased capacitance and reduced size [17]. Images include noise associated with the quality of the cameras used to capture them. All electronic sensors include added noise associated with the resistivity of their components. Alternatively, environmental conditions relating to fog and air quality can affect the information that may be gained from images of a structure.

Missing observations in datasets also affect the uncertainty of structural integrity decisions inferred from these datasets. Most SHM analysis algorithms for system identification and damage detection do not formally accept missing observations (an exception includes the work presented in [18, 19]. This confines the processing of a dataset with missing observations, to either discard the set completely, or estimate the missing observations with a probabilistic framework, generating additional uncertainty in the entire dataset via these estimates. Furthermore, the type of probabilistic analysis required affects the processing time. For example, a multivariate analysis of structural response data at several degrees of freedom may take significantly more processing resources than if multiple responses were condensed into a single, damage-sensitive feature. Missing data may result from instances as sensor malfunctions and lost communication, but is also inherent in some monitoring schemes [20].

Furthermore, inconsistencies can create challenges in collecting numerous sets of data over time. In the case of SHM data, variability in datasets has always been an issue for long-term monitoring systems, where structures and infrastructure systems are periodically monitored and the data is processed for anomaly detection and damage localization. In such scenarios, a long-term established baseline of the monitoring data is required to be used as a reference for decision-making. Such a baseline library is required to reflect the inherent variability in structural behavior in different environmental conditions. Several factors contribute to the variability, such as reliability of wireless sensor networks, durability of data acquisition systems and wires, power consumption problems (especially in the case of wireless sensor networks), and missing data packets.

9.3 Bigdata Processing

The characteristics of a data processing algorithm must also be considered in an evaluation of the overall analysis. In this section, the means for the processing demands of SHM algorithms are estimated. Data loading and cleansing steps that are common precursors to SHM applications require computational resources that are susceptible to the dataset characteristics introduced in the previous section. The algorithms associated with each SHM application also evolve in unique ways.

Given equivalent computational resources, measurement of the CPU time for a function to execute with changing dataset size can be used to assess that function's scalability. Alternatively, if individual functions or algorithms are investigated with varying computational resources, operation counts are required.

The demands of preprocessing functions such as fast Fourier transform (FFT), loading, detrending, and downsampling in MATLAB were explored in [21]. Widespread preprocessing steps such as FFT and loading showed nonlinear increases in CPU time as dataset sizes increased linearly.

These scalability issues become more prominent when considering entire SHM algorithms, which are comprised of several different subfunctions, which often have their own scalability concerns, e.g., LU factorization or singular value decomposition. The high computational efforts needed to produce stabilization diagrams in certain system identification methods have motivated the introduction of new techniques with reduced operations, e.g., ERA-NExT-AVG [22] or STRIDE [19]. Furthermore, [21] demonstrated that numerous, widely-used system identification and damage detection algorithms were not scalable in CPU time with linear dataset dimension increases.

9.4 Promises

Several promising approaches have emerged in order to deal with BIGDATA management and processing. The first novel strategy is using parallel and distributed computing for time and cost efficient data analytics. Hadoop is one of the widely used open-source software developed for distributed storage and processing of massive data [23]. Hadoop achieves distributed data analytics with MapReduce paradigm which is a framework inspired by artificial intelligence expert John McCarthy in 1956 and proposed as "MapReduce" by Dean & Ghemawat [24]. In simple words, the framework takes a single large workload and divides it into smaller sub-workloads for processing of huge datasets in parallel. Although this functional style programming model has been implemented in many real-world applications, it is fairly new to the SHM research community. There are several studies proposing MapReduce model for damage modeling, monitoring, data analytics and uncertainty quantification in concrete structures, [25] structural damage detection and localization of the building structures [26], multi-scale structural bridge health monitoring system [27], and multi-processor system-on-chip (MPSoC) damage detection [28].

It is also possible to reduce the data quantity before processing, or even collecting it. An emerging technology, called Compressive Sensing (CS) [29, 30], was introduced to the research community and has potential to reduce the volume of data transmitted, stored and processed at the time of sampling. This framework has recently been applied to SHM datasets (e.g. [31–35]). Initial findings show that CS is a promising approach that improves the storage requirements, as well as transmission and computation time in SHM applications.

Recently studies have preset newer methods in managing the information involved in structural monitoring applications. Linden et al. presented a cyber-infrastructure system that provides remote access for sensor data acquisition systems, data analysis modules, and human operators [36]. Khazaeli et al. have developed a near-real time data driven structural health monitoring framework to detect damage in structures using the data-driven models along with machine learning algorithms on cloud services [37]. Jeong et al. employed cloud computing services in implementation of a cloud-based cyber infrastructure platform to effectively manage the bridge monitoring data using NoSQL database systems to handle time-series data as well the unstructured bridge information model data [38].

In consideration of this, Matarazzo & Pakzad described a new data class called dynamic sensor networks (DSN), which encompasses mobile sensing data and BIGDATA, for which a truncated physical model (TPM) was presented [19]. Mobile sensing itself is a relatively new SHM scheme that has similarities with BIGDATA. Consider, for example, the work presented by Horner et al. where system identification is performed on a simply supported steel beam [39]. Six mobile sensors scanned approximately 8000 distinct locations on the beam and were stored as a DSN data set. In the usual state-space model representation of the equation of motion of a multi-degree of freedom dynamic system, state variable DOFs coincide with structural sensing nodes—this paradigm cannot be applied to mobile sensing or BIGDATA problems, which consider a very large number of points in space, e.g., 8000. The TPM decouples the size of the dynamic system model from the size of the spatial sensing grid, creating an effective way of processing spatially dense datasets.

By classifying the mobile sensing data as DSN data, the TPM and STRIDE method are applicable and three vertical modes were identified [39]. In particular, mode shapes contained over 20 points which is significant spatial information from six sensors. If an equivalent spatial resolution were desired from a fixed sensor network, over 20 individual sensors would be required, which is more expensive and laborious. The ability to store dense spatial information in an efficient number of observations through mobile sensing is thus clear.

Moreover, the identification framework used for mobile sensor data is directly applicable to BIGDATA, since they both belong to the DSN data class. These tools enable a compressed sensing approach to system identification with BIGDATA [40], which helps reducing computational costs without compromising spatial information.

The strategies presented here by no means represent an exhaustive list of promising BIGDATA management and processing solutions. It is also expected that the continually-evolving nature of BIGDATA problems will reveal even more intelligent solution strategies.

9.5 Conclusion

In the context of typical SHM procedures, BIGDATA may result from special applications, such as long-term monitoring, dense sensor arrays, or high sampling rates. As resolution of monitoring data in time and space is improved through advancement in sensing technology, it is expected that the prevalence of BIGDATA will increase. This paper presents an overview of the anticipated BIGDATA challenges in SHM applications. The challenges associated with the characteristics of applying BIGDATA sets in SHM are investigated in detail. The expected BIGDATA processing demands associated with these datasets are also discussed for typical SHM algorithms. Additionally, novel and promising approaches are briefly introduced.

Despite the challenges that it presents, BIGDATA also represents a wealth of opportunity. Peter Norvig, Google's director of research, summarizes the idea behind their success as: "We don't have better algorithms. We just have more data." [41]. The value behind this idea can be explained as the ability of turning BIGDATA to worth [42] where this worth has some impact on society.

In SHM applications, the ability to collect more data can enable more accurate decision-making about the health of structures. More monitoring locations can yield more accurate mode shapes and more definite damage localizations. In addition to decision-making, the time a dataset is collected may hold particular importance. As an example, in the case of catastrophic events like an earthquake or hurricane, it is difficult to classify a structure as damaged or undamaged in real time. However, with the new opportunities that BIGDATA brings, this may become achievable. To summarize, BIGDATA can represent a challenging task when all obstacles are considered. However, utilizing its power can provide societal benefits, which can contribute to the improvement of America's aging infrastructure.

Acknowledgement The authors would like to thank Matthew Horner for his contributions to this study. Research funding is partially provided by the National Science Foundation through Grant No. CMMI-1351537 by Hazard Mitigation and Structural Engineering program, and by a grant from the Commonwealth of Pennsylvania, Department of Community and Economic Development, through the Pennsylvania Infrastructure Technology Alliance (PITA).

References

1. ASCE: 2013 Report Card for America's Infrastructure. In: American Society of Civil Engineers (2013)
2. U.S. Department of Transportation Federal Highway Administration and Federal Transit Administration. Status of the nation's highways, bridges and transit: conditions and performance (2013)
3. Laney, D.: 3D management: controlling data volume, velocity and variety. In: META Group Research Note, 6, 70. 2014 (2001)
4. Che, D., Safran, M., Peng, Z.: From data to bigdata mining: challenges, issues, and opportunities. In: Database Systems for Advanced Applications, pp. 1–15. Springer Berlin Heidelberg, Germany (2013)
5. Ward, J.S., Barker, A.: Undefined by data: a survey of big data definitions. Preprint arXiv:1309.5821 (2013)
6. Wu, X., Zhu, X., Wu, G.Q., Ding, W.: Data mining with bigdata. IEEE Trans. Knowl. Data Eng. **26**(1), 97–107 (2014)
7. MediaPost: Number of smartphone users in the United States from 2010 to 2019 (in millions)*. *Statista*, < https://www.statista.com/statistics/201182/forecast-of-smartphone-users-in-the-us/> (Oct. 4, 2016), 2015
8. Raghupathi, W., Raghupathi, V.: Bigdata analytics in healthcare: promise and potential. Health Inf. Sci. Syst. **2**, 3 (2014). doi:10.1186/2047–2501–2-3
9. Intel IT Center: Peer Research on Bigdata Analysis. < http://www.intel.com/content/dam/www/public/us/en/documents/reports/ data-insights-peer-research-report.pdf> (Dec. 11, 2015), 2012
10. Jeong, S., Zhang, Y., Hou, R., Lynch, J.P., Sohn, H., Law, K.H.: A cloud based information repository for bridge monitoring applications. In: SPIE Smart Structures and Materials+Nondestructive Evaluation and Health Monitoring, p. 980313. International Society for Optics and Photonics (2016)
11. Yoneyama, S., Kitagawa, A., Iwata, S., Tani, K., Kikuta, H.: Bridge deflection measurement using digital image correlation. Exp. Tech. **31**(1), 34–40 (2007)
12. Ko, J.M., Ni, Y.Q.: Structural health monitoring and intelligent vibration control of cable-supported bridges: research and application. ASCE J. Civil Eng. **7**(6), 701–716 (2003)
13. Vanschoren, J., Vespier, U., Miao, S., Meeng, M., Cachucho, R., Knobbe, A.: Large-scale sensor network analysis: applications in structural health monitoring. In: Hu, W., Kaabouch, N. (eds.) Bigdata Management, Technologies, and Applications, pp. 314–347. Information Science Reference, Hershey, PA (2014)

14. Schumacher, T., Shariati, A.: Monitoring of structures and mechanical systems using virtual visual sensors for video analysis: fundamental concept and proof of feasibility. Sensors. **13**(12), 16551–16564 (2013)
15. McGinnis, M., Barbachyn, S., Kurama, Y.: Application of multiple digital image correlation sensors in earthquake engineering. In: 10th National Conference in Earthquake Engineering (2014)
16. Zuech, R., Khoshgoftaar, T.M., Wald, R.: Intrusion detection and Big Heterogeneous Data: a Survey. J. Bigdata. **2**(1), 1–41 (2015)
17. Lent, B.B.: Practical considerations of accelerometer noise. In: Endevco Website <https://www.endevco.com/news/arc hived-news/2009/2009_12/TP324.pdf> (Dec. 18. 2015) (2007)
18. Matarazzo, T.J., Pakzad, S.N.: Truncated physical model for dynamic sensor networks with applications in high-resolution mobile sensing and BIGDATA. ASCE J. Eng. Mech. **142**, 04016019 (2016). doi:10.1061/(ASCE)EM.1943-7889.0001022
19. Matarazzo, T.J., Pakzad, S.N.: STRIDE for structural identification using expectation maximization: iterative output-only method for modal identification. ASCE J. Eng. Mech. **142**, 04015109 (2016). doi:10.1061/(ASCE)EM.1943-7889.0000951
20. Matarazzo, T.J., Pakzad, S.N.: Structural modal identification for mobile sensing with missing observations. J. Eng. Mech. **142**, 04016021 (2016)
21. Matarazzo, T.J., Shahidi, S.G., Chang, M., Pakzad, S.N.: Are today's SHM procedures suitable for tomorrow's BIGDATA? In: Structural Health Monitoring and Damage Detection, vol. 7, pp. 59–65. Springer International Publishing (2015)
22. Chang, M., Pakzad, S.N.: Observer Kalman filter identification for output-only systems using interactive structural modal identification toolsuite (SMIT). J. Bridge Eng. **19**, 04014002 (2013)
23. Taylor, R.C.: An overview of the Hadoop/MapReduce/HBase framework and its current applications in bioinformatics. BMC Bioinf. **11**(Suppl 12), S1 (2010)
24. Dean, J., Ghemawat, S.: MapReduce: simplified data processing on large clusters. Commun. ACM. **51**(1), 107–113 (2008)
25. Mahadevan, S., Adams, D., Kosson, D.: Challenges in concrete structures health monitoring. In: Proceedings, Annual Conference of the Prognostics and Health Management Society (2014)
26. Yu, L., Lin, J.: Cloud computing-based time seriesanalysis for structural damage detection. J. Eng. Mech. **143**, C4015002 (2015). doi:10.1061/(ASCE)EM.1943-7889/00000982
27. Liang, Y., Wu, D., Liu, G., Li, Y., Gao, C., Ma, Z.J., Wu, W.: Big data-enabled multiscale serviceability analysis for aging bridges. Dig. Commun. Networks. **2**(3), 97–107 (2016)
28. Tran, C.: Structural-damage detection with big data using parallel computing based on MPSoC. Int. J. Mach. Learn. Cybern. **7**, 1213–1223 (2015)
29. Candès, E.J., Romberg, J., Tao, T.: Robust uncertainty principles: exact signal reconstruction from highly incomplete frequency information. IEEE Trans. Inf. Theory. **52**(2), 489–509 (2006)
30. Donoho, D.L.: Compressed sensing. IEEE Trans. Inf. Theory. **52**(4), 1289–1306 (2006)
31. Klis, R., Chatzi, E.N.: Model-based data compression for vibration monitoring using wireless sensor networks. In: Life-Cycle of Structural Systems: Design, Assessment, Maintenance and Management, pp. 138–145 (2014)
32. O'Connor, S.M., Lynch, J.P., Gilbert, A.C.: Compressed sensing embedded in an operational wireless sensor network to achieve energy efficiency in long-term monitoring applications. Smart Mater. Struct. **23**(8), 085014 (2014)
33. Yao, R., Pakzad, S.N., Venkitasubramaniam, P., Hudson, J.M.: Iterative spatial compressive sensing strategy for structural damage Diagnosis as a BIGDATA problem. In: Dynamics of Civil Structures, vol. 2, pp. 185–190. Springer International Publishing, New York (2015)
34. Gulgec, N.S., Shahidi, S.G., Pakzad, S.N.: A Comparative study of compressive sensing approaches for structural damage diagnosis. In: Proceedings of GeoStructures Congress, Phoenix, AZ (2016)
35. Shahidi, S.G., Gulgec, N.S., Pakzad, S.N.: Compressive sensing strategies for multiple damage detection and localization. In: Proceedings of the Society of Experimental Mechanics IMAC XXXIV, Orlando, FL (2016)
36. Linden, G.W., Emami-Naeini, A., Zhang, Y., Lynch, J.P.: Cyber-infrastructure design and implementation for structural health monitoring, nondestructive characterization for composite materials, aerospace engineering, civil infrastructure, and homeland security. Proc. SPIE. **8694**, 869419-2 (2013)
37. Khazaeli, S., Ravandi, A.G., Banerji, S., Bagchi, A.: The application of data mining and cloud computing techniques in data-driven models for structural health monitoring. Proc. SPIE. **9805**, 98052M (2016)
38. Jeong, S., Zhang, Y., O'conner, S., Lynch, J.P., Sohn, H., Law, K.H.: A NoSQL data management infrastructure for bridge monitoring. Smart Struct. Syst. **17**(4), 669–690 (2016). doi:10.12989/sss.2016.17.4.669
39. Horner, M., Koser, K., Korneva, K., Matarazzo, T.J., Pakzad, S.N.: A wireless mobile sensor platform for structural health monitoring. In: Proceedings of the Joint 6th International Conference on Advances in Experimental Structural Engineering and 11th International Workshop on Advanced Smart Materials and Smart Structures Technology, Illinois, IL (2015)
40. Matarazzo, T.J., Pakzad, S.N.: Compressed sensing strategy for BIGDATA in output-only system identification. In: IALCCE Fifth International Symposium on Life-Cycle Civil Engineering (2016)
41. McAfee, A., Brynjolfsson, E., Davenport, T.H., Patil, D.J., Barton, D.: Bigdata: the management revolution. Harvard Bus. Rev. **90**(10), 61–67 (2012)
42. Marr, B.: Why only one of the 5 Vs of bigdata really matters. <http://www.ibmbigdatahub.com/blog/why-only-one-5-vs-big-data-really-matters> (Dec. 13, 2015) (2015)

Chapter 10
Detection of Cracks in Beams Using Treed Gaussian Processes

M. Civera, C. Surace, and K. Worden

Abstract For some years, there has been interest in locating cracks in beams by detecting singularities in mode shape curvatures. Most of the work in the past has depended on the estimation of spatial derivatives (smoothed or otherwise) of the experimentally measured mode shape. This problem is made difficult by the fact that numerical differentiation is notorious for amplifying measurement noise, coupled with that fact that very precise estimates of mode shapes are difficult to obtain. One recent approach, introduced by one of the authors, circumvented the noise issue via a method which did not need numerical differentiation. Briefly, the method applied a Gaussian process regression to the data, using a covariance function that could switch between spatial regions; the switch point—which indicated the crack position—could be determined by a maximum likelihood algorithm. The object of the current paper is to present an alternative approach which uses Treed Gaussian Processes (TGPs). The idea is that separate Gaussian Processes, with standard covariance functions, can be fitted over different spatial regions of the beam, with any switching points learned as part of a decision tree structure. The paper also revisits the idea of using differentiated mode shapes, on the premise that the Gaussian process can 'see through' the noise created and perceive the underlying structure.

Keywords Structural health monitoring (SHM) • Crack detection • Treed Gaussian processes (TGPs)

10.1 Introduction

Since the very inception of the subject of Structural Health Monitoring (SHM) [1], practitioners have looked towards structural dynamics in order to provide damage-sensitive features for data-based diagnostics. Within the context of dynamics, one naturally directs attention towards modal quantities for the required features. The obvious candidates for data-based SHM are the natural frequencies, as it is well-known that they suffer changes as a result of induced damage [2]. The main problem with adopting natural frequencies for SHM is that they are arguably just as sensitive to benign variations in the environmental and operational conditions of the structure as they are to damage [1, Chap. 12], and this can lead to false alarms. As an alternative to frequencies, the mode shapes were proposed, having proved less sensitive to environmental variations. A great deal of the work on mode shapes as features was restricted to beam-like structures and based on the fact that a crack introduces a discontinuity into the mode shape. Unfortunately, the discontinuity was in the second derivative of the mode shape (which represents the local curvature of the beam) and was therefore a subtle effect. The discontinuity could, in principle, be brought to light by twice-differentiating the estimated mode shape; however, this also proved to have issues because of the amplification of noise caused by the process of discrete differentiation. Various attempts at mitigating the effects of differentiation/noise were considered; however, it is not the intention of this paper to survey these attempts. Instead, the focus of this paper is on one specific approach to detecting cracks from measured mode shapes, which attempted to eliminate differentiation from the process of analysis [3]. The approach was based on Gaussian process (GP) regression [4].

In GP regression, a covariance kernel is defined (see later) which characterises the smoothness of the structure being modelled. In the normal usage of GPs, the approach assumes that the structure of interest is *uniformly* smooth and therefore that a single covariance kernel applies everywhere. If one attempts to model a beam-like structure using a Gaussian process, the assumption of uniform smoothness is only valid for an undamaged beam; if a crack is present, it induces short length-scale

M. Civera • C. Surace (✉)
Department of Structural, Building and Geotechnical Engineering, Politecnico di Torino, 10129 Torino, Italy
e-mail: marco.civera@studenti.polito.it; cecilia.surace@polito.it

K. Worden
Dynamics Research Group, Department of Mechanical Engineering, University of Sheffield, Mappin Street, S1 3JD Sheffield, UK
e-mail: k.worden@sheffield.ac.uk

C. Niezrecki (ed.), *Structural Health Monitoring & Damage Detection, Volume 7*, Conference Proceedings
of the Society for Experimental Mechanics Series, DOI 10.1007/978-3-319-54109-9_10

structure (a discontinuity) which is not present in the undamaged portions of the beam. The idea behind [3] was to allow a spatial switch point in the GP covariance which allowed different characteristics in the vicinity of a point and on either side of the point. Once such a covariance function was created, one could determine the position of the crack by maximising the likelihood of the mode shape data by varying the position of the switch point. That this approach could be successful was demonstrated in [3] and supported by comparison with other methods of crack detection from mode shapes in [5]. The approach was also shown to work in the case of multiple cracks (as long as they were reasonably well separated). Arguably, the only real weakness of the approach was that it did not determine the *number* of cracks present, except via a count of the number of local maxima in the likelihood function.

The current paper proposes a method based on GPs which could, in principle, retain the strengths of the previous approach, but also determine the number of cracks in a principled manner. The idea will be to use a *Treed Gaussian Process* (TGP) [6]. In the TGP approach, one does not place switches in the covariance kernel, but divides up the feature space into regions covered by separate GPs with simple covariance functions. In principle, the approach could lead to a measure of the evidence for the number of cracks *and* estimate their locations; however, the analysis is not taken so far in the current paper, which only seeks to establish if the TGP can estimate crack positions via placement of TGP branch points. A feature of the paper will be to reconsider whether it is advantageous to differentiate the mode shape data; the argument being that the TGP can, in principle, distinguish between the different regions of beam curvature even though these are masked by noise.

The layout of the paper is as follows: Sect. 10.2 will present the background to the basic Gaussian process and briefly describe how they were used in the previous crack detection methodology. Section 10.3 will present a short description of Treed Gaussian processes and Sect. 10.4 will describe the data in the current study and present the results of analysis using TGPs. The paper ends with some discussion and conclusions.

10.2 The Previous Approach

10.2.1 Gaussian Processes

Gaussian process (GP) regression has recently become a popular technique in machine learning, although its roots go back many years [4]. In essence, Gaussian processes are a Gaussian distribution over *functions*; unlike most forms of regression model that return a crisp value $f(\underline{x})$ for any given $\underline{x}$, a GP *returns a Gaussian probability distribution*. Among the advantages of the GP for regression purposes are its principled statistical (Bayesian) foundations and the fact that it automatically returns a confidence interval for predictions. GPs adhere to the Bayesian paradigm in the sense that a number of prior assumptions are made about the function being modelled, and then training data (samples of the features) are used to update and evaluate a posterior distribution over functions. Because the implementation of the GP algorithm (unlike its derivation) is fairly straightforward to state, it will be given here in a little detail.

For any set of n input points $\{\underline{x}_1, \ldots, \underline{x}_n\}$, each of dimension d, the prior beliefs about the corresponding outputs can be represented by a multivariate normal distribution, the mean of which is a least-squares regression fit through the training data,

$$E[f(\underline{x})|\underline{\beta}] = m(\underline{x}) = \underline{h}(\underline{x})^T \underline{\beta} \tag{10.1}$$

where $\underline{h}(\underline{x})^T$ is a specified (vector) regression function of $\underline{x}$, and $\underline{\beta}$ is the corresponding vector of coefficients. For simplicity, $\underline{h}(\underline{x})^T$ can be chosen to be $(1, \underline{x}^T)$, representing a linear regression, or simply set to zero. The covariance between output points is given as,

$$\text{cov}[f(\underline{x}), f(\underline{x}')|\sigma_f^2, \sigma_n^2, L] = k(\underline{x}, \underline{x}') \tag{10.2}$$

where σ_f^2 is a scaling factor (sometimes called the *height parameter*), σ_n^2 represents noise variance and L is a diagonal matrix of (inverse) length-scales, representing the roughness of the output with respect to the individual input parameters. These constants are the *hyperparameters* of the problem. One covariance function commonly adopted, is the squared-exponential (SE) function of the form,

$$k(\underline{x}, \underline{x}') = \sigma_f^2 \exp[-(\underline{x} - \underline{x}')^T L (\underline{x} - \underline{x}')] + \sigma_n^2 \delta \tag{10.3}$$

where $\delta = 1$ if $\underline{x} = \underline{x}'$ and is zero otherwise. This expression shows where the hyperparameters occur in the covariance. If the matrix L is restricted to the form δ_{ij}/l^2, only a single length-scale hyperparameter is needed and the covariance is *isotropic*, one obtains,

$$k(\underline{x}, \underline{x}') = \sigma_f^2 \exp\left(-\frac{1}{2l^2}||\underline{x} - \underline{x}'||^2\right) + \sigma_n^2 \delta \tag{10.4}$$

These equations complete the prior specification of the problem; the *posterior distribution* is then found by conditioning the prior distribution on the training data $\underline{y}$ (the vector of output points corresponding to the input training set).

One of the defining properties of the GP is that the density of a finite number of outputs from the process is multivariate normal. Together with the known marginalisation properties of the Gaussian density, it is therefore possible to consider the value of this function only at a number of sampled points of interest: training points and predictions. Allowing $\underline{f}$ to denote the function values at the training points X (where the training vectors have been assembled into a matrix), and $\underline{f^*}$ to denote the predicted function value at a new point $\underline{x}^*$, one has,

$$\begin{pmatrix} \underline{f} \\ f^* \end{pmatrix} \sim \mathcal{N}\left(\underline{0}, \begin{bmatrix} K(X,X) & K(X,\underline{x}^*) \\ K(\underline{x}^*, X) & K(\underline{x}^*, \underline{x}^*) \end{bmatrix}\right) \tag{10.5}$$

where a zero-mean prior has been used for simplicity (see [4] for a discussion), and $K(X,X)$ is a matrix whose i,jth element is equal to $k(\underline{x}_i, \underline{x}_j)$. Similarly, $K(X, \underline{x}^*)$ is a column vector whose ith element is equal to $k(\underline{x}_i, \underline{x}^*)$, and $K(\underline{x}^*, X)$ is the transpose of the same.

In order to relate the observed target data $\underline{y}$ to the function values $\underline{f}$, a simple Gaussian noise model can be assumed,

$$\underline{y} \sim \mathcal{N}(\underline{f}, \sigma_n^2 I) \tag{10.6}$$

where I is the identity matrix. Since one is not interested in the variable $\underline{f}$, it can be marginalised (integrated out) from Eq. (10.5) [4], as the relevant integral,

$$p(\underline{y}) = \int p(\underline{y}|\underline{f}) p(\underline{f}) d\underline{f} \tag{10.7}$$

is over a multivariate Gaussian and is therefore analytically tractable. The result is the joint distribution for the training and testing target values,

$$\begin{pmatrix} \underline{y} \\ y^* \end{pmatrix} \sim \mathcal{N}\left(\underline{0}, \begin{bmatrix} K(X,X) + \sigma_n^2 I & K(X,\underline{x}^*) \\ K(\underline{x}^*, X) & K(\underline{x}^*, \underline{x}^*) + \sigma_n^2 \end{bmatrix}\right) \tag{10.8}$$

In order to make use of the above, it is necessary to re-arrange the joint distribution $p(\underline{y}, y^*)$ into a conditional distribution $p(y^*|\underline{y})$. Using standard results for the conditional properties of a Gaussian reveals [4],

$$y^* \sim \mathcal{N}(m^*(\underline{x}^*), k^*(\underline{x}^*, \underline{x}^*)) \tag{10.9}$$

where,

$$m^*(\underline{x}^*) = k(\underline{x}^*, X)[K(X,X) + \sigma_n^2 I]^{-1} \underline{y} \tag{10.10}$$

is the *posterior mean* of the GP and,

$$k^*(\underline{x}^*, \underline{x}') = k(\underline{x}^*, \underline{x}') - K(\underline{x}^*, X)[K(X,X) + \sigma_n^2 I]^{-1} K(X, \underline{x}') \tag{10.11}$$

is the posterior variance.

Thus the GP model provides a posterior distribution for the unknown quantity y^*. The mean from Eq. (10.9) can then be used as a 'best estimate' for a regression problem, and the variance can also be used to define confidence intervals.

There does remain the question of determining any hyperparameters in an optimal manner; in general this can be accomplished by using an evidence framework [4]. Denoting the complete set of these parameters as $\underline{\theta}$, they can be found by maximising a function,

$$f(\underline{\theta}) = -\frac{1}{2}\underline{y}^T[K(X,X) + \sigma_n^2 I]\underline{y} - \frac{1}{2}\log|K(X,X) + \sigma_n^2 I| \tag{10.12}$$

which is the *log marginal likelihood* and is equal to the log of the evidence, up to some constant. Since the number of hyperparameters is usually small, the optimisation can be carried out simply by gradient descent.

10.2.2 Previous Method: Crack Detection

As described in the last subsection, spatial correlations in the regression model are expressed via the length-scale hyperparameter l in the covariance function (10.4). In the form specified, there is a single length-scale for all the feature space. As discussed in the introduction, this covariance is unsuitable to model a cracked beam, as the crack induces short-length behaviour distinct from the longer length scales required over the remaining (undamaged, smooth) beam. One approach to adapting the GP model to the situation is to specify a covariance function which can switch its behaviour in different regions of the beam, and this was the approach adopted in [3]. Suppose the crack is at a position $x = a$ on the beam, then a covariance function appropriate to the situation can be defined as follows,

$$k(x_i, x_k) = \begin{cases} k_1(x_i, x_j) + k_2(x_i, x_j) & x_i < a, x_j < a \\ k_1(x_i, x_j) + k_2(x_i, x_j) & x_i > a, x_j > a \\ k_1(x_i, x_j) & \text{otherwise} \end{cases} \tag{10.13}$$

(noting that the input variable x is now univariate), and this was the approach followed in [3] where k_1 was taken as a polynomial kernel,

$$k_1(x_i, x_j) = \sigma_f^2(1 + x_i x_j)^N + \sigma_n^2 \delta_{ij} \tag{10.14}$$

and k_2 was an SE kernel as defined in Eq. (10.4). In both cases σ_f^2 and σ_n^2 are hyperparameters associated with the signal and noise variances, and N is a hyperparameter controlling the polynomial order.

All of the ingredients for crack detection using the GP regression are now in place; one simply regards the crack position parameter as an unknown, which is varied in order to maximise the likelihood of the data as specified in Eq. (10.12). It is clear that this approach works by fitting directly to the mode shape data and does not need any estimates of the first or second derivatives of the mode shapes. Results from the previous method will not be presented here, the reader can consult [3] for details. The alternative to this approach which is the subject of this paper, will be introduced in the next section.

10.3 Treed Gaussian Processes

10.3.1 Regression Trees

The idea of a regression tree is fairly simple to state (much of the theory and practice of such trees can be attributed to the work of Breiman and colleagues, and a good reference is [7]). The idea is to partition the independent variable space into regions over which the response behaviour is smooth, and to fit low-order regression models over each region. If the partitioning is carried out by hand, the resulting problem is still amenable to linear least-squares methods. The idea, however, of a regression tree in general, is that the partitions are determined from the data as part of the modelling problem; this renders the estimation problem highly nonlinear and alternatives to least-squares are needed. Breiman and co-workers established a greedy algorithm for fitting the trees that gave good (but suboptimal) solutions. If an effective partition of the data is found, linear regression models over each distinct region can give excellent results; however, in

principle, *any* algorithm can be used once the data have been partitioned into sensible regions. Once the concept of *Classification and Regression Trees* (CART) was established, arguably the next major advance was the development of a Bayesian framework for the algorithm [8, 9]. The new algorithm was based on rigorous concepts of probability theory and proved an effective departure from the greedy algorithm. In Bayesian CART, a prior probability distribution was proposed over all possible tree structures as well as all possible coefficients; this was then refined by using the data to determine which tree was supported by the greatest evidence. The original formulation is too complicated to describe here without taking this paper a long way from its illustrative objectives. In the original Chipman formulation, all the regression models within the tree were linear; this restriction was later removed by Gramacy, who replaced the linear models by more powerful GP models and produced the TGP [6]; Gramacy's work also extended the Bayesian formulation of the problem significantly.

Although Gramacy's TGP algorithm is too complex to explain here, it is possible to summarise an extended variant of the GP algorithm as developed by O' Hagan and colleagues [10] using additional ideas from Bayesian probability. The Bayesian formulation makes the incorporation into a Bayesian regression tree formulation more direct. The main innovation in terms of the GP algorithm is to integrate out (or marginalise over) the hyperparameters σ_f^2 and $\underline{\beta}$, thus removing them from the optimisation problem. The calculation is technically straightforward but very time consuming, a detailed walkthrough can be found in [11]. The integrals involved are usually all Gaussian, and although the expressions are almost always very complicated, the results can be given in closed form. (For simplicity, the closed-form expressions for the case $\sigma_n^2 = 0$ are given below, although all the results presented later were obtained without this restriction.)

The result is a Students t-process, conditional on L and the training data,

$$[f(\underline{x})|y, L] \sim t_{n-q}(m^*(\underline{x}), \hat{\sigma}_f^2 k^*(\underline{x}, \underline{x})) \tag{10.15}$$

where,

$$m^*(\underline{x}) = \underline{h}(\underline{x})^T \hat{\underline{\beta}} + \underline{k}(\underline{x})^T K^{-1}(\underline{y} - H\hat{\underline{\beta}}) \tag{10.16}$$

$$k^*(\underline{x}, \underline{x}') = k(\underline{x}, \underline{x}') - \underline{k}(\underline{x})^T K^{-1} \underline{k}(\underline{x}') +$$

$$(\underline{h}(\underline{x}) - \underline{k}(\underline{x})K^{-1}H)(H^T K^{-1} H)(\underline{h}(\underline{x}') - \underline{k}(\underline{x}')K^{-1}H)^T \tag{10.17}$$

$$\underline{k}(\underline{x})^T = (k(\underline{x}, \underline{x}_1), \ldots, k(\underline{x}, \underline{x}_n)) \tag{10.18}$$

$$H^T = (\underline{h}(\underline{x}_1), \ldots, \underline{h}(\underline{x}_n)) \tag{10.19}$$

$$K = \begin{pmatrix} 1 & k(\underline{x}_1, \underline{x}_2) & \ldots & k(\underline{x}_1, \underline{x}_n) \\ k(\underline{x}_2, \underline{x}_1) & 1 & & \vdots \\ \vdots & & \ddots & \\ k(\underline{x}_n, \underline{x}_1) & \ldots & & 1 \end{pmatrix} \tag{10.20}$$

$$\hat{\underline{\beta}} = (H^T K^{-1} H)^T H^T K^{-1} \underline{y} \tag{10.21}$$

$$\hat{\sigma}_f^2 = \frac{\underline{y}^T (K^{-1} - K^{-1} H (H^T K^{-1} H) H^T K^{-1}) \underline{y}}{n - d - 3} \tag{10.22}$$

$$\underline{y} = (f(\underline{x}_1), \ldots, f(\underline{x}_n))^T \tag{10.23}$$

Determination of this model is basically an exercise in machine learning and therefore its quality is critically dependent on the number and distribution of training data points in the input space, and the values of the hyperparameters. The expressions for $\hat{\underline{\beta}}$ and $\hat{\sigma}_f^2$ shown above are the result of marginalisation; however, it can be shown that they actually coincide with least-squares estimates. The diagonal matrix of roughness parameters L cannot generally be integrated out analytically and it is usually evaluated using maximum likelihood estimation or Markov Chain Monte Carlo (MCMC); this calculation typically represents the most computationally intensive part of the process.

This almost completes the basic description of the models used here—*Treed Gaussian Processes* (TGPs). Although the actual implementation is too complex to explain here in any detail, the basic ingredients have been covered.[1] The TGP partitions the variable space in much the same way as a Bayesian CART and then fits GP regressors over each independent region. The software used for modelling in this work is the TGP package written by Gramacy in the language R [12].

10.4 The Current Data and Results

10.4.1 Current Data

To analyse the performance of the TGP approach, a case study was performed considering a cracked cantilevered beam with the following mechanical and geometrical characteristics: Young's Modulus $2.06\,10^{11}\,\mathrm{N/m^2}$, density $7850\,\mathrm{kg/m^3}$, length 1 m and square cross-section with side 0.02 m. Mode shapes have been calculated numerically using the finite element model. Undamaged sections of the beam were modelled by Euler-type finite elements with two nodes and two degrees-of-freedom (transverse displacement and rotation) at each node. For the section with the crack, the finite element proposed in reference [13] has been employed. It is assumed that the crack is open and does not propagate with time and that the damage affects just the stiffness matrix of the element containing the crack, calculated using principles of linear elastic fracture mechanics, and not the element mass matrix. In the first case, the following damage scenario was examined: a single crack with depth of 0.004 m, located at a distance of 0.30 m from the fixed end of the beam. The analysis was conducted considering initially 100 points spaced regularly along the beam and then 60, with different levels of noise: SNR=100, SNR=80, SNR=60, where $SNR = 20\log_{10}\left(\frac{A_{signal}}{A_{noise}}\right)$. Secondly, the case of two cracks was considered again with a same depth of 0.004 m and located 0.30 and 0.60 m from the clamped end. The number of measurement points was set to 100 for the two-crack case.

10.4.2 Results

To keep the discussion brief, the results presented here will only be for a subset of the modes simulated: the first, sixth and eleventh. As the TGP algorithm implementation used here [12] is a Markov Chain Monte Carlo (MCMC) algorithm, it is required to set the number of samples. For all cases presented here a 'burn-in' period of 2000 samples was allowed (in order for the chains to become stationary) followed by 5000 samples in order to establish statistics. For each run of the algorithm, the *Maximum A Posteriori* (MAP) tree was recorded at the end, and any switching points were noted.

The first exercise considered the 100-point mode shape functions without added noise; this was in order to consider the most idealised situation first. In order to avoid confusing the algorithm with edge effects from the differentiations, 5% of the points were removed from the edges of each data set. A total of 1000 TGPs each were fitted to the mode shape itself and the first and second derivatives. In each case, the number of MAP trees with a single branch point was extracted, and the set of resulting branch points was averaged in order to give an estimate of the crack position. In general, the TGP was able to fit an excellent regression model.

The results of the first exercise are reported in Table 10.1. The results are interesting; where single branch trees are obtained, the branch point provides a good estimate of the crack position. The largest error (for the mode shape) is 28 mm. The best results are for the first derivatives, and this might be explained as follows. The discontinuity in the mode shape

[1] In the full implementation of the TGP code [12], all the hyperparameters are dealt with in a principled manner, including the roughness parameters. In fact the hyperparameters are represented by prior densities, which have their own hyper-hyperparameters. The result of this extra generality is that a much more complex algorithm is needed than the basic Bayesian approach outlined earlier in this section.

Table 10.1 Crack position estimates (mean branch point) for TGP model fits to the mode shape and its first and second derivatives

Function	Mode	Fraction of 1-branch trees	Mean branch point (m)
$\phi(x)$	1	0.044	0.272
	6	0.078	0.273
	11	0.023	0.273
$\phi'(x)$	1	0.685	0.288
	6	0.153	0.289
	11	0.038	0.283
$\phi''(x)$	1	0[a]	–
	6	0.630	0.288
	11	0.038	0.283

[a]for the second derivative of the 1st mode shape, only two-branch trees were produced

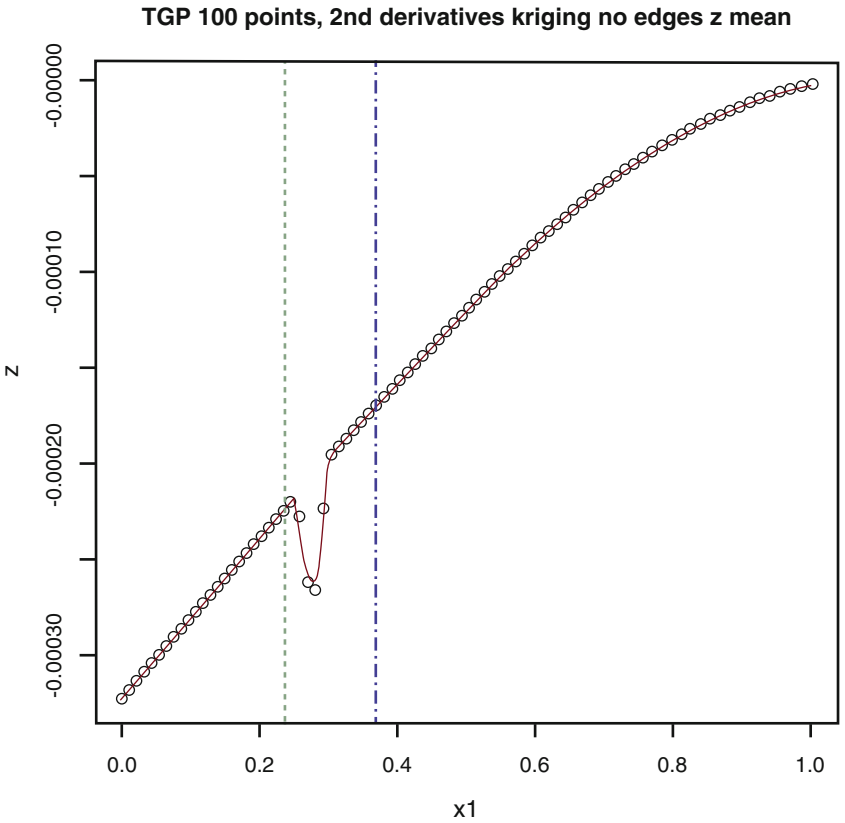

Fig. 10.1 First mode shape curvature $\phi''(x)$ (*circles*) and TGP model fit (*line*). The *vertical lines* indicate the positions of the two branch points in the tree

produced by the crack in the second spatial derivative has a subtle effect. The TGP is able to find a good model in most cases with a single Gaussian process across the whole beam and thus does not branch; this is reflected in the fact that no more than 78 branched TGPs were fitted from the 1000 runs of the algorithm on the mode shapes. In the case of the second derivative of the mode shape $\phi''(x)$, an interesting effect occurs. The way by which the crack was modelled produced a compact region around the crack position distinct from the background curvature, and in general, this would require *three* distinct GPs, and thus a two-branch model. This situation is illustrated in Fig. 10.1; in such a case, the two branches might be expected to bracket the crack position. Another effect on the estimated position is from the proximity of any nodes of the mode shape close to the crack. In the extreme case that the crack is actually at a node, it will clearly not be detectable in the mode concerned.

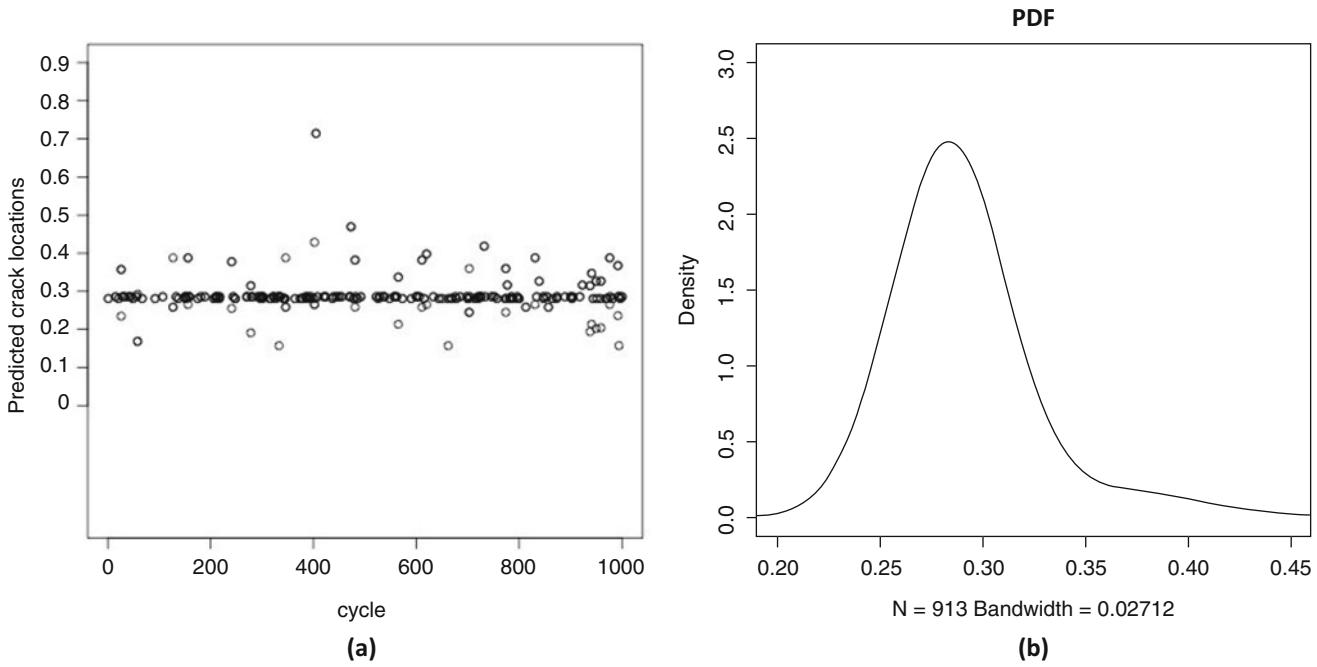

Fig. 10.2 TGP estimates of crack position for mode 6 first derivative- noiseless 100-points data: (**a**) point estimates, (**b**) estimated density function

Table 10.2 Crack position estimates (mean branch point) for TGP model fits to the mode shape $\phi(x)$ with different levels of additive noise

SNR	Mode	Fraction of 1-branch trees	Mean branch point (m)
∞	1	0.018	0.269
	6	0.009	0.267
	11	0	–
100	1	0.008	0.275
	6	0.009	0.269
	11	0	–
80	1	0	–
	6	0.011	0.271
	11	0	–

Figure 10.2 shows some of the results in a more informative format. The crack positions estimated from single-branch TGPs are shown in Part (a) of the figure; these have then been used in order to construct a *kernel density estimate* [14] for the probability density of the crack position in Part (b). The density estimate allows a visualisation of the spread of estimates obtained.

The next exercise considered the slightly more realistic situation of 60-point mode shapes with additive noise. Table 10.2 shows the results obtained for 1000 runs of the TGP algorithm on the mode shapes $\phi(x)$.

The results show that it is quite difficult to discern the position of the crack from the raw mode shape. Although the position estimates are not bad when the TGP branches, the number of branches is very small. This is because the subtle problem of locating the crack in the raw mode shape data is made worse by the presence of the noise. For any SNR values lower than 80, the TGP failed to branch at all. Figure 10.3 shows details of the results obtained for the first mode at the SNR of 100, in terms of the density estimated from the TGP runs. The structure in the density is almost certainly an artefact of the very small number of samples.

The next set of results are for the same exercise, but on the first derivative of the mode shape $\phi'(x)$; they are reported in Table 10.3.

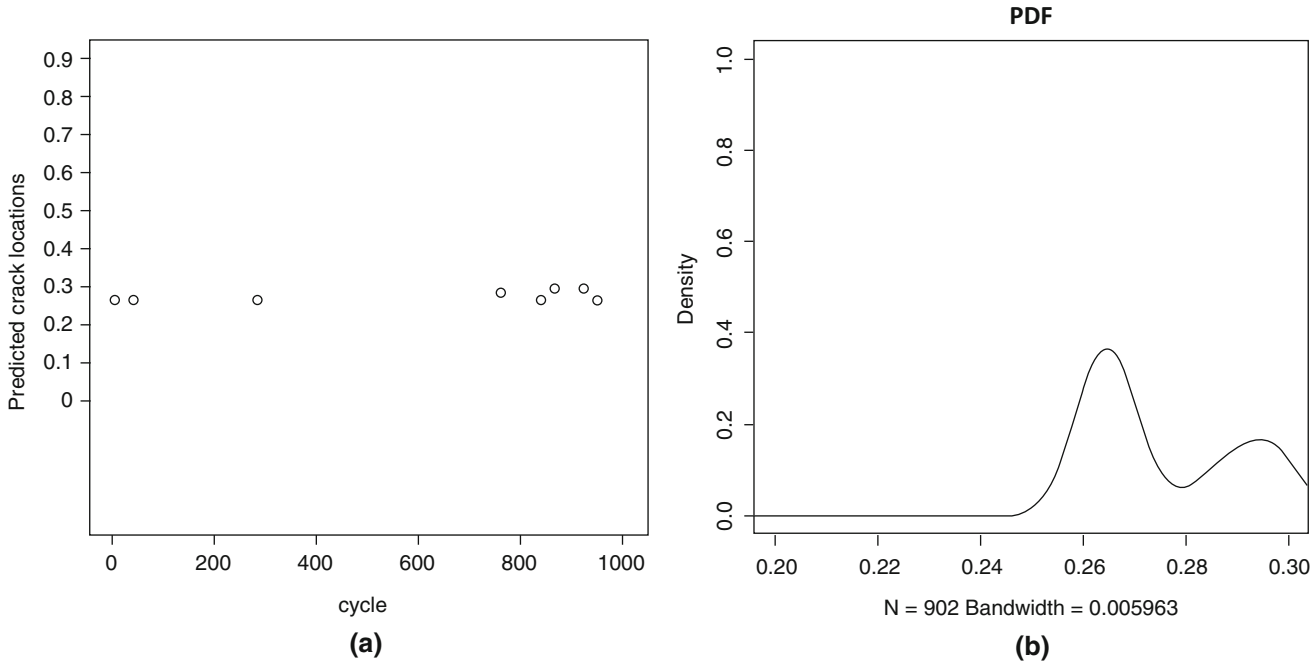

Fig. 10.3 TGP estimates of crack position for mode 1: (**a**) point estimates, (**b**) estimated density function

Table 10.3 Crack position estimates (mean branch point) for TGP model fits to the first derivative of the mode shape $\phi'(x)$ with different levels of additive noise

SNR	Mode	Fraction of 1-branch trees	Mean branch point (m)
∞	1	0.302	0.296
	6	0	–
	11	0.015	0.287
100	1	0.115	0.304
	6	0.029	0.294
	11	0	–
80	1	0	–
	6	0.031	0.290
	11	0	–
60	1	0.303	0.474
	6	0.012	0.316
	11	0	–

As observed earlier, the results for the first derivative $\phi'(x)$, show an improvement on those for the raw mode shape. The estimates of the crack position are more accurate at the same levels of noise; the worst estimate is only in error by 13 mm. Furthermore, the TGP is able to produce some single-branched trees for data with an SNR of 60; although the results for mode 1 are quite badly in error in that case. Specific results for the mode 1, SNR 100 case are shown in Fig. 10.4; in this case 115 of the 1000 TGP runs had a single branch. The figure shows what appears to be a small local minimum in the converged results and this induces a mildly bimodal density function; despite this, the averaged value of the branch point gives the most accurate estimate of the crack location i.e. at 30.4 cm.

The final set of results for a single crack are those for twice-differentiated data $\phi''(x)$, and are presented in Table 10.4. Apart from two cases for mode 1, where rather biased results are obtained, the estimates of the crack position are fairly good regardless of the noise level; in fact, the best estimate is obtained for mode 6 at SNR 60, namely 30.3 cm. Figure 10.5 shows specific results for the most accurate run. This figure makes an interesting point; the mode of the density is biased away from 30 cm, it is the local minimum around 50 cm which is allowing the accurate mean prediction.

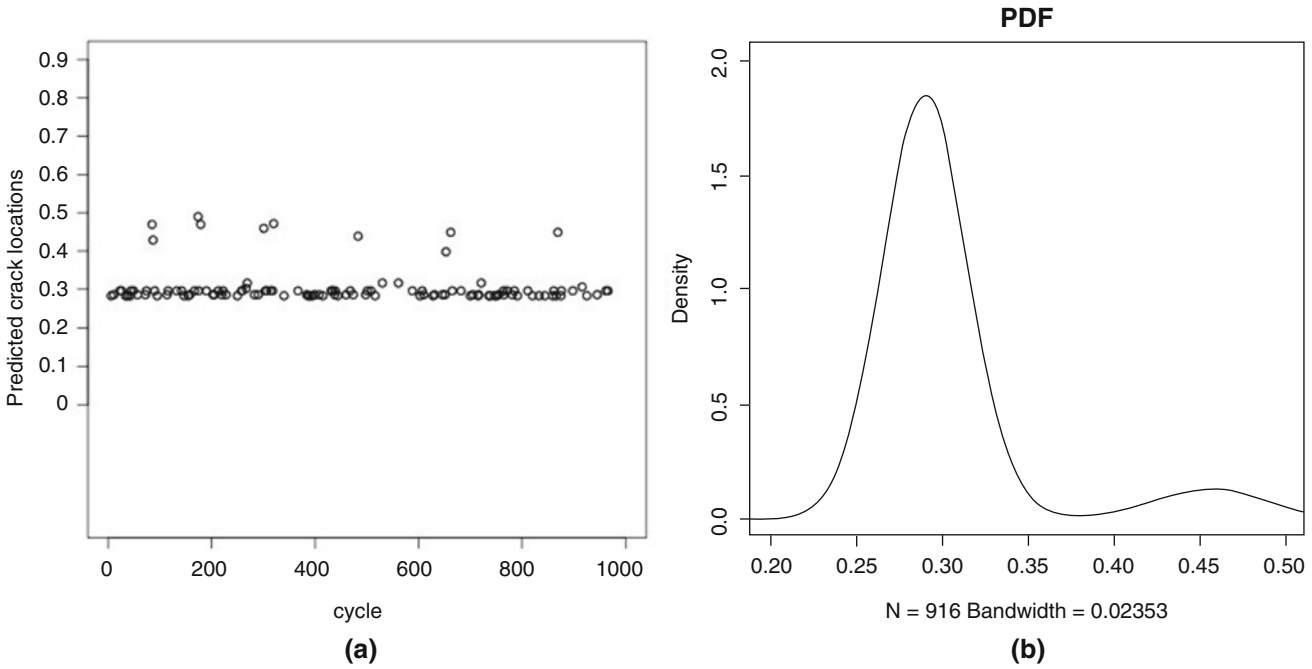

Fig. 10.4 TGP estimates of crack position for mode 1, first derivative, SNR 100: (**a**) point estimates, (**b**) estimated density function

Table 10.4 Crack position estimates (mean branch point) for TGP model fits to the second derivative of the mode shape $\phi''(x)$ with different levels of additive noise

SNR	Mode	Fraction of 1-branch trees	Mean branch point (cm)
∞	1	0	–
	6	0.002	0.316
	11	0.060	0.322
100	1	0	–
	6	0.339	0.314
	11	0.064	0.312
80	1	0.315	0.619
	6	0.402	0.313
	11	0	–
60	1	0.227	0.684
	6	0.191	0.303
	11	0	–

The final set of results is for a group of simulations with two cracks, one at 30 cm and one at 60 cm. Only results for the first mode, obtained from 100-points input data, without any additive noise, will be presented for now. In the case of the raw mode shape, none of the TGP runs arrived at a MAP tree with two branches. For the first derivative of the mode shape, 461 out of 1000 TGP runs arrived at MAP trees with two or more branches; the results are summarised in Fig. 10.6. The results for the second derivative are given in Fig. 10.7; the TGP algorithm arrived at a MAP tree with two branches in 990 out of 1000 cases. In both cases, for the first and second derivatives, the results are biased: the position of the 30 cm crack is underestimated; the position of the 60 cm crack is overestimated. The fact that this is indeed a bias is very clear from Fig. 10.7; there is very little variance in the positions of the branch points.

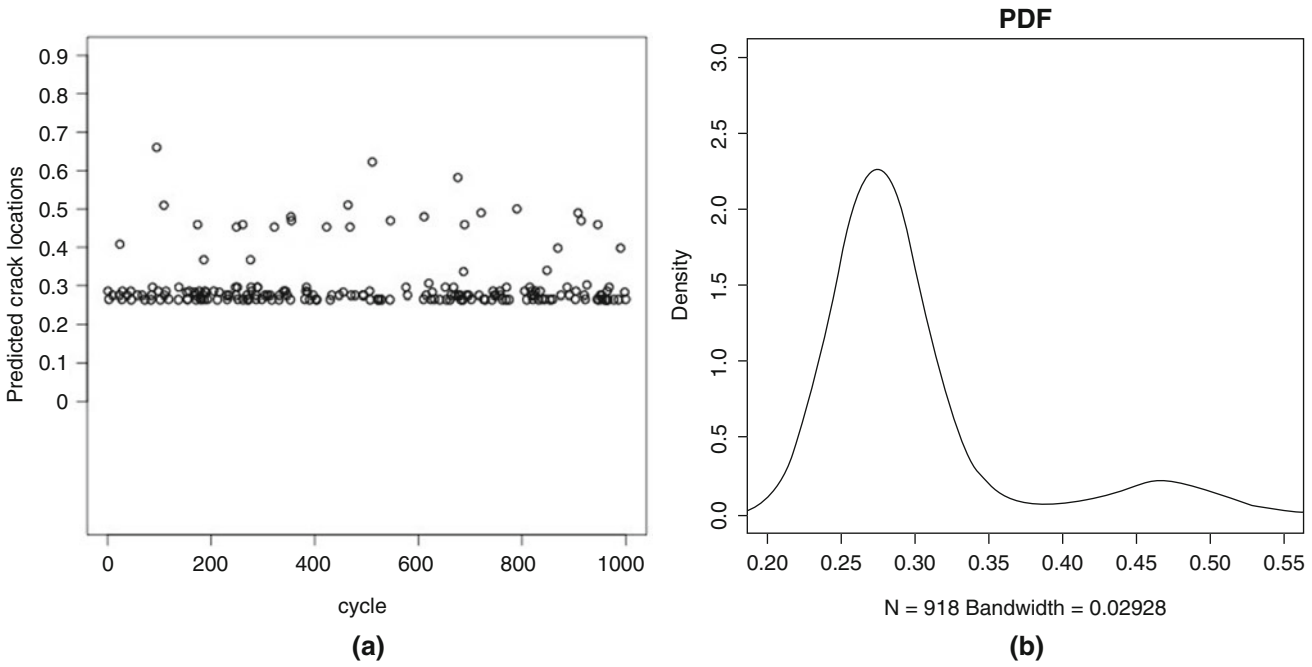

Fig. 10.5 TGP estimates of crack position for mode 6, second derivative, at SNR 60: (**a**) point estimates, (**b**) estimated density function

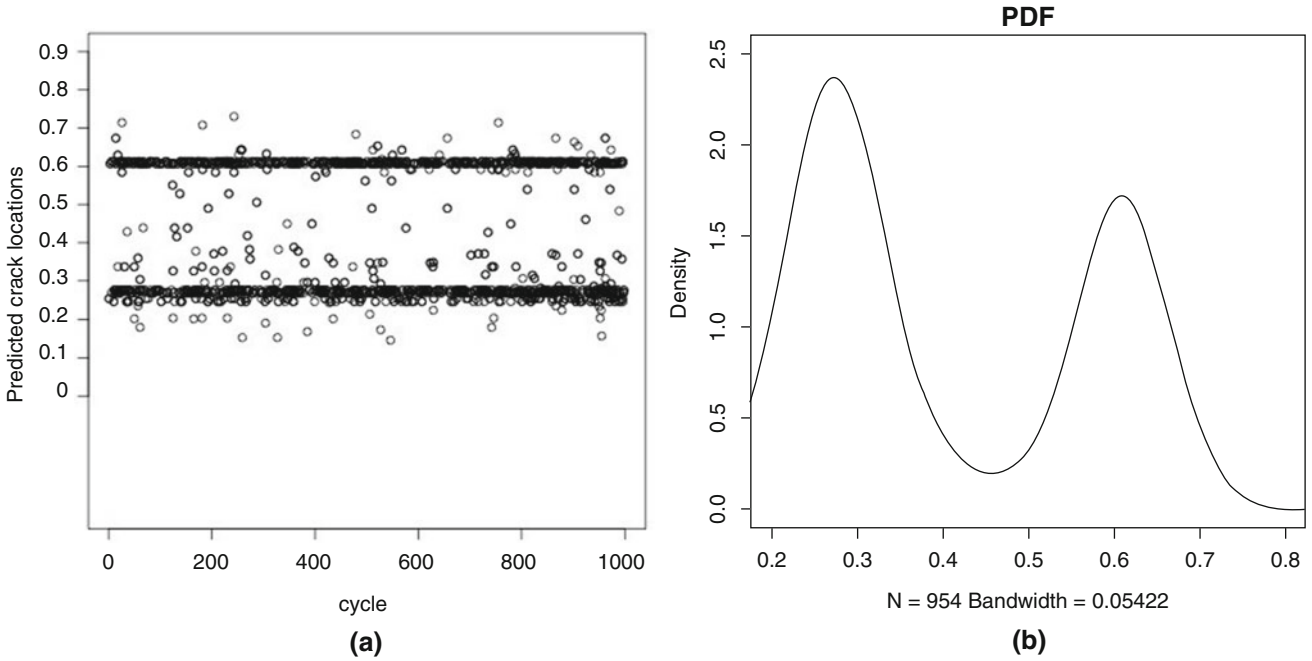

Fig. 10.6 TGP estimates of crack positions for two crack case: mode 1, first derivative, noiseless: (**a**) point estimates, (**b**) estimated density function

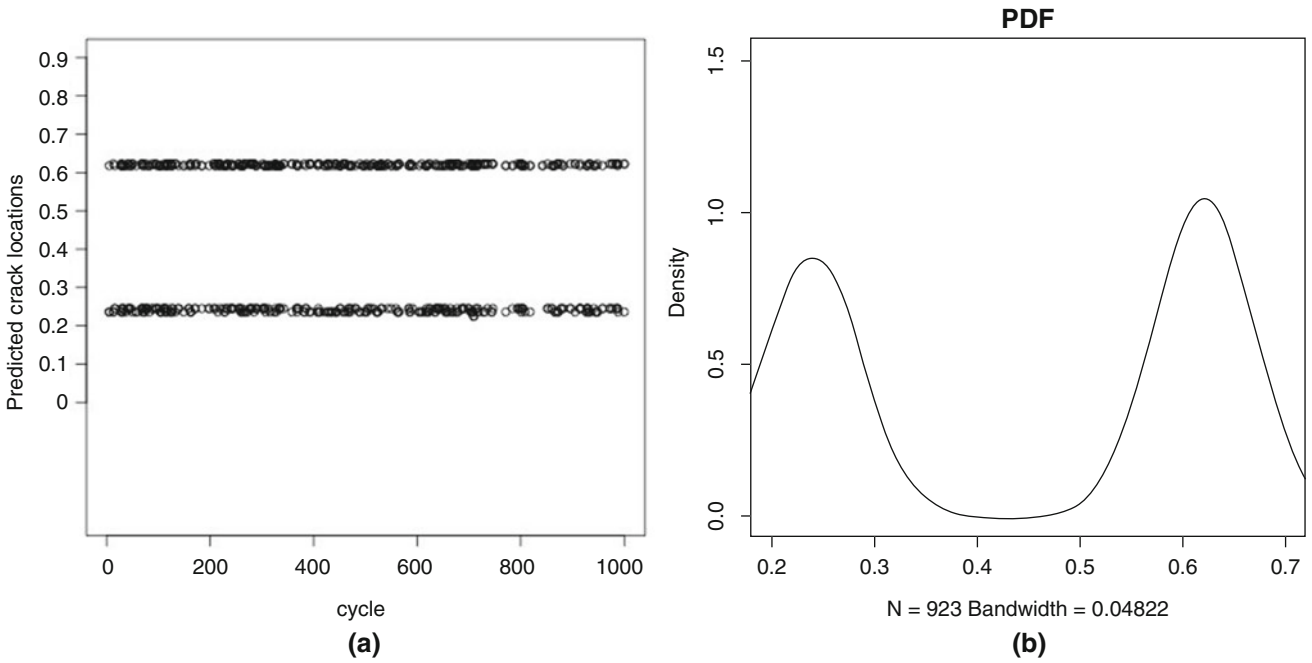

Fig. 10.7 TGP estimates of crack positions for two crack case: mode 1, second derivative, noiseless: (**a**) point estimates, (**b**) estimated density function

10.5 Conclusions

The current paper is very much a preliminary study. The constraints imposed by time limitations forbade a much more systematic study; however, this situation will be corrected in the future. The paper is presented in the spirit that the results obtained do indicate that the underlying ideas have some merit. Using a Treed Gaussian process to indicate the positions of cracks on a beam by the placement of its branch points in a regression model of the mode shape (or its derivatives) appears to work quite well. The main criticism of the current work must be that the approach has only proved feasible in situations where the mode shape estimate is available with low noise at a comparably high number of measurement points. This means that the approach is only applicable if the mode shape estimate is obtained from appropriate technology e.g. laser vibrometry. Allowing for this caveat, the approach appears too work quite well; a sample of sets of results across mode shapes and noise levels is presented here, and the results are quite consistent. It must be said that the results are not yet as good as those from the previously-applied GP approach, where a single GP with split covariance function was applied. This is a little surprising as the likelihood of the data from the TGP model should be the same as that from the single GP with split covariance. The issue is that the TGP is a much more complicated algorithm with more hyperparameters which must be set; it is not yet clear if the results presented here are optimal for the approach. The original motivation for adopting the TGP was that it would not need an a priori specification of the number of cracks; however, this is not strictly a weakness of the original single GP approach, as that could indicate the presence of multiple cracks via local minima in the likelihood function. The main advantage of the TGP approach is that it can potentially find the true minimum of the likelihood in the multiple crack case; whether it achieves its potential will depend on whether future fine-tuning of the algorithm will allow it.

References

1. Farrar, C.R., Worden, K.: Structural Health Monitoring: A Machine Learning Perspective. Wiley, New York (2013)
2. Salawu, O.: Detection of structural damage through changes in frequency: a review. Eng. Struct. **19**, 718–723 (1997)
3. Hensman, J.J., Surace, C., Gherlone, M.: Detecting mode-shape discontinuities without differentiating - examining a Gaussian process approach. In: Proceedings of 9th International Conference in Damage Assessment (DAMAS 2011), Oxford (2011)
4. Rasmussen, C.E., Williams, C.: Gaussian Processes for Machine Learning. The MIT Press, New York (2006)
5. Corrado, N., Surace, C., Montanari, L., Spagnoli, A.: Comparing three derivative discontinuities detection methods for the localisation of cracks in beam-like structures. In: Proceedings of International Workshop on Structural Health Monitoring, Palo Alto, CA (2015)

6. Gramacy, R.B.: Bayesian treed Gaussian process models. PhD thesis, University of California (2005)
7. Breiman, L., Friedman, J., Stone, C.J., Olshen, R.A.: Classification and Regression Trees. Chapman and Hall/CRC, Boca Raton (1984)
8. Chipman, H.A., George, E.I., McCulloch, R.E.: Bayesian CART model search. J. Am. Stat. Assoc. **93**, 935–948 (1998)
9. Chipman, H.A., George, E.I., McCulloch, R.E.: Bayesian treed models. Mach. Learn. **48**, 299–320 (2002)
10. Kennedy, M.C., Anderson, C.W., Conti, S., O'Hagan, A.: Case studies in Gaussian process modelling of computer codes. Reliab. Eng. Syst. Saf. **91**, 1301–1309 (2006)
11. Becker, W.E.: Uncertainty propagation through large nonlinear models. PhD thesis, Department of Mechanical Engineering, University of Sheffield (2011)
12. Gramacy, R.B.: tgp: An R package for Bayesian nonstationary, semiparametric nonlinear regression and design by treed Gaussian process models. J. Stat. Softw. **19** (2007). doi:10.18637/jss.v019.i09
13. Qian, G.L., Gu, S.N., Jiang, J.S.: The dynamic behaviour and crack detection of a beam with a crack. J. Sound Vib. **138**(2), 233–243 (1990)
14. Silverman, B.W.: Density Estimation for Statistics and Data Analysis. Monographs on Statistics and Applied Probability. Chapman and Hall, London (1986)